Evaluating Graphene as a Channel Material in Spintronic Logic Devices

A DISSERTATION
SUBMITTED TO THE FACULTY OF
UNIVERSITY OF MINNESOTA
BY

Yoska Anugrah

IN PARTIAL FULFILLMENT OF THE REQUIREMENTS
FOR THE DEGREE OF DOTOR OF PHILOSOPHY

Prof. Steven J. Koester, Adviser

March 2016

© Yoska Anugrah 2016

Acknowledgements

I would like to thank my adviser, Prof. Steven J. Koester, who has patiently shared his knowledge with me since I joined the Koester Nano Devices Laboratory (KNDL) group back in 2010. It has been an honor to be a part of his group, which he started from scratch at the University of Minnesota. I am eternally grateful for the opportunity that he has given me to learn from him. His guidance has helped me grow as a researcher and I hope to continue to learn by his example.

I would also like to thank my dissertation committee, Prof. Paul A. Crowell, Prof. Jianping Wang, and Prof. Mo Li for their willingness to have discussions that have greatly helped me to try to think critically in the way I approach the problems in my research.

My dissertation project was definitely something that I could never handle all on my own. I would like to express my sincere gratitude to Gordon Stecklein for helping me with all the measurement and analysis of my devices, Dr. Jing Li for his help and guidance, Jiaxi Hu for the helpful discussions and idea exchanges, Qun Su for providing high quality CVD graphene, Jake Odom for helping with exfoliation, and Justin Watts for helping with MBE studies. I would also like to thank all of the Minnesota Nanofabrication Center (MNC) staff members that I have interacted with for their help with the tools in the clean room.

I cannot imagine working for years in a group where the members are no more than just colleagues. For that, I would really like to thank my fellow KNDL group members. You are all my dearest friends and I hope we can continue to be friends no matter where our paths lead us in the future. I thank our former postdocs for their generosity in sharing their knowledge, Dr. Brian Olmsted, Dr. David Deen, and Dr. Eric Olson. I really

appreciate the fun and the knowledge that you have shared with me. I will always cherish the fun times (occasional jokes in the office, afternoon coffee trips to Starbucks on Washington Ave, etc.) that I had with my office mates Nazila Haratipour, Yang Su, Yulong Li, Andrew Stephan, and Qun Su that always renewed my vigor when I needed it the most. I would also like to thank the group members from the "other" office, Matthew Robbins, Rui Ma, Jiaxi Hu, Yao Zhang, Saran Kumar Chaganti, Dr. Seon Namgung and Chaitanya Kshirsagar who take a lot of microwave trips to our office. It is still a mystery to us (from the main office) why some of you have the key to our office but we do not have the key to yours. Is it really just because of the microwave and refrigerator? This is definitely something for all of us to think about. Anyway, you guys are the best and thank you for making my time here enjoyable and memorable.

The support and love that I have received from all of my friends has been overwhelming and for that, I am most grateful. Among them are Alex Hartoto, Ke Li, Liyuan Zhang, Qiaodi Zhuang, Rui Ma, Sirun Chen, Sha Shi, Sze Chiu Cheng, Venty Chai, Weimin Wang, Wilson Hersandy, and Yang Su (in alphabetical order), among others. I am very lucky to have all of you to have fun with and to share the many amazing trips that we took together. I look forward to more of those in the future!

I am also indebted to some of the coffee shops that have provided me comfortable space while I was writing this dissertation, Allegro and Solstice at the U District, Seattle and mainly Starbucks at Dinkytown, Minneapolis.

After almost eight years of living here, Minneapolis has become my home away from home. It has been difficult for me as I begin to prepare to leave this amazing city and the people in it. You will always have a special spot in my heart.

Last but not least, I would like to thank the greatest family anyone could ask for, my family, and especially my parents. Your love is what gives me strength and makes me who I am today. There is nothing that I desire more in this world than to make you happy and proud.

Dedication

This dissertation is dedicated to my family.

Abstract

Spintronics, a class of devices that exploit the spin properties of electrons in addition to the charge properties, promises the possibility for nonvolatile logic and memory devices that operate at low power. Graphene is a material in which the spin orientation of electrons can be conserved over a long distance, which makes it an attractive channel material in spintronics devices. In this dissertation, the properties of graphene that are interesting for spintronics applications are explored. A robust fabrication process is described for graphene spin valves using Al_2O_3 tunnel tunnel barriers and Co ferromagnetic contacts. Spin transport was characterized in both few-layer exfoliated and single-layer graphene, and spin diffusion lengths and spin relaxation times were extracted using the nonlocal spin valve geometry and Hanle measurements. The effect of input-output asymmetry on the spin transport was investigated. The effect of an applied drift electric field on spin transport was investigated and the spin diffusion length was found to be tunable by a factor of ~8X (suppressed to 1.6 μm and enhanced to 13 μm from the intrinsic length of 4.6 μm using electric field of ±1800 V/cm). A mechanism to induce asymmetry without excess power dissipation is also described which utilizes a double buried-gate structure to tune the Fermi levels on the input and output sides of a graphene spin logic device independently. It was found that different spin scattering mechanisms were at play in the two halves of a small graphene strip. This suggests that the spin properties of graphene are strongly affected by its local environment, e.g. impurities, surface topography, defects. Finally, two-dimensional materials beyond graphene have been explored as spin channels. One such material is phosphorene, which has low spin-orbit coupling and high

mobility, and the interface properties of ferromagnets (cobalt and permalloy) with this material were explored. This work could potentially enable spin injection without the need for a physical tunnel barrier to solve the conductivity mismatch problem inherent to graphene.

Table of Contents

List of figures ix

CHAPTER 1 Introduction 1

1.1 Spintronics 1

1.2 All spin logic devices 8

1.3 Graphene 13

1.4 Project overview 20

CHAPTER 2 Spin injection and transport in semiconductors and graphene 24

2.1 Spin injection into semiconductors and the conductivity mismatch problem .. 24

2.2 Nonlocal spin valves for pure spin current detection 35

2.2.1 Spin relaxation mechanisms 35

2.2.2 Nonlocal resistance signal detection 37

2.2.3 Nonlocal Hanle spin precession 43

2.2.4 Nonlocal baseline resistance value due to Peltier and Seebeck effects 45

2.3 Spin injection and transport in graphene 46

2.3.1 Tunnel barriers for efficient spin injection into graphene 46

2.3.2 Spin-orbit coupling in graphene 51

CHAPTER 3 Synthesis and identification of graphene 57

3.1 Graphene exfoliation from highly oriented pyrolitic graphite 57

3.2 Chemical vapor deposition (CVD) growth of graphene 60

3.3 Atomic Force Microscopy (AFM) and Raman spectroscopy for graphene characterization 70

CHAPTER 4 Charge transport properties of graphene 76

4.1 Graphene-based field effect transistors (GFET) 76

4.1.1 Device fabrication 79

4.1.2 Ohmic contacts to graphene 81

4.1.3 Electrostatic gating of GFET 87

4.2 Doping control in graphene by surface chemical treatment 95

CHAPTER 5 Graphene-based nonlocal spin valves 100

5.1 Fabrication of graphene-based nonlocal spin valves 100

5.2 Equipment set-up for nonlocal resistance measurement................................ 106

5.3 Graphene nonlocal spin valve measurement... 107

5.3.1 Nonlocal resistance measurement of graphene nonlocal spin valve....... 107

5.3.2 Nonlocal Hanle measurement of graphene nonlocal spin valve............. 109

5.3.3 Spin transport properties of single-layer graphene 111

5.3.4 Spin transport properties of mechanically exfoliated few-layer graphene ……….. 117

CHAPTER 6 Electric field and doping asymmetry effects on spin transport in graphene ...…………………………………………………………………… 122

6.1 Asymmetric spin transport in graphene nonlocal spin valve due to applied electric field effect 122

6.1.1 Electric field effect on spin transport in semiconductors....................... 122

6.1.2 Tuning of nonlocal resistance in graphene nonlocal spin valve by electric field application 125

6.2 Graphene nonlocal spin valve with incorporated double buried-gate structure for asymmetric doping effect investigation 131

6.2.1 Double buried-gate structure.. 131

6.2.2 Graphene nonlocal spin valve with double buried gate 138

6.2.3 Double buried-gate in graphene-based ASL devices............................. 150

CHAPTER 7 Future directions and conclusion 154

7.1 Potential applications of graphene spintronics 154

7.2 Phosphorene for spintronics beyond graphene 156

7.3 Conclusion 165

List of references ……..……………………………………………..……………… 169

Appendix ……………………..………………………………………………………… 184

List of Figures

1-1	Ferromagnet/Insulator/Ferromagnet (FM1/I/FM2) structures …………..	4
1-2	Simple ferromagnet/nonmagnetic metal/ferromagnet (FM1/N/FM2) structures……….…………………………..................................	6
1-3	Mechanism 1 of the all spin logic (ASL) device concept ……………..…	10
1-4	Mechanism 2 of the all spin logic (ASL) device concept ……………..…	11
1-5	Layout for the logic gates implementation of two-input AND/OR or NAND/NOR gates using mechanism 2 ……………………................	12
1-6	Band structure of graphene ……………………………………………...	15
1-7	Transfer characteristic curves (conductance vs. gate voltage) of graphene FET ………………………………………………………....	18
2-1	Datta-Das electro-optic modulator and spin transistor ………………..…	26
2-2	Ferromagnet/semiconductor structure assuming no Schottky barrier formation ……………………………………………………….………..	28
2-3	Lateral spin valve for spin signal detection ……………...………………	38
2-4	Nonlocal spin valve structure for pure spin current detection ……...……	40
2-5	Nonlocal resistance as a function of in-plane and out-of-plane magnetic fields ……………………….………………………………………………	42
2-6	Illustration of the surface topography of and comparison of surface roughness before and after Al_2O_3 deposition …………………………...	49
2-7	Calculated SOC as a function of the lattice deformation in graphene with (red) and without (blue) the inclusion of the SOC from d orbitals ...	53
3-1	Sequence of steps for the scotch-tape method or mechanical exfoliation of graphene layers from HOPG …………………....……………………	59
3-2	Optical micrograph of a few-layer graphene flake on 300-nm SiO_2 substrate ………………………………….………………………………	60
3-3	Schematic diagram of CVD system for graphene synthesis ………….…	63
3-4	CVD system used for growing graphene in Koester Lab ………	63

3-5	Graphene transfer process from Cu foil to a desired substrate ready for further fabrication ……………………………………………………..	65
3-6	Optical micrograph of CVD grown graphene on 300-nm SiO_2 substrate	66
3-7	Optical image of CVD grown graphene on SiO_2/Si substrate showing PMMA residue ………..……………………………………………	69
3-8	Optical and AFM images of few-layer exfoliated graphene ……….……	70
3-9	Height profiles obtained from AFM analysis ………………...………….	72
3-10	Raman spectrum of single-layer graphene …………...…………………	73
4-1	Electron mobility as a function of band gap for conventional semiconductors and graphene, graphene nanoribbons (GNRs), and carbon nanotubes (CNTs) ………………………………………………..	78
4-2	Graphene FET schematics …………………...…………………………..	81
4-3	Graphene FET resistances and geometry ……………......………………	84
4-4	Output characteristics of GFETs for different channel lengths ………….	86
4-5	Total resistance (R) vs. channel length (L) for GFETs ……….....……..	86
4-6	Channel conductivity measurement for a GFET ……….......………….	88
4-7	GFET parameter extraction by curve fitting ……………...……………..	91
4-8	Carrier concentration as a function of the gate voltage for different interface trap capacitance values ……………….....………………….	92
4-9	GFET curve fitting with and without interface trap capacitance ……..…	94
4-10	The HMDS:acetone vapor treatment environment ……….....………….	97
4-11	Transfer characteristics of GFETs with and without HMDS treatment	98
4-12	Histogram plot of the gate hysteresis for 50 GFETs fabricated on substrates with and without HMDS treatment …………………………..	98
5-1	Exfoliated graphene flake with nonmagnetic contacts ……………….….	102
5-2	Illustration of the Al_2O_3 tunnel barrier deposition process ……..………	103
5-3	Raman spectra of exfoliated few-layer graphene before tunnel barrier deposition ….……………………………………………………….	104

5-4 Raman spectra of exfoliated few-layer graphene after tunnel barrier deposition …… 104
5-5 Optical images of the finished graphene nonlocal spin valve …… 105
5-6 Illustration of the equipment connection for performing graphene nonlocal spin valve measurement …… 107
5-7 Nonlocal resistance and nonlocal Hanle plots of a CVD single-layer graphene spin valve …… 109
5-8 Channel resistivity (solid black line) and nonlocal resistance (blue squares) vs. applied gate voltage (V_G) of the CVD single-layer nonlocal spin valve …… 112
5-9 Predicted relationship between the nonlocal resistance (ΔR_{NL}) and the applied gate voltage (V_G) …… 113
5-10 Nonlocal Hanle data and the fit result of the CVD single-layer nonlocal spin valve …… 114
5-11 Comparison of the diffusion coefficient and spin relaxation time of the CVD single-layer nonlocal spin valve …… 115
5-12 Spin relaxation time vs. diffusion coefficient for CVD single-layer graphene nonlocal spin valve …… 117
5-13 Channel resistivity and nonlocal resistance vs. applied gate voltage of the exfoliated few-layer graphene nonlocal spin valve …… 119
5-14 Relationship between D and τ_S of the exfoliated few-layer graphene nonlocal spin valve …… 120
6-1 Graphene nonlocal spin valve with an independent DC current (I_E) source to produce an electric field along the graphene channel …… 126
6-2 Nonlocal resistance plots of the few-layer graphene nonlocal spin valve for different applied current values (I_E) …… 128
6-3 The applied electric field effect on spin parameters in few-layer exfoliated graphene …… 130
6-4 Double buried-gate structure …… 133

6-5 Transfer characteristic curves of the double buried-gate FET with few-layer graphene channel …………….…………………………………… 135
6-6 Transfer characteristic curves of the double buried-gate FET with CVD single-layer graphene channel ………………………………...……… 136
6-7 Fermi level positions on the left and right gates corresponding to the four points in figure 6-6 …………………………..………………….. 137
6-8 Integrated structure: Graphene nonlocal spin valve with double buried-gate …………………...…………………………………………… 139
6-9 Illustration of the integrated graphene nonlocal spin valve with double buried-gate structure ………………………………..………………… 140
6-10 Color contour plot of the few-layer graphene channel resistivity as a function of the left and right gate voltages ……………………....….. 141
6-11 Color contour plot of the nonlocal resistance of the exfoliated few-layer graphene device as a function of the left and right gate voltages …….… 142
6-12 Color contour plots of the CVD single-layer graphene resistivity as a function of the left and right gate voltages ……………………..…….. 144
6-13 Nonlocal resistance plot for the CVD single-layer graphene as a function of the left and right gate voltages with the spin polarized current injected from FM1 …………………....……………………….. 145
6-14 Nonlocal resistance plot for the CVD single-layer graphene as a function of the left and right gate voltages with the spin polarized current injected from FM2 ……………………….…...……………….. 146
6-15 Measurement results as a function of only the left gate voltage ………... 147
6-16 Measurement results as a function of only the right gate voltage ….…… 148
6-17 Spin parameter comparison between the left and right gate effects …….. 149
6-18 Estimated spin current injected into the detector ……………………..… 151
6-19 Possible design for graphene-based ASL devices with double buried-gate structures ………………..……………………………………….. 153
7-1 Schematic of the few-layer phosphorene back-gated device ……..…….. 159

7-2 Transfer characteristic curves for the few-layer phosphorene devices …. 160

7-3 Evolution of the transfer characteristic curves as a function of temperature …………………………………………………………… 161

7-4 Example Arrhenius plots for the few-layer phosphorene device with Py contact at $V_{BG} = +10V$ …………………………………...………….. 163

7-5 Schottky barrier height as a function of V_{BG} ……………………………. 164

CHAPTER 1 INTRODUCTION

The significance of spintronics is emphasized in this chapter in relation to its promising role for post-CMOS solid state devices owing to its tremendous advance over the course of decades. A proposed concept that aims to utilize spin in all stages of operation is reviewed. Graphene has also been shown to be interesting not only for electronic applications, but also for spintronic devices. The possible applications of graphene and its spin phenomena such as the spin transfer torque and spin Hall effect are brought to the reader's attention. The outline at the end of the chapter should give the reader a clear idea of what topics are discussed.

1.1 Spintronics

Solid state devices have long been dominated by electronics, which operates by controlling the flow of charge carriers, i.e. electrons and holes, to process and store information. The trend in electronics has consistently been to scale down the device size in order to reduce the power consumption, increase the device density, and lower the production cost while simultaneously increasing the processing speed. Reducing the size to few nanometer dimensions, however, comes with several consequences, for example the short-channel effects and limitations in gate dielectric thickness in metal-oxide-semiconductor field effect transistors (MOSFETs). Additionally, at such dimensions, quantum effects can dominate the device behavior. Despite the massive and continued research effort led by both the industry and research institutions as well as improvements in the nanofabrication capabilities, these performance degrading effects due to scaling are

inevitable and will very likely cause the ability to scale down the size of electronic devices to cease.

Fortunately, there is now a different class of solid state devices that are not bounded by such limitations as mentioned above. Spintronics, or spin-electronics as it is often referred to, is a class of devices that manipulate the quantum-mechanical spin angular momentum degree of freedom of electrons, in addition to the charge degree of freedom, to process and store information. In conventional electronics, binary information of bits 1 and 0 is represented by the presence and absence, respectively, of electronic charges. In spintronic devices, however, the same information is coded by the direction of magnetization in the magnets, which are typically made of ferromagnetic metals.

The interest in spintronics research can be traced back to the first experimental demonstration of nuclear polarization in InSb by Clark and Feher.[1] Spin polarization by passing current through a ferromagnet/semiconductor junction was first proposed by Aronov and Pikus.[2] Meservey, Tedrow, and Fulde[3] measured a spin polarization in a thin aluminum film cooled down below its superconducting transition temperature. The experiment back in 1970 was carried out by measuring the tunneling conductance value through a Al/Al_2O_3/Ag stack as a function of the magnetic field, similar to the method described by Bardeen[4] and Giaever[5]. The experimental result showed a split in the tunneling conductance as the magnetic field was varied, indicating the difference in the spin-up and spin-down densities of states in the superconducting aluminum film. Subsequent demonstrations of the same phenomenon in the following years using different ferromagnetic metals confirmed the original result.[6,7] Furthermore, spin injection and

polarization in normal (nonmagnetic) metals was rigorously investigated by Johnson and Silsbee[8–11] based on the theoretical study carried out by Aronov.[12] All of these pioneering results suggested that spin polarization can exist not only in magnetic materials, but also in nonmagnetic materials.

In ferromagnets under equilibrium condition, the densities for spin-up and spin-down electrons are naturally different due to their strong exchange interaction. The consequence of this property was unambiguously observed in the experiments by Julliere[13] in 1975 where the tunneling conductances across a ferromagnet/insulator/ferromagnet (FM1/I/FM2) structure were measured. This kind of structure is called the "spin valve" structure. Figure 1-1 shows an illustration of the structures when the two ferromagnets are parallel (figure 1-1, left) and antiparallel (figure 1-1, right). Julliere found that the resistance of the structure is different when they are parallel and antiparallel, and the difference can be referred to as the tunneling magnetoresistance (TMR), given by

$$TMR = \frac{R_{AP} - R_P}{R_P} \tag{1.1}$$

where R_P (R_{AP}) is the tunneling resistance when the two ferromagnets are in parallel (antiparallel) configuration. The origin of the tunneling magnetoresistance can be explained by the lower illustrations in figure 1-1 as follows. Assuming the spins tunnel without flipping (spin is conserved through the tunneling process), then when the magnetization directions of the two ferromagnets are parallel to each other, there are plenty of states at the Fermi level for the majority spins to tunnel from the FM1 to FM2, hence the lower tunneling resistance. On the other hand, when the two ferromagnets are in the

antiparallel configuration, there are few states at the Fermi level in FM2 for the majority spins in FM1 to tunnel to, resulting in the large tunneling resistance in this configuration. We can then express the tunneling magnetoresistance as a function of the spin-dependent density of states, as given by the Julliere's model:

$$TMR = \frac{2P_1P_2}{1 - P_1P_2} \quad (1.2)$$

where $P_i = (N_{i\uparrow} - N_{i\downarrow})/(N_{i\uparrow} + N_{i\downarrow})$ is the polarization of the ferromagnet (FM_i) and depends on $N_{i\uparrow(\downarrow)}$, which is the density of states (DOS) for the spin-up (spin-down) electrons at the Fermi level.

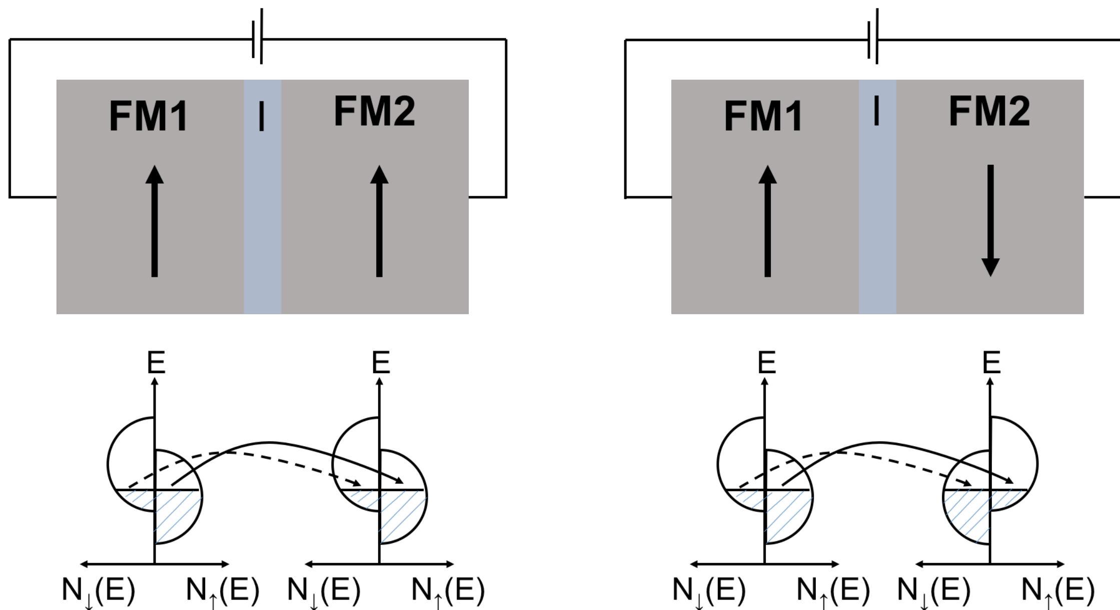

Figure 1-1 *Ferromagnet/Insulator/Ferromagnet (FM1/I/FM2) structures. The structures (upper) and their corresponding spin densities (lower) are shown for the a) parallel and b) antiparallel configurations. The dashed (solid) arrows indicate tunneling of the spin-down (spin-up) electrons.*

The discovery of the TMR effect showed that one could manipulate the resistance of a FM/I/FM stack simply by controlling the relative orientation of the ferromagnets. A

little more than a decade afterwards, another similar effect called the giant magnetoresistance (GMR) was discovered, where instead of the insulator layer, a nonmagnetic metal (N) was inserted in between the two ferromagnetic layers, as shown in figure 1-2. The effect is very much similar to TMR where a significant different in the resistance of the stack is measured depending on the relative magnetization orientations of the two ferromagnetic layers. The origin of the effect, however, is not the same as in the TMR effect. Here, there difference in the resistance is not due to the spin-dependent tunneling probability; rather, it is due to the difference in the scattering rates of the spins. When the two ferromagnets have parallel magnetizations, electrons with spin parallel to that of the bulk ferromagnets can travel unscattered across the stack and the stack resistance is small. On the other hand, when the ferromagnets have antiparallel magnetizations, both spin types experience strong scattering in the ferromagnets, resulting in substantially higher resistance. The conduction through the FM1/N/FM2 in figure 1-2 can be thought of as arising due to two conduction channels, one by spin-up electrons and the other by spin-down electrons, as first pointed out by Mott.[14] The total resistance of the stack is then simply the parallel resistance of the two channels combined. The discovery of GMR by Fert[15] and independently by Grünberg[16] in 1988 started extensive research on this topic and soon afterwards, it found its way into real technological applications, such as magnetic field sensors used in hard disk drives, biosensors, microelectromechanical systems (MEMS), and other devices. In addition, together with TMR effect, GMR is also widely used nonvolatile memory applications, specifically in magnetoresistive random access

memory (MRAM). The Nobel Prize in physics in 2007 was awarded to Fert and Grünberg for the discovery of GMR.

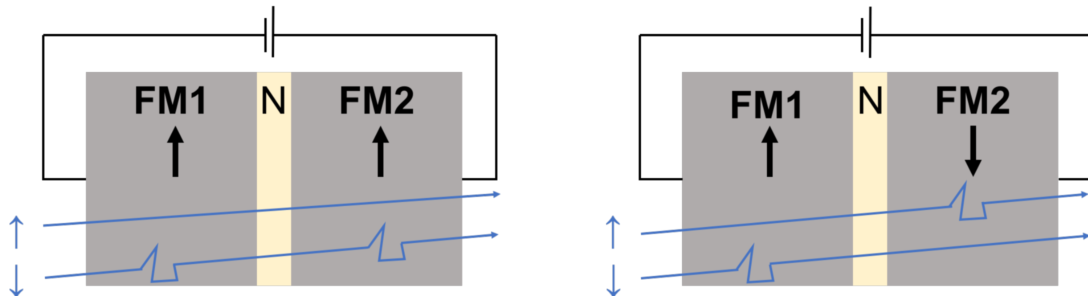

Figure 1-2 *Simple ferromagnet/nonmagnetic metal/ferromagnet (FM1/N/FM2) structures. The structures show how the electrons with spin parallel to the bulk ferromagnet travel unscattered while the electrons with opposite spin experience strong scattering, causing the resistance to be smaller when the ferromagnets have parallel magnetizations (left) compared to when the ferromagnets are in the antiparallel configuration (right).*

Both the TMR and GMR effects require magnetization alignment of the ferromagnets by applying external electric field. In the MRAM structure, this external magnetic field is provided by the current flowing in a write-line and creating current-induced magnetic field to flip the ferromagnet's magnetization. In practice, large amounts of electric current are needed to produce magnetic fields that are sufficiently strong to overcome the anisotropy energy of the ferromagnet and flip its orientation. Another effect that has also gained strong interest from the research community is the spin transfer torque effect (STT). This effect is quite technologically interesting because it enables a spin-polarized electric current passing through a magnetic layer to exert enough torque on the magnet's magnetization to flip its orientation. This effect was originally proposed independently by Slonczewski[17,18] and Berger[19,20] in 1996. The experimental demonstration by Tsoi and collaborators in 1998[21] further propelled the research of this effect, and extensive effort is in motion to develop STT-based MRAM, or what is usually

referred to as STT-RAM. In STT-RAM, it is possible in principle to have the write current of the same order as the read current. Proponents of STT-RAM believe that it has the potential to replace conventional MRAM due to the possibility of switching the magnetization direction using smaller current density and having higher device density (better scalability) compared to the conventional MRAM. However, the prediction of lower-current switching has not been realized.[22–24] The disparity between prediction and experiments is a topic of active research.

It is also important to point out that there is a known effect that enables the detection of spin current without the need for a ferromagnet, namely the spin-Hall effect, first predicted by Dyakonov and Perel in 1971[25] and later rediscovered by Hirsch in 1999.[26] It was predicted that due to the spin-orbit coupling between an electron's spin and momentum, an asymmetry in the scattering of the spin-up and spin-down electrons should arise which results in spin imbalance perpendicular to the direction of the current flow in a nonmagnetic material with considerable spin-orbit coupling. The spin imbalance can in turn be detected using the inverse effect where the difference spin orientations diffuse through a separate nonmagnetic material and in the process of doing so create an asymmetry in the motion of the electrons that results in charge imbalance that can then be detected. This inverse effect is widely known as the reverse spin-Hall effect and the voltage generated is called the spin-Hall voltage (V_{SH}). Experimental demonstrations of these effects[27–32] have been achieved. These effects serve as a relatively new means to study spin related effects, however it could still be a long way before they can translate into real applications.

Spintronics is clearly an interesting field of study where not only the spin phenomena of the electrons are explored in terms of the fundamental physics research, but also put into real technological applications. Spin-based devices have a lot to offer; however, being relatively new and not very well understood, there remains to be significant challenges to optimizing the performance of the current spin-based devices. The author would like to refer the interested reader to these articles[33,34] for more comprehensive review on spintronics and its applications.

1.2 All spin logic devices

Continued scaling of complementary metal-oxide-semiconductor (CMOS)-based transistors over the past few decades has reached the point where further scaling causes uncontrollable increase in the power dissipation. With the physical limits of CMOS technology approaching, it has become clear that the need to develop the new logic technology is inevitable. Spintronics-based devices are among the several technologies currently under heavy investigation and they could enable low power operation, increased speed and density.

Several logic applications have been proposed where spin is implemented as a state variable.[35,36] These approaches promise low-power operation and scalability of the devices. However, sophisticated circuitry may be needed for the operation and Amperian magnetic fields are required to switch the magnetization of the magnets. Behin-Aein *et al.*[37] proposed for the first time in 2010 a logic scheme that can be performed entirely in the spin domain using a concept called all spin logic (ASL) devices. Using this type of devices, not only can information be stored in the nanomagnets' magnetizations but it can also be transferred

by means of pure spin current. The spin current that carries the information is used to flip the magnetization of the nanomagnets using the spin transfer torque (STT) effect discussed in the previous section and it has since been observed experimentally.[38,39] Since the devices operate only in the spin domain, neither spin-to-charge conversion is needed, nor the nanomagnets need an external magnetic field to switch the magnetization, which could simplify the circuit design and lower the device footprint.

In the proposal, two mechanisms were proposed. The first one is shown in figure 1-3. In this configuration, the information is stored as the magnetization direction in the magnetic free layers (1), which due to the shape anisotropy in the design, are bistable. This means that it is energetically favorable for the magnets to align their magnetization in one direction (or the direction 180 degrees from it), which is along the easy axis of the magnetization. V_{supply} provides the charge current that goes to the ground contact (5) and generates spin current in the spin-coherent channel (4). The tunneling layer (3) serves to improve the spin polarization in the channel; this will be explained in detail in the next chapter. The isolation layer (2) is designed to isolate the input signal from the output signal of the magnet. Sufficient spin current must be injected by the input magnet to generate enough torque to switch the magnetization of the output magnet either parallel or antiparallel to the input magnet depending on the voltage polarity applied to V_{supply}. If a positive voltage is applied to V_{supply}, the resulting current will flow from V_{supply} into the ground and this means that the electron spins parallel to the input magnet are preferably drawn into the input magnet, causing an excess of the opposite spin species in the channel. The spin current will then exert a torque that flips the magnetization of the output magnet

antiparallel to the input magnet. If a negative voltage is applied, however, there will be an accumulation of spins parallel to that of the input magnet in the channel. When sufficient torque is present, the output magnet will flip its magnetization to the direction parallel to the input magnet.

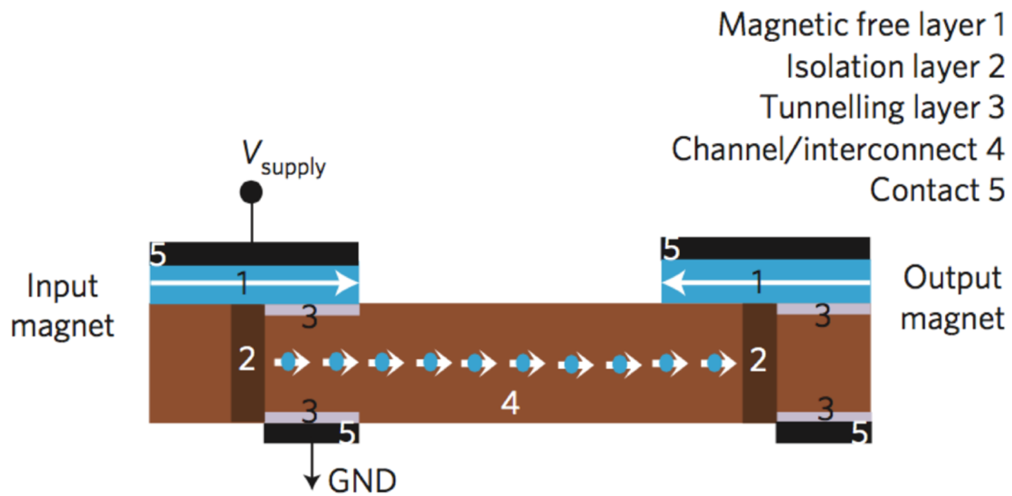

Figure 1-3 Mechanism 1 of the all spin logic (ASL) device concept. Reprinted by permission from Macmillan Publishers Ltd: NATURE NANOTECHNOLOGY (Behin-Aein, et al. [37]), copyright 2010.

The second mechanism that was proposed is shown in figure 1-4. In this structure, the input and output magnets now have a magnetic fixed layer separated by a spacer layer from the magnetic free layer. This structure has the advantage of requiring lower spin current in the channel, since most of the work will be done by applying a voltage to the output magnet itself, but may require a more complicated clocking scheme. This could be achieved as follows. In the first mechanism, the input takes full charge of the output. In the second mechanism, V_{supply} is applied directly to the output magnet and in the process, spins accumulate in the spacer and put the magnetization of the output magnet in the high energy state (its hard axis). Once the output magnet has its magnetization in the high energy

(neutral) state, it is ready to receive information and the input magnet needs only provide enough spin torque to flip the magnetization of the output magnet to one of the bistable states once the V_{supply} is removed. The input signal is supplied by V_{bias} and needs to be larger than thermal fluctuations that could tilt the magnetization of the output magnet randomly.

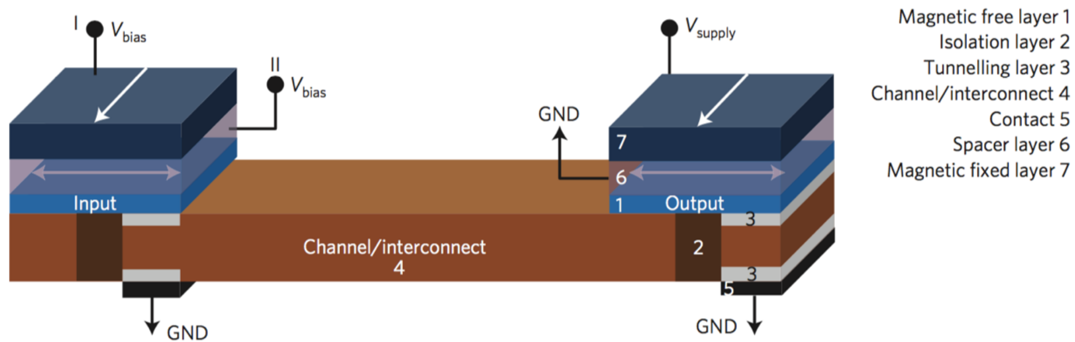

Figure 1-4 Mechanism 2 of the all spin logic (ASL) device concept. Reprinted by permission from Macmillan Publishers Ltd: NATURE NANOTECHNOLOGY (Behin-Aein, et al. [37]), copyright 2010.

Logic gates can be realized using this proposed concept, as shown in figure 1-5. Gate A shows a two-input ("send") gates with one fixed (middle "send") gate. When V_{supply} is applied to the "receive" gate in Gate A to put its magnetization in the higher energy state, V_{bias} is applied to the "send" gates and following the majority rule, the magnetization of the output ("receive") gate will flip according to the dominant spins. In the picture shown, if V_{bias} is negative, Gate A will behave as a two-input OR gate; if V_{bias} is positive, it is a two-input NOR gate. Two-input AND and NAND gates can be obtained simply by rotating the magnetization of the fixed (middle "send") gate 180 degrees. The discussion for the "idle" gates is intentionally left out because they may or may not be necessary for performing the logic function.

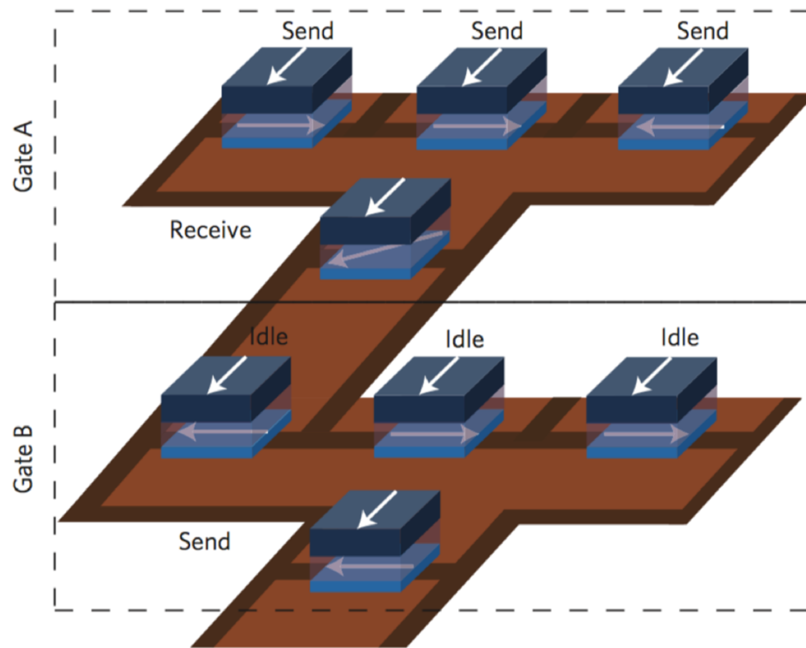

Figure 1-5 Layout for the logic gates implementation of two-input AND/OR or NAND/NOR gates using mechanism 2. Reprinted by permission from Macmillan Publishers Ltd: NATURE NANOTECHNOLOGY (Behin-Aein, et al. [37]), copyright 2010.

We have seen that all spin logic (ASL) devices can potentially be used to perform complete Boolean operation simply by cascading the AND/OR and NAND/NOR gates shown above. Because the magnets used are bistable, the devices are naturally "nonlinear", meaning the output signal should align itself to one of the stable states to represent a "0" or "1" during the logic operation. The devices are definitely "concatenable" due to the similar magnets used at the input and output terminals, and therefore the output of one stage can be used as input to the next stage while keeping all biasing parameters constant. In the proposed device, feedback is eliminated by using a tunnel barrier in the input side to improve the spin polarization and a transparent (low-resistance) contact at the output to suppress the feedback. It should also be noted that in both mechanisms 1 and 2, the ground contact is located closer to the input than the output. This is done in order to more

efficiently generate spin current in the input than in the output, which could also suppress the feedback.[40] In the second mechanism, the switching energy comes from V_{supply} directly applied to the output magnet and the input only needs to provide a small bias signal to put the output magnetization in the correct state. This ensures the signal level is maintained throughout the logic operation. The ideal all spin logic (ASL) devices possess all of the characteristics mentioned above and can indeed perform the same functionality of CMOS-based logic devices. Furthermore, ASL devices have built-in memory stored in the nanomagnets, and since the information is stored in the form of magnetization, it is nonvolatile, meaning that it remains even when the devices are powered off.

The main potential advantage of an ASL-device over its CMOS counterpart, i.e. its low-power operation, has not been demonstrated experimentally. The switching energy for the nanomagnet is typically orders of magnitude higher than the theoretically predicted value.[22,24] For example, it was pointed out that a magnet with activation barrier of $40kT$ could theoretically be switched using energy of less than 10^{-18} Joule, while it has been shown to require tens of femto Joules experimentally.[23,41] A huge discrepancy between the theoretical limit and the experimental value is also true in the case of the switching speed.[22,42] Obviously, these discrepancies will have to be addressed for ASL to be competitive with CMOS.

1.3 Graphene

It was long believed that free-standing two-dimensional crystal could not exist in nature because it was thermodynamically unstable. However, that belief was shattered after the successful isolation of single-layer of a particular material called graphene in 2004[43],

which was later awarded the Nobel Prize in Physics in 2010. In this experiment, graphene layers were mechanically exfoliated from bulk graphite using adhesive tape. Graphene is a one-atom thick sheet of carbon atoms arranged in the honeycomb structure. Each carbon atom in graphene forms an sp^2 bond with its three neighbors. The distance between two nearest carbon atoms was found to be 1.42 Å. Due to the sp^2 hybridization and small carbon-carbon distance, the interatomic bond (also known as the σ-bond) is strong enough to provide stability to the two-dimensional sheet against any thermal fluctuations that may otherwise cause the sheet to collapse. There are four valence electrons in a carbon atom, three of which are responsible for the σ-bond in the two-dimensional plane. The last one forms an out-of-plane π-bond responsible for the electronic conduction in graphene. The π-bonds from different carbon atoms overlap and hybridize to form π-band and π*-bands located above and below the two-dimensional plane.

Single-layer graphene is a semi-metal with no band gap. The conduction and valence bands intersect[44] at the zero energy point called the Dirac point. At low energy, the dispersion relation in graphene is shown in figure 1-6 can be expressed as a linear function of the momentum:

$$E(k) = \hbar v_F k \tag{1.3}$$

where $\hbar$ is the reduced Planck's constant, $v_F \sim 10^8\ cm/s$ the Fermi velocity in graphene, and k the momentum relative to the K or K' points, which are two non-equivalent sets of three points that comprise the six points at the corners of the first Brillouin zone. This linear E- k relationship is similar to that of massless Dirac particles. Therefore, the electronic properties in graphene are better described by the Dirac equation, rather than the

Schrödinger equation. The relativistic behavior arises due to the interaction between the electrons moving around carbon atoms and the periodic potential of the lattice.[45] Graphene also demonstrates a minimum conductivity as predicted in theory for massless Dirac fermions. The minimum value of the conductivity observed experimentally around $4e^2/h$ is higher than the predicted value of $4e^2/\pi h$.[45,46] It is unclear what causes the discrepancy, which has come to be known as 'the mystery of a missing pie'. In addition, quantum Hall effect[47–51], quantum interference and Klein tunneling effect[52] as well as quantum spin Hall effect[53] have also been observed in graphene. One phenomenon after another is being discovered in graphene which makes it very valuable for fundamental physics research.

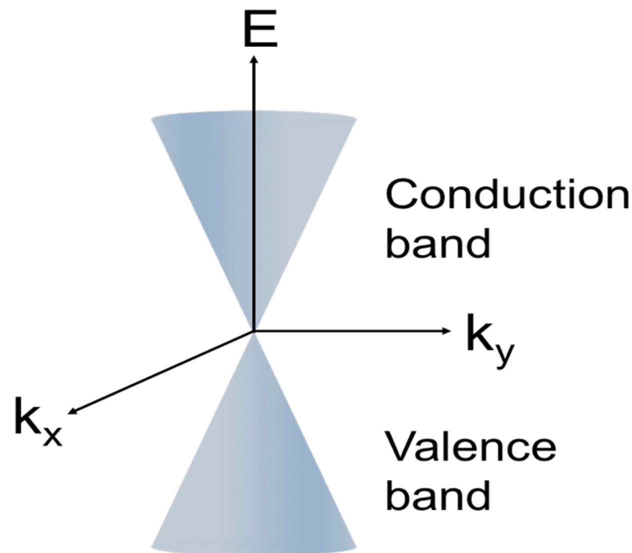

Figure 1-6 Band structure of graphene. The linear relationship between the energy and momentum is shown. There is no band gap in large-area single layer graphene and at zero energy the conduction meets the valence band at the Dirac point.

As silicon-based devices approach the physical limit, the search for alternative materials to continue to scale down future electronics has intensified. Graphene is technologically interesting mainly due to its extremely high carrier mobility. Its intrinsic

carrier mobility can theoretically reach 200,000 $cm^2V^{-1}s^{-1}$, higher than that of InSb (77,000 $cm^2V^{-1}s^{-1}$), which is currently the highest mobility inorganic semiconductor, and carbon nanotubes (100,000 $cm^2V^{-1}s^{-1}$).[54] Graphene on SiO_2 substrate is predicted to have its carrier mobility decreased to about 40,000 $cm^2V^{-1}s^{-1}$ at room temperature due to the surface phonons at the SiO_2 surface. The substrate effect is also believed to be the limiting factor of the carrier velocity at high electric field causing the velocity to saturate at a value of 3-5 times larger than in a typical n-type silicon.[55,56] Being a two-dimensional material with a low density of states makes it possible to control the carrier density in graphene by electric field. This is not possible for bulk semiconductors and metals due to the much higher bulk concentration compared to the surface and extremely small charge screening length, which is typically less than 1 nm. Achieving atomically thin semiconductor and metal layers has also proved to be a formidable task due to the thermodynamic stability limitation of such thin films.

Owing to the advantages mentioned above, graphene surely emerges as one of the potential candidates for future high-speed transistors.[43,57–67] However, there are a few challenges that have prevented graphene from taking over silicon. The absence of a band gap and presence of residual charge in graphene, for example, cause the field-effect transistors (FET) based on graphene to have mediocre current on/off ratio (I_{on}/I_{off}) and therefore a huge leakage current. It is possible to induce a band gap in graphene by patterning it into nanoribbons. In such a small dimension, the quantum confinement in the graphene causes the energy gap to appear. Various methods to pattern graphene have been studied and proposed by different groups.[68–72] Another challenge is integration of graphene

in large-scale circuits. This requires consistent production on a large-scale of high-quality graphene free from defects and contamination. So far, this has been very challenging, and conclusive fundamental research in graphene has generally been done on graphene exfoliated from bulk graphite, a process that produces small graphene flakes in a random manner. Large-area graphene growth on metal and insulating substrates is still an active area of research[57,58,73–78] and heavy emphasis has been placed on growing large-area single crystal graphene with high carrier mobility.

Being a two-dimensional material also means that graphene's properties are heavily affected by what is happening on its surface. In particular, water molecules underneath and above the graphene surface in a graphene transistor have been known to introduce unintentional hole doping and shift the Dirac point to a more positive gate voltage[79–82], as shown by the transfer characteristic (conductance vs. back-gate voltage, V_{bg}) curve in figure 1-7(a). Furthermore, water molecules together with some adsorbates (oxygen, organic residues from processing, etc.) have been shown to act as charge trapping sites and can cause hysteretic behaviors in graphene transistors as demonstrated by figure 1-7(b). The doping and charge trapping effects are dependent on growth, ambient, and processing conditions which can be significantly different for two devices fabricated in different labs or at different times. To be able to fabricate reproducible and robust graphene devices, reliable ways to controllably change the doping[83–86] and suppress the hysteresis[82,87–89] are investigated. Any impurities on the graphene surface can also degrade the interface between graphene and the metal contacts, resulting in increased series resistances in graphene transistors. The dependence of graphene device performance on the graphene-

metal interface quality has been explored, both in the DC[90–97] and RF regimes.[67,98] Until the semiconductor industry develops the technology to fabricate graphene devices with fully controlled properties, large-scale circuits based on graphene devices will not turn into real products.

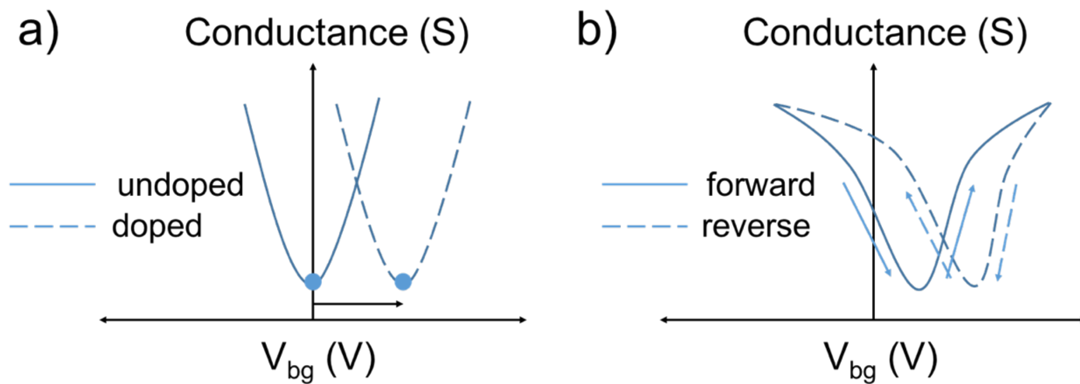

Figure 1-7 Transfer characteristic curves (conductance vs. gate voltage) of graphene FET. a) Undoped (intrinsic) graphene with Dirac point at zero gate voltage and doped graphene transistor with shifted Dirac point. b) Sweep direction-dependent hysteresis.

Despite its challenges, the idea of using graphene for a wide range of applications remains an alluring prospect because the advantage of graphene extends way beyond its high carrier mobility. In optoelectronics, for example, the high optical absorption, even in single layer graphene, combined with its excellent transport and optical properties has made graphene very attractive for low-footprint, high-bandwidth, and high-speed photodetectors and optical modulators.[99–107] The relative ease in tuning the Fermi level in graphene by using gate-controlled field enables a wide spectrum for light absorption. The high mobility in graphene and quantum capacitance made possible by the low-density of states result in capacitance control by gate-controlled carrier modulation and predicted high quality factor (Q-factor) variable capacitors[108–110] useful in wireless sensor applications

that are orders of magnitude smaller than microelectromechanical systems- (MEMS) based sensors. Having high mechanical strength and only one atom-thick layer, graphene has been predicted to be an excellent membrane material for salt water desalination that can be faster than the conventional reverse osmosis process[111] as well as channel material for flexible electronics.[62,65] The applications of graphene mentioned above are just the tip of the iceberg. The diverse applications of graphene are beyond the scope of this dissertation.

In the context of spintronics, graphene is very attractive due to its weak spin-orbit coupling and negligible hyperfine interaction. Because the electron spins are weakly coupled to their orbital motion, electrons should maintain their spin orientation over long distance while traveling in graphene. This has direct technological significance for spintronics-based circuit designs. In such circuits, the spin signals decay exponentially as $\exp(-d/\lambda)$, where d is the interconnect distance and λ is the spin diffusion length. To propagate spin signals over long distances in real circuitry, intermediate buffers would be needed to maintain the signal level. The long spin diffusion in graphene means that ASL circuits with graphene interconnects will require fewer buffers and reduced power overhead. Spin injection and transport in graphene was first demonstrated using two-terminal geometry[112] followed by demonstration using the nonlocal spin valve geometry[113] both at low and room temperatures. Since then, numerous work has been done in the study of spin phenomena in graphene. Theoretically, the fundamental physics of spin transport in graphene[114–122] as well as device and circuit level applications[123–125] is investigated. A lot of the experimental work focuses on improving the ferromagnet/graphene interface for improved spin injection efficiency and substrate condition, in addition to fundamental

demonstration of theoretical predictions.[120,126–155] The spin-Hall effect has also been investigated by intentional introduction of covalently bonded hydrogen atoms[156] and metallic adatoms[32] on graphene to enhance the spin-orbit coupling. Spin-transfer torque in graphene nonlocal spin valves has been demonstrated where the magnetization switching was assisted by application of external magnetic field.[157,158] Clearly, realizing graphene-based logic gates remains highly challenging. Spin injection into graphene is currently still limited by very low injection efficiency. Spin transport in the graphene channel has consistently shown spin relaxation times (~ 1 ns) that are orders of magnitude lower than predicted by theory (~ 1 μs). Transport properties in large-area graphene are clouded by defects, surface contamination, and other unknowns. Spin-transfer torque-induced switching has not been observed using reasonable current levels or without external magnetic field assistance. All of these and other challenges are active research areas currently being addressed by the scientific community.

1.4 Project overview

There are immense applications that graphene could play a role in due to its excellent properties. In this dissertation, our methods at investigating and manipulating some of the properties are explained. In this first chapter, the emergence of spintronics and how it evolves into a key player in post-CMOS technology was discussed. The interesting idea of using spin, instead of charge, as the state variable in logic gates was also discussed. Graphene and its properties were introduced to the reader starting from the electronics, optoelectronics, and sensor applications to their great potential in spintronics applications.

In the second chapter, our discussion will focus on spin injection and transport, specifically in semiconductors and graphene. Conductivity mismatch between the ferromagnet electrode and semiconductor or graphene, which is the main challenge that has been the limiting factor in the spin injection efficiency, will be discussed. The relaxation mechanisms of spins will be reviewed as well as the methods for determining the spin transport properties and origin of noise signals in spin transport experiments.

The third and fourth chapters are a summary of graphene-related work that has been performed in our lab. The graphene exfoliation method from highly ordered pyrolitic graphite similar to that of the Manchester group will be briefly explained. Our set-up of the chemical vapor deposition (CVD) system to grow large-area graphene will be shown and growth method and parameters discussed. Graphene used in our experiments is usually identified by Raman spectroscopy. Our fabrication method for graphene field-effect transistors (FET) and the measurement results will be elaborated. Our investigation of a chemical dopant, polyethyleneimine, to controllably dope graphene and hexamethyldisilazane pre-treatment of graphene FET substrates to reduce unintentional doping and suppress gate hysteresis will be summarized.

Spin transport experiment in graphene performed in our lab will be discussed in detail in chapter 5, starting with our nonlocal graphene spin valve device structure and the fabrication method including the tunnel barrier deposition. The measurement set-up for measuring such devices is also shown. Both the carrier density dependence and temperature dependence of the spin signals will be included in the discussion.

Chapter 6 will be started by review of the effect of in-plane electric field on the spin transport in semiconductors as predicted theoretically. The review of experimental manifestation of this effect on graphene spin devices will follow where it is shown that the electric field can be used to either enhance or suppress the spin signal. A method to manipulate the spin current flow by inducing doping asymmetry in the graphene channel will be proposed. Our experiments focus on the use of a double buried-gate structure, which consists of two closely separated back-gates, to control the doping asymmetry, and thus the spin current flow. The working mechanism, integration of this structure to the conventional nonlocal spin valves as well as the measurement results will be described. The electrochemical potential splitting in graphene that arises due spin injection from the ferromagnet electrode will be calculated using realistic empirical values.

Beyond graphene, other materials such as transition metal dichalcogenides and black phosphorus also have potential applications in spintronic devices. Our experiment results on charge transport in black phosphorus will be presented in chapter 7. The charge transport properties, although not a direct observation of the spin phenomenon, are usually a good indicator in predicting the spin phenomenon. In black phosphorus, which is also known to have excellent charge transport properties and weak spin-orbit coupling, the experimental results showing gate-controlled Schottky barrier height tuning for efficient spin injection are encouraging in the pursuit of spintronic research in this material.

Finally, the dissertation will be concluded. The purpose of the dissertation will be emphasized, which is to bring to the reader’s attention the interesting field of spintronics and its applications, the important role graphene plays in the future of spintronics, and the

possibility of utilizing other materials beyond graphene. The author is hopeful that the original works that are presented in the dissertation can lay the groundwork for some of the future research in this area, in addition to being an enjoyable source of information.

CHAPTER 2 SPIN INJECTION AND TRANSPORT IN SEMICONDUCTORS AND GRAPHENE

The very low spin current polarization commonly seen in semiconductor-based spintronic devices caused by the mismatch in the conductivity of the semiconductor and the ferromagnet and the tunnel barrier solution that has been adopted to solve the problem are reviewed. Spin relaxation mechanisms in semiconductors and metals that explain spin signals evolution in real measurements are discussed. Techniques for pure spin current detection, the nonlocal spin valve measurement and nonlocal Hanle measurement are reviewed. The possible origin of background signals typically present in such measurements is also reviewed. Finally, experimental works in spin injection into graphene as well as studies on the spin-orbit coupling in realistic graphene devices that have been reported in the literature are presented.

2.1 Spin injection into semiconductors and the conductivity mismatch problem

We have discussed the importance of spintronics devices as an alternative to CMOS in the first chapter. In this chapter, we will focus on the different aspects that are of importance in semiconductor-based spintronics devices. The choice of a semiconductor over metals as the channel material is often justified due to the longer spin relaxation time in semiconductors. In addition, the gate-controlled spin-orbit coupling on which the proposal of spin transistor by Datta and Das[159] was based caused the interest in

semiconductor channels to grow even more. The proposal highlights the importance of semiconductor channels and shall herein be briefly discussed. The spin transistor proposed was analogous to the electro-optic modulator shown in figure 2-1(a). In the electro-optic modulator, the polarizer at the input side polarizes the incoming light to 45 degrees relative to the y-axis in the y-z plane. The light then passes through the electro-optic material where the differential phase shift is controlled by the gate voltage applied by V_G. The light is detected at the output by an analyzer that lets the 45-degree polarized light through. The detected output power of the light is a function of the differential phase shift controlled by the gate. Similarly, in the spin transistor shown in figure 2-1(b), the output signal is also a function of the gate voltage. The polarizer and analyzer are replaced by ferromagnetic metal (in this case, iron) contacts. The light is replaced by electrons and the electro-optic material by a narrow-gap semiconductor InGaAs. While the gate voltage changes the dielectric constant of the polarized light in the modulator case, it produces electric field that changes the strength of the spin-orbit coupling due to Rashba effect in the spin transistor case. Obviously, in order for the spin transistor to work, these criteria must be met: 1) long spin relaxation time in the semiconductor, 2) electric field-controlled of spin-orbit coupling in the semiconductor, and 3) efficient spin injection into the semiconductor.[160] The control of spin-orbit coupling has been demonstrated in multiple semiconductors. The long spin relaxation time, although demonstrated by optical experiments, is still a challenge in practice, as we will discuss further in the case of graphene. In this section, we shall discuss in detail the third criterion, i.e. efficient spin injection into semiconductors.

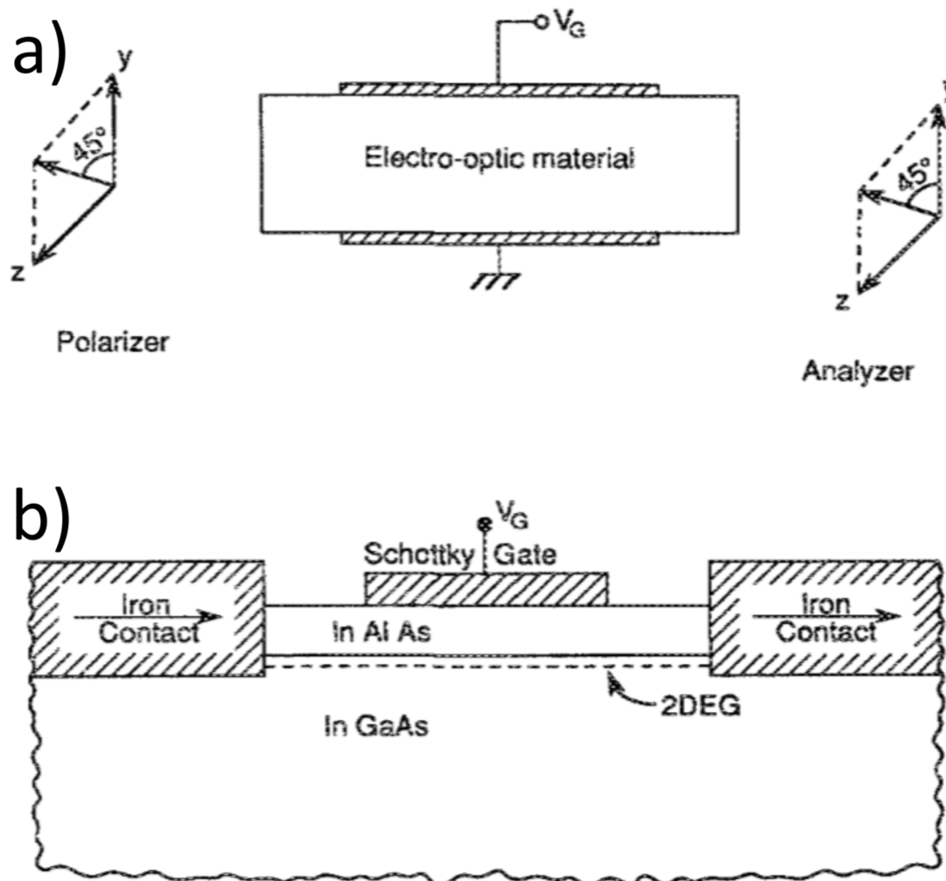

Figure 2-1 Datta-Das electro-optic modulator and spin transistor. a) Light is polarized by the polarizer before it passes through the electro-optic material, where the differential phase shift gets modulated by the gate voltage, and finally gets detected by the analyzer. b) Spin transistor analogous to the electro-optic modulator. The gate voltage changes the spin-orbit coupling in the semiconductor, effectively controlling the spin signal. Reprinted with permission from Datta and Das [159]. Copyright 1990, AIP Publishing LLC.

Efficient spin injection from a ferromagnet to nonmagnetic metals has been widely studied. After the earlier demonstrations at low temperatures[6–8,11], the first demonstration at room temperature[161] further prompted the interest in spin injection and detection in nonmagnetic metals. Unfortunately, spin injection into semiconductors suffered from low spin current polarization γ, defined as the ratio of the difference between the currents due to spin-up and spin-down electrons to the total current $\gamma = \frac{j_\uparrow - j_\downarrow}{j_\uparrow + j_\downarrow}$, which had been found

experimentally to be around 1% in semiconductors, more than one order of magnitude smaller than that of metals.[162,163] This low spin current polarization in the semiconductor makes it difficult to separate the spin injection from other effects, such as the stray field-induced Hall or magnetoresistance effect.[164,165] More importantly, the low spin current polarization makes the application using spin injection and detection in semiconductors impractical. It is therefore important to understand where the low spin current polarization comes from to be able to come up with a solution to improve it.

The spin injection through a ferromagnet/semiconductor junction can be analyzed by examining the materials on both sides of the junction. It should be emphasized the spin injection in our discussion is from electrical charge current passing through the junction, not from other mechanisms such as the optical spin injection using circularly polarized light and ferromagnetic resonance spin pumping. For the clarity of discussion, let us determine the position of the junction to be at $x = 0$, the ferromagnet to the left of the junction ($x < 0$), and the semiconductor to the right of the junction ($x > 0$), as shown in figure 2-2 (a). It has also been assumed that no Schottky barrier is formed at the ferromagnet/semiconductor interface. On the ferromagnet side of the junction, the electrical current can be perceived as consisting of two separate channels, one for each spin orientation. The two-current model states that at low temperatures with respect to the Curie temperature, the electrons in a ferromagnet can travel while maintaining their spin orientation. Therefore, the spin-up and spin-down electrons generating the current can be thought as moving in parallel inside the ferromagnet. Due to the difference in the band structures, the spin-up and spin-down electrons will generally have different conductivities.

An extreme example of this property can be observed in the case of half-metallic ferromagnet (HMF). In a half-metallic ferromagnet, the spin-up electrons display metallic behavior, while the spin-down electrons display semiconducting behavior. This results in the spin-up electrons being significantly more conductive and sole carriers of the current. The difference in the density of states between the two spin types implies that the electrical current is naturally spin polarized. However, this very same current, after passing through the ferromagnet/semiconductor junction, loses the spin polarization in the semiconductor.

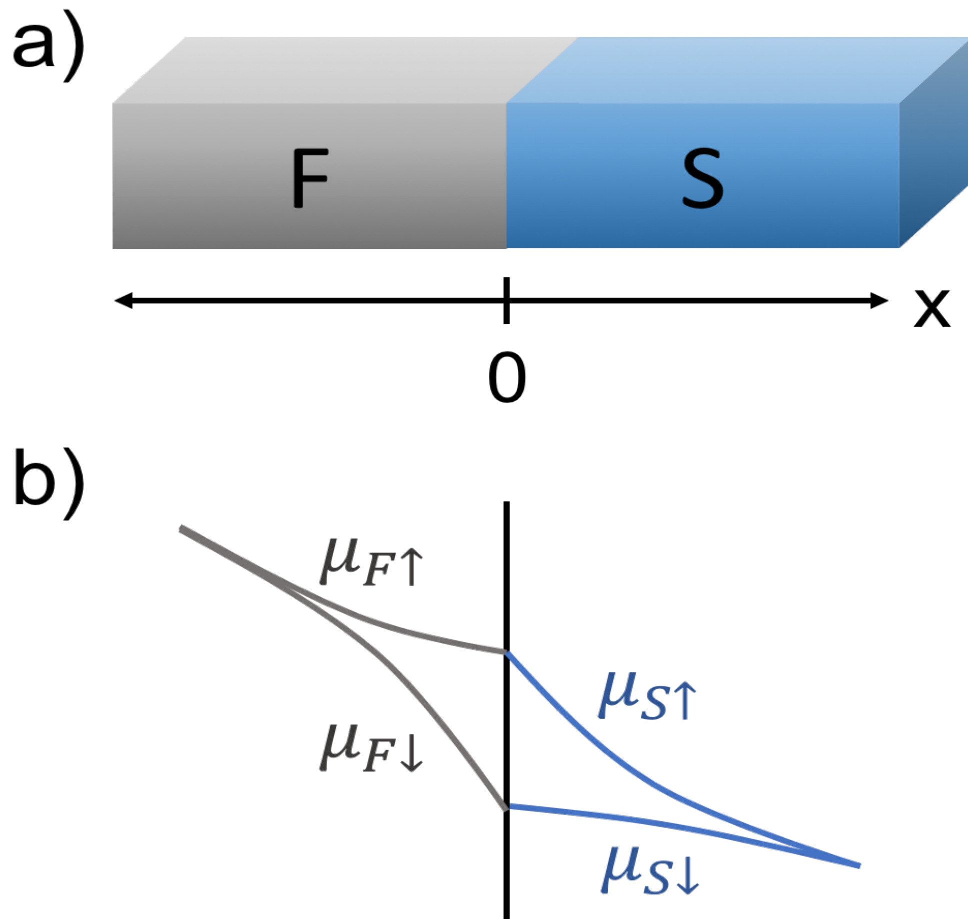

Figure 2-2 Ferromagnet/semiconductor structure assuming no Schottky barrier formation. a) Structure is shown with the interface at x = 0. b) Electrochemical potentials of the spin-up and spin-down electrons split at the interface while the difference between them vanishes far from the interface.

It was predicted by van Son *et al.*[166] that the distribution of the spin-up and spin-down electrons has to change when an electrical current flows across a ferromagnet/non-ferromagnetic metal junction. This prediction can be extended to the ferromagnet/semiconductor junction. Considering the one-dimensional case, the current density due to a specific spin type can be expressed as

$$j_\eta = \sigma_\eta \frac{\partial \left(\frac{\mu_\eta}{e}\right)}{\partial x} \qquad 2.1$$

assuming that the electrons stay in the local quasithermal equilibrium. In the equation, j_η, σ_η, and μ_η are the current density, conductivity, and electrochemical potential, respectively, due to spin type η (↑ or ↓) electrons. e is the electron charge and x is the position. It is possible to define separate electrochemical potentials for the spin-up and spin-down electrons as shown by figure 2-2 (b) because of the assumption that the spin scattering events happen at a much slower rate compared to the non-spin scattering events.[166,167] Far from the interface (junction) or at $x = \pm\infty$, both spin types are in equilibrium and the two electrochemical potentials merge. Near the interface, however, the electrons are driven out of the quasithermal equilibrium. The electrochemical potentials obey the diffusion equation

$$\frac{\mu_\uparrow - \mu_\downarrow}{\tau_s} = D \frac{\partial^2(\mu_\uparrow - \mu_\downarrow)}{\partial x^2} \qquad 2.2$$

where τ_s is the spin relaxation time, a measure of how long the electrons can travel before relaxing their spin orientation. $D = \frac{1}{3} v_F l$ is the diffusion coefficient, which is a function of v_F, the Fermi velocity and l, the electron mean free path. The diffusion coefficients can be

determined by $D_F = (1-\alpha_F)D_{F\uparrow} + \alpha_F D_{F\downarrow}$ in the ferromagnet and $D_{S\uparrow} = D_{S\downarrow} = D_S$ in the semiconductor. Let us now define the conductivity and current density contributions from the two spin types: $\sigma_\uparrow = \alpha\sigma$, $\sigma_\downarrow = (1-\alpha)\sigma$, $j_\uparrow = \beta j$, $j_\downarrow = (1-\beta)j$, where σ and j are the total conductivity and current density contributed by both spin types. Without loss of generalization, we can take the spin-up electrons to be the majority carriers of the current. α and j are the conductivity and current polarization. At the interface, α changes abruptly while j is continuous at the interface, assuming no strong spin relaxation event taking place at the interface. This means that not only the total current density is constant across the structure, but also the individual current densities.

Since the electron concentration in the ferromagnet is much larger than in the semiconductor, α in the ferromagnet (α_F) is taken to be independent of the current density and position.[167] On the semiconductor side, α_S is a function of the current density and position and can be expressed as the ratio between the majority spin population density to the total carrier density:

$$\alpha_S = \frac{n_{\uparrow S}}{n_{\uparrow S} + n_{\downarrow S}} = \frac{1}{(1 + e^{-(\mu_\uparrow - \mu_\downarrow)/kT})} \qquad 2.3$$

where k is the Boltzmann's constant and T the temperature. The current density of spin type η right at the interface (j_η^0) is a function of the electrochemical potential difference for spin type η ($\Delta\mu_\eta$) between the ferromagnet and the semiconductor:

$$j_\eta^0 = G_\eta(\Delta\mu_\eta/e) \qquad 2.4$$

where G_η is the interface conductance (consequently $1/G_\eta$ is the interface resistance) for electrons of spin type η. $\Delta\mu_\eta = \mu_{\eta 0^+} - \mu_{\eta 0^-}$; here $\mu_{\eta 0^+}$ and $\mu_{\eta 0^-}$ denote the

electrochemical potential for electrons of spin type η just to the right and left of the the interface, respectively.

Given the parameters above, i.e. the diffusion coefficient (D) and the spin relaxation time (τ_S), the spin diffusion length, a measure of how long electrons diffuse before relaxing their spin orientation, can be defined:

$$\lambda = \sqrt{D\tau_S} \qquad 2.5$$

Writing equation 2.2 in terms of the diffusion length and solving the differential equation with the appropriate boundary conditions, we obtain:

$$\mu_\uparrow - \mu_\downarrow = Ae^{\frac{x}{\lambda_F}}, x < 0 \qquad 2.6\text{ (a)}$$

$$\mu_\uparrow - \mu_\downarrow = Be^{-\frac{x}{\lambda_S}}, x > 0 \qquad 2.6\text{ (b)}$$

where λ_F and λ_S are the spin diffusion length of electrons in the ferromagnet and semiconductor, respectively. Right at the interface, the total current density can be split between the spin-up and spin-down current densities based on equation 2.4: $j_\uparrow^0 = \beta j = G_\uparrow(\Delta\mu_\uparrow/e)$ and $j_\downarrow^0 = (1-\beta)j = G_\downarrow(\Delta\mu_\downarrow/e)$. Here, the difference in the electrochemical potentials at the interface can be written as:

$$\Delta\mu_\uparrow - \Delta\mu_\downarrow = (\mu_{\uparrow 0} - \mu_{\downarrow 0})_+ - (\mu_{\uparrow 0} - \mu_{\downarrow 0})_-$$

$$\Delta\mu_\uparrow - \Delta\mu_\downarrow = B - A \qquad 2.7$$

where A and B are obtained by evaluating equations 2.6 (a) and (b) at $x = 0$. Rearranging equation 2.4 results in $\Delta\mu_\uparrow = \frac{ej_\uparrow}{G_\uparrow} = \frac{e\beta j}{G_\uparrow}$ and $\Delta\mu_\downarrow = \frac{ej_\downarrow}{G_\downarrow} = \frac{e(1-\beta)j}{G_\downarrow}$, which can be combined with equation 2.7 to give:

$$B - A = ej\left[\beta\left(\frac{1}{G_\uparrow} + \frac{1}{G_\downarrow}\right) - \frac{1}{G_\downarrow}\right] \qquad 2.8$$

Solving equation 2.1 for the for the ferromagnet side:

$$j = j_{\uparrow} + j_{\downarrow} = (\sigma_{\uparrow}\frac{\partial(\mu_{\uparrow}/e)}{\partial x}) + (\sigma_{\downarrow}\frac{\partial(\mu_{\downarrow}/e)}{\partial x})$$
$$ej = \alpha_F\sigma_F(\frac{\partial\mu_{\downarrow}}{\partial x} + \frac{A}{\lambda_F}e^{x/\lambda_F}) + (1-\alpha_F)\sigma_F(\frac{\partial\mu_{\uparrow}}{\partial x} - \frac{A}{\lambda_F}e^{x/\lambda_F})$$
$$ej = -\alpha_F\sigma_F(\frac{\partial(\mu_{\uparrow}-\mu_{\downarrow})}{\partial x}) + (\alpha_F\sigma_F\frac{A}{\lambda_F}e^{x/\lambda_F}) + \sigma_F(\frac{\partial\mu_{\uparrow}}{\partial x} - \frac{A}{\lambda_F}e^{x/\lambda_F})$$
$$+ (\alpha_F\sigma_F\frac{A}{\lambda_F}e^{x/\lambda_F})$$
$$ej = (\alpha_F\sigma_F\frac{A}{\lambda_F}e^{x/\lambda_F}) + \sigma_F(\frac{\partial\mu_{\uparrow}}{\partial x} - \frac{A}{\lambda_F}e^{x/\lambda_F})$$
$$\frac{ej}{\sigma_F} = (\alpha_F\frac{A}{\lambda_F}e^{x/\lambda_F}) + (\frac{\partial\mu_{\uparrow}}{\partial x} - \frac{A}{\lambda_F}e^{x/\lambda_F})$$
$$\frac{ej}{\sigma_F} = (\alpha_F - 1)\frac{A}{\lambda_F}e^{x/\lambda_F} + \frac{ej_{\uparrow}}{\sigma_{\uparrow}} = (\alpha_F - 1)\frac{A}{\lambda_F} + \frac{e\beta j}{\alpha_F\sigma_F}$$

where the last equation shown above is evaluated at the interface ($x = 0$), and after a simple rearrangement, can be written as:

$$\frac{ej}{\sigma_F}\left(\frac{\alpha_F - \beta}{\alpha_F(\alpha_F - 1)}\right) = \frac{A}{\lambda_F} \qquad 2.9\text{ (a)}$$

Similarly, for the semiconductor side, we obtain:

$$\frac{ej}{\sigma_S}\left(\frac{\alpha_S - \beta}{\alpha_S(\alpha_S - 1)}\right) = -\frac{B}{\lambda_S} \qquad 2.9\text{ (b)}$$

Recalling the definition of the spin current polarization γ, we can now express it in terms of β, which is itself related to 2.9 (a) and (b) as follows:

$$\gamma = \frac{j_{\uparrow} - j_{\downarrow}}{j_{\uparrow} + j_{\downarrow}} = 2\beta - 1$$
$$\gamma = \frac{(2\alpha_F - 1)R_F + (2\alpha_S - 1)R_S + (1/G_{\downarrow}) - (1/G_{\uparrow})}{R_F + R_S + (1/G_{\uparrow}) + (1/G_{\downarrow})} \qquad 2.10$$

where

$$R_{F,S} = \frac{\lambda_{F,S}}{\sigma_{F,S}\alpha_{F,S}(1-\alpha_{F,S})} \qquad 2.11$$

is just the sum of the bulk resistivities in the ferromagnet (F) or semiconductor (S) multiplied by its corresponding diffusion length.

We are finally at a place where we can trace the origin of low spin polarization of current injected from a ferromagnet into a semiconductor. When the ferromagnet and semiconductor are in good thermal contact, the interface resistance is small, which means that the $(1/G_{\downarrow})$ and $(1/G_{\uparrow})$ terms in equation 2.10 are small compared to R_F and R_S and are therefore negligible, leaving equation 2.10 simplified to:

$$\gamma \approx \frac{(2\alpha_F - 1)R_F + (2\alpha_S - 1)R_S}{R_F + R_S} \qquad 2.12$$

The spin diffusion length (λ) in ferromagnets (~10 nm) is typically smaller than in semiconductors (~1 µm). Furthermore, the carrier conductivity (σ) in ferromagnets is typically several orders of magnitude larger than in semiconductors, resulting in R_S being several orders of magnitude larger compared to R_F in equation 2.11. This results in the R_F term in equation 2.12 also being negligible, further simplifying the spin current polarization (γ) equation to:

$$\gamma \approx (2\alpha_S - 1) \qquad 2.13$$

In a normal semiconductor, the carriers are not spin polarized and the value of α_S is very close to ½. This in turn causes γ to have a very small value (approaching zero). This very low spin current polarization value that arises due to the large conductivity difference is what has come to be known as the “conductivity mismatch” problem for spin current

injection from a ferromagnet into a semiconductor. This has indeed been observed in many experiments involving spin injection into semiconductors.

Based on equation 2.10, the natural solution to the conductivity mismatch problem would be to increase the values of the $(1/G_{\downarrow})$ and $(1/G_{\uparrow})$ terms. If the $1/G$ terms are substantially larger compared to the other terms, it is then appropriate to consider the spin current polarization in equation to depend heavily on the $1/G$ terms, simplifying the equation to:

$$\gamma \approx \frac{G_{\uparrow} - G_{\downarrow}}{G_{\uparrow} + G_{\downarrow}} \tag{2.14}$$

Equation 2.14 implies that the spin current polarization should increase tremendously once the $1/G$ terms dominate. The interface conductances can be reduced by inserting a spin dependent insulating layer at the ferromagnet/semiconductor interface.[160] This insulating layer should take over the effective contact resistance at the interface and emerge as the main determinant of the spin current polarization. The value of the interface conductance is proportional to the density of states for each spin type and the different interface conductance values naturally arise due to the difference in the Fermi wave vector for each spin type in the ferromagnetic contact.[168] The insertion of a tunnel barrier at the interface could sometimes pose a high contact resistance problem. Careful engineering of the tunnel barrier is needed to achieve optimum contact resistance, or the resistance-area (RA) product, at the interface while preserving the spin filtering property. Such effort has been demonstrated, for example in the epitaxial Zn-doped MgO tunnel barrier,[169] which produced smaller band gap barrier, as well as the surface doping of Ge in the ferromagnet/insulator/n-Ge structure.[170] Another solution to the conductivity mismatch

problem besides tunnel barrier insertion is by engineering a Schottky barrier at the ferromagnet/semiconductor interface.[171] Both methods have been shown to enhance the spin current polarization.

The origin of the low spin current polarization was discussed. We have assumed in our discussion that the spin flip at the interface is negligible, which is a pretty reasonable assumption for realistic ferromagnet/semiconductor structures, with the exception of silicon, where a silicide layer is typically formed at the interface. Spin current across the interface was conserved while the spin-dependent conductivity was abruptly changed. We have seen that this caused the spin current polarization to vanish. Physically, this can be explained as follows. Due to the much higher resistance in the semiconductor, the injected spins tend to diffuse (sink) back into the ferromagnet upon injection into the semiconductor. The introduction of a tunnel barrier at the interface which dominates the effective resistance of the structure prevents the injected spins from seeing the lower resistance at the ferromagnet side. Experimentally, improvement in spin injection into semiconductors has been observed using both the tunnel barrier/ferromagnetic metal contact[172,173] and the Schottky barrier-type tunnel barrier.[174,175] Therefore, engineering of thin insulating layers with reduced resistance is important for future spintronics-based devices because not only it will increase the spin current polarization, but also the total injected current.

2.2 Nonlocal spin valves for pure spin current detection

2.2.1 Spin relaxation mechanisms

There are several spin relaxation mechanisms that are relevant for electrons in metals and semiconductors, such as the Elliott-Yafet, Dyakonov-Perel, resonant scattering

by local magnetic moments, Bir-Aronov-Pikus, and hyperfine-interaction mechanisms.[33,176] For the purpose of discussing the spin relaxation in graphene, the first two of the mechanisms listed above are briefly reviewed here. The Elliott-Yafet relaxation mechanism is dominant in materials with an inversion symmetry. In this mechanism, the spin relaxation occurs by ordinary momentum scattering from interaction with either phonons or impurities (or both) that induce spin-orbit coupling in the electron wave function. Due to the spacial inversion symmetry, the spin-orbit coupling does not break the degeneracy of spin-up and spin-down states. It does, however, introduce a small admixture of the opposite spin to a given spin state. In a metal, a nominally spin-up electron with a small admixture of spin-down spinor then has a finite probability of flipping its spin after typically around a thousand scattering events. Since the relaxation events occur during momentum scattering, the spin relaxation rate is then proportional to the momentum scattering rate:

$$\frac{1}{\tau_S} \approx \frac{b^2}{\tau_P} \qquad 2.15$$

In the expression above, τ_S and τ_P are the spin relaxation time and momentum relaxation time, respectively, and $b = \frac{\Lambda_{SO}}{\Delta \mathrm{E}}$ is the amplitude of the spin admixture, with Λ_{SO} being the amplitude of the matrix element of the spin-orbit coupling between the two states and ΔE the energy distance between the two adjacent states.

The Dyakonov-Perel mechanism takes place in materials that lack inversion symmetry. Materials that consist of two distinct types of atoms, for example III-V materials, are a good example where this mechanism is more prominent compared to the Elliott-Yafet mechanism, which is more prominent in elemental materials. In the absence of inversion

symmetry, the degeneracy of momentum states for the spin-up and spin-down electrons is broken. This spin splitting can be closely described by introducing an intrinsic magnetic field, around which electron spins precess at Larmor frequency. The electron experiences a magnetic field that changes in magnitude and direction at each scattering event. This essentially means that the electron is affected by randomly fluctuating spin-orbit induced magnetic field. Between each momentum scattering event, which happens every τ_P, the electron precesses by $\partial\phi = \Omega_{av}\tau_P$, where Ω_{av} is the average magnitude of the intrinsic Larmor precession frequency over the actual momentum distribution. During time t, t/τ_P momentum scattering events happen, after which the phase becomes $\phi(t) \approx \partial\phi\sqrt{t/\tau_P}$. Spin relaxation happens at t when $\phi(t) = 1$, which yields the spin relaxation rate:

$$\frac{1}{\tau_S} \approx \Omega_{av}^2\tau_P \qquad 2.16$$

This has the implication that is opposite to the Elliott-Yafet mechanism. In the Elliott-Yafet mechanism, the longer the momentum relaxation time is, the longer the spin relaxation time results. In the Dyakonov-Perel, the opposite is true. Since the spins dephase between scattering events, not during, the longer the momentum relaxation time is, the shorter the spin relaxation becomes.

2.2.2 Nonlocal resistance signal detection

In order to detect spin signal, a lateral spin valve as shown in figure 2-3 can be utilized. In this configuration, the magnetization direction of the first and second ferromagnets (FM1 and FM2) can be saturated in a particular direction by applying a large external magnetic field in the easy direction of the magnets. The spin signal can be

measured by injecting a spin polarized current that flows between FM1 and FM2 through the metal or semiconductor and simultaneously measuring the voltage between them while the external in-plane magnetic field is swept from a large negative value to a large positive value and also in the reverse direction. FM1 and FM2 have different dimensions and in the actual experiments, the width is typically varied. This results in FM1 and FM2 having different coercive fields. Sweeping the magnetic field in one direction changes the magnetization direction of the ferromagnet (FM1 or FM2) that has a smaller coercive field. When this happens, the two ferromagnets now have different and antiparallel magnetization directions and the voltage read between them changes. Further increasing the applied magnetic field beyond the coercive field of the second ferromagnet also changes its magnetization direction and the two ferromagnets once again have parallel magnetization. The voltage between them should also return to the original value.

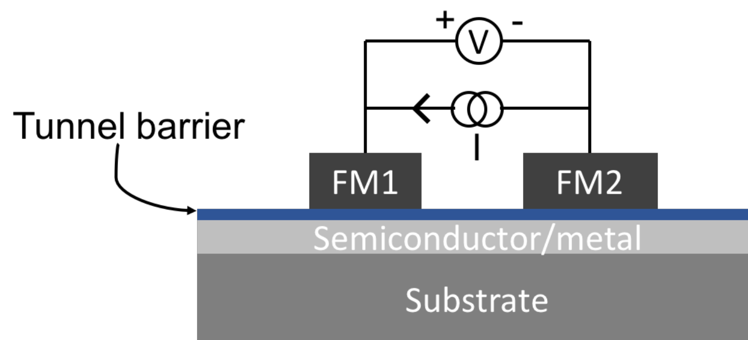

Figure 2-3 Lateral spin valve for spin signal detection. FM1 and FM2 have different widths and therefore different coercive fields. The voltage between them changes depending on their relative magnetization direction.

The lateral spin valve discussed above is referred to as the local spin valve. Although this geometry has been widely used to detect spin signals in metals or

semiconductors, it usually has a low signal-to-noise ratio. This is due to the typically small magnitude of the spin signals that needs to be detected on top of the much larger voltage that arises from the charge induced current. An alternative geometry to measure spin signals is the nonlocal spin valve, as shown by figure 2-4a, where the detection of the spin signals is completely separated from the charge current injection point. A minimum of four electrodes are needed in this configuration. The two remote contacts need not be ferromagnetic. In fact, it is usually more convenient to use nonmagnetic metal for the two remote contacts, NM1 and NM2. This also simplifies the signal analysis because only the two center contacts, FM1 and FM2, are affected by the magnetic field sweep during measurement. Here, the spin polarized current is injected by FM1 and flows towards NM1. Since the spin-polarized charge current only flows to the left of FM1, no charges flow towards FM2 and NM2. The spin-polarized charge current does, however, generate spin accumulation underneath FM1. Spins accumulated underneath FM1 then diffuse equally to the left and right of FM1 and relax after certain spin relaxation time τ_S, that depends on the channel material, substrate material, temperature, and/or other effects. Spin accumulation with only a small charge current spreading effect is detected between FM2 and NM2 and therefore, typically better signal-to-noise ratio is obtained in the spin signal measurement.

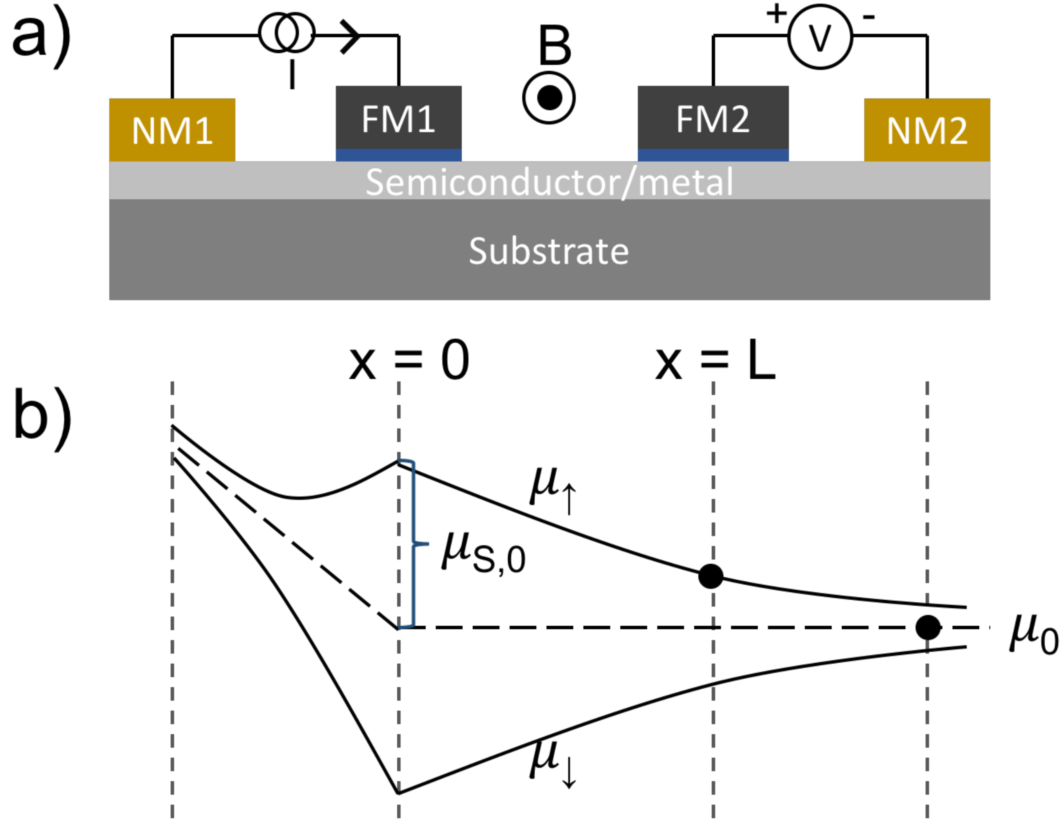

Figure 2-4 Nonlocal spin valve structure for pure spin current detection. a) Cross-section schematic. b) Electrochemical potential profile as a function of position in the nonlocal spin valve geometry in a).

The one-dimensional electrochemical potential profile is shown in figure 2-4b as a function of position in the nonlocal spin valve structure. Our following derivation focuses specifically on a two-dimensional channel and large interface resistances resulting from perfect tunnel barriers. The current injection point (FM1) is located at $x = 0$, while the voltage detection point at $x = L$. The distance between FM1 and FM2 is then equal to L. At $x = 0$, when the spin polarized current is injected, electrochemical potential imbalance appears, which shall be referred to as $\mu_{S,0}$, equal to its deviation from the equilibrium value. Given the magnitude of the injection current I and the injection efficiency P_i, the electrochemical potential split can be determined by

$$\mu_{S,0} = eP_iIR_S \qquad 2.17$$

In the high interface resistance limit that we have assumed, $R_S \ll (1/G)$, where R_S is the spin resistance and G the interface conductance. Since the accumulated spins diffuse equally to the left and right of FM1, the spin imbalance $\mu_{S,0}/2$ is considered for the detection by FM2. Taking into account the spin relaxation, the spin imbalance that actually arrives at FM2 and gets detected is

$$\mu_{S,L} = \left(\mu_{S,0}/2\right)e^{-L/\lambda} \qquad 2.18$$

which is given by the fact that spins decay exponentially as a function of distance and λ is the spin diffusion length. This electrochemical potential is detected as voltage by FM2 and its magnitude is related to the spin detection efficiency at FM2, P_d, by

$$V_{NL} = (P_d/e)\left(\mu_{S,L} - \mu_{S,\infty}\right) \qquad 2.19$$

The nonlocal voltage is due to the electrochemical potential difference between FM2 and NM2, as indicated by the black dots in figure 2-5b. Since NM2 is not spin-sensitive, we can safely equate the electrochemical potential at NM2 to $\mu_{S,\infty}$, which is equal to the equilibrium value. If the contact in NM2 is ferromagnetic, NM2 needs to be located far from FM2 (at least a few λ away) to maximize the spin signal. Therefore, given equation 2.17 the nonlocal voltage can be expressed as

$$V_{NL} = \pm\frac{P_iP_dIR_S}{2}e^{-L/\lambda} \qquad 2.20$$

The + (-) refers to the case where the magnetization directions of FM1 and FM2 are parallel (antiparallel) to each other. The spin resistance (R_S) can be determined if the sheet resistance and channel geometry are known by $R_S = \frac{R_{sq}\lambda}{W}$, where W is the channel width

and the sheet resistance R_{sq} is usually determined from charge transport measurement. It is more common to use a resistance unit to denote the spin signal, and therefore the nonlocal voltage is normalized to the injection current to yield nonlocal resistance (R_{NL}) in units of resistance

$$R_{NL} = \frac{V_{NL}}{I} = \pm \frac{P_i P_d R_{sq} \lambda}{2W} e^{-L/\lambda} \qquad 2.21$$

It should be noted, however, that this is not an actual resistance. It is merely the nonlocal voltage, which after being normalized to the injection current, carries the unit of resistance. Figure 2-5a shows the switching of the nonlocal resistance signal from the parallel to the antiparallel state and vice versa as the in-plane magnetic field is swept. The nonlocal resistance is positive when the ferromagnets are parallel to each other, and negative when they are antiparallel.

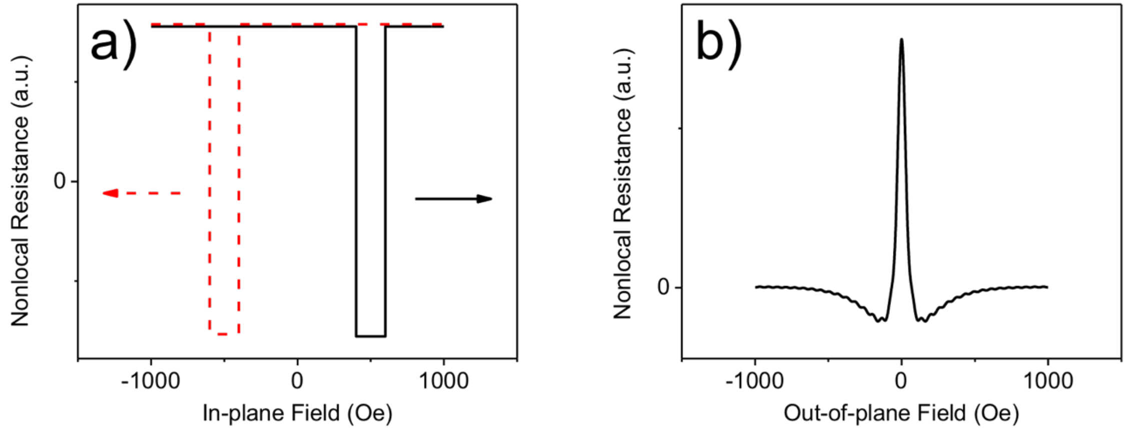

Figure 2-5 Nonlocal resistance as a function of in-plane and out-of-plane magnetic fields. a) Nonlocal resistance as a function of the in-plane magnetic field used to control the magnetization direction of the ferromagnets. b) Nonlocal resistance for the Hanle spin precession measurement as a function of the out-of-plane magnetic field. The figure illustrates the case when the ferromagnets have parallel magnetization.

2.2.3 Nonlocal Hanle spin precession

Another independent technique for pure spin current detection is the nonlocal Hanle spin precession measurement. This technique is widely applied in spin signal measurement because it not only involves direct manipulation of electron spins by the applied field but it also directly yields physical parameters, namely the diffusion coefficient and the spin relaxation time. It differs from the nonlocal spin valve measurement in that the magnetic field is applied out-of-plane and perpendicular to the spin polarization direction. This out-of-plane field, $B_{\perp}$, causes the injected spins to precess with a precession frequency equal to the Larmor frequency

$$\omega_L = \frac{g\mu_B B_{\perp}}{\hbar} \qquad 2.22$$

where g is the electron g-factor, μ_B the Bohr magneton, and $\hbar$ the reduced Planck's constant. Over time, the spin precession causes the electrons to lose their polarization. An electron spin that diffuses from $x = 0$ experiences random walk and can take any path to reach $x = L$. The time t it takes to arrive at $x = L$ depends on the particular path taken. For diffusive transport, the probability distribution for the arrival time is given as

$$\rho_D(t) = \frac{1}{\sqrt{4\pi Dt}} e^{\left(-\frac{L^2}{4Dt}\right)} \qquad 2.23$$

with D being the diffusion coefficient of the electrons. When the spin relaxation is taken into account, equation 2.23 should include the exponential decay function and be modified to $\rho_D(t)e^{-t/\tau_S}$. Again, because the diffusion is a random process, the potential at $x = L$ given an out-of-plane magnetic field of strength B is given by $\mu_{S,L}(B)$ which is a sum over all possible arrival times. Therefore,

$$\mu_{S,L}(B) = 2\sqrt{\frac{D}{\tau_S}}\int_0^\infty dt\,\rho_D(t)e^{-t/\tau_S}cos(\omega_L t) \qquad 2.24$$

and the pre-factor $2\sqrt{\frac{D}{\tau_S}}$ arises due to the boundary condition that $\mu_{S,L=0}(B = 0) = \mu_{S,0}$. The nonlocal voltage (still with the assumption of a highly resistive interface) can then be determined from equation 2.19, and after normalization to the injection current, the following equation for the nonlocal resistance is obtained:

$$R_{NL} = \pm\frac{P_i P_d R_{sq}}{W}\int_0^\infty \sqrt{\frac{D}{4\pi t}}e^{\left(-\frac{L^2}{4Dt}\right)}\cos(\omega_L t)\,e^{\left(-\frac{t}{\tau_S}\right)}dt \qquad 2.25$$

Equation 2.25 has three main terms that are evaluated by the integral sign and these three terms are:

1) $\sqrt{\frac{D}{4\pi t}}e^{\left(-\frac{L^2}{4Dt}\right)}$, representing the spin diffusion;
2) $\cos(\omega_L t)$, representing the spin precession; and
3) $e^{\left(-\frac{t}{\tau_S}\right)}$, representing the spin relaxation.

The physics of the spin diffusion, precession, and relaxation are well captured by equation 2.25 and the effect of the out-of-plane magnetic field on the nonlocal resistance is illustrated in figure 2-5b. In the figure, only the parallel case is shown. The antiparallel case is simply the mirror image of the curve relative to the y = 0 line. In real device analysis, equation 2.25 can be solved numerically and used to fit experimental data to extract the fitting parameters, i.e. the diffusion coefficient and spin relaxation time.

2.2.4 Nonlocal baseline resistance value due to Peltier and Seebeck effects

In the nonlocal spin valve geometry, we have seen that the charge current path (FM1 to NM1) is completely separated from the spin signal detection (FM2-NM2). The nonlocal voltage, and equivalently nonlocal resistance, detected between FM2 and NM2 should therefore equal zero in the absence of spin signal. When there is spin current present, based on equation 2.21, the nonlocal resistance should have spin signal that is positive when the ferromagnets are in parallel configuration, and spin signal that is equal in amplitude but opposite in polarity when the ferromagnets have antiparallel magnetization. This is usually not the case in real data generated from experiments.

Contrary to expectation, the nonlocal resistance signal typically has a nonzero baseline value, a phenomenon which is even more prominent in spin valves with semiconductor channels. Johnson and Silsbee[177] argued that the nonzero baseline resistance could be due to nonuniformity in the current injection along the channel width. If the current from FM1 to NM1 is injected uniformly across the channel width, by symmetry, there should be no potential built up to the right of the injection point because the electrons that stray to the right will be canceled out by electrons flowing to the left due to the opposing space-charge field within a mean free path of the electrons. This is no longer true for nonuniform current injection and the spreading of this local current can cause baseline nonlocal voltage (or Ohmic resistance) detected by FM2, which should decay exponentially as FM2 gets farther apart from the injection point (FM1) by $V_R \propto e^{-\frac{\pi L}{W}}$. The nonuniform current injection can take place in the highly-resistive-interface case due to nonuniform thickness of the tunnel barrier. In the high interface conductance limit, the

same effect could arise because the current is mostly injected through some preferred edge of the channel rather than uniformly along the channel width.

While the exponential dependence agrees well with experimental data for small separations between FM1 and FM2, Bakker *et al.*[178] found that at larger separations, the baseline nonlocal resistance decreases more slowly and the exponential dependence no longer holds. The almost linear dependence on the separation was attributed to the Peltier and Seebeck effects in their experiments. At FM1, due to the difference in the Peltier coefficients between the ferromagnet and channel material (either nonmagnetic metal or semiconductor), heat is absorbed or accumulated at the interface. Although the charge current is continuous across the interface, the heat current is not and depends on the Peltier coefficient mismatch. This in turn generates heat current that gets carried along the channel away from FM1, both to the left and to the right. When this heat current arrives at FM2, the temperature gradient at the interface gets converted to a potential difference by the Seebeck effect. Using their thermoelectric model, Bakker *et al.* were able to show excellent agreement between their calculation and experiment results. The nonlocal baseline resistance is then determined as the sum of the Ohmic resistance due to the local current spreading and the thermoelectric effect due to the interplay between the Peltier and Seebeck effects.

2.3 Spin injection and transport in graphene

2.3.1 Tunnel barriers for efficient spin injection into graphene

Studying the spin transport properties in a material requires the ability to first inject spin polarized electrons into the material. Spin injection into graphene has been challenging

and the injection efficiency has mostly been low. This is because spin injection into graphene also suffers from the conductivity mismatch problem encountered by spin injection into semiconductors, as we have seen earlier. Here we shall review the different attempts that have been made to study the spin injection into graphene.

Spin injection into graphene in direct contact with a ferromagnetic metal has indeed been shown to yield very low spin injection efficiency. This direct contact, or usually referred to as transparent contact, highlights the problem with the conductivity mismatch between graphene and the ferromagnetic metal. In their experiments, Han *et al.*[130] deposited Co as the ferromagnetic metal directly on graphene. A masking layer of MgO was used to reduce to contact width to achieve higher spin signal. The resulting resistance-area (RA) products, a measure of the contact or interface resistance, are small ($< 30\ \Omega\mu m^2$), as expected for good thermal contact between graphene and Co. Using the transport distance dependence of the nonlocal resistance signal in equation 2.21, a spin diffusion length of ~1.6 μm was obtained. This spin injection and transport was also confirmed using the Hanle nonlocal measurement, from which they extracted a spin relaxation time of 84 ps and a spin diffusion length of ~1.5 μm, similar to the value obtained by the transport distance dependence. Furthermore, a very low spin injection efficiency of ~1% was obtained, which should be expected due to the high interface conductance of the device.

Based on our earlier discussion, inserting an oxide layer between the graphene and the ferromagnetic metal should help improve the spin injection efficiency into graphene. Indeed, the first demonstration of nonlocal resistance signal in graphene at room temperature by Tombros *et al.*[113] showed a spin injection efficiency of ~10%. Al_2O_3 layer

was used as the tunnel barrier this case and Co was used as the ferromagnetic contact. In other experiments where the spin polarized current was also injected through an Al_2O_3/Co contact,[128,132,133] similar spin injection efficiency values were also reported. The improvement compared to the case of transparent contact is apparent.

The tunnel barriers used in the experiments above are very thin (~1 nm) to allow a substantial amount of current to tunnel through and enter the graphene. The very thin nature of the tunnel barrier poses some challenges. The most obvious challenge is whether the deposited tunnel barrier is uniform everywhere. It turns out that due to the high surface diffusion on graphene, the as-deposited tunnel barrier most likely consists of pinholes. Different techniques have been developed to deposit uniform tunnel barriers on graphene. For example, it has been found by Dlubak *et al.*[137] that a thin Al_2O_3 film deposited on graphene by evaporation of Al and oxidation in O_2 atmosphere is usually granular in nature because of the tendency of the Al atoms to cluster together, as also reported by Popinciuc *et al.*[133] This results in pinholes in the Al_2O_3 layer. The deposition of Al_2O_3 by sputtering of Al, however, seems to increase the uniformity and reduce the surface roughness, as shown by figure 2-6. It is unclear why sputtered Al forms more uniform layer compared to the evaporated case. In the case of MgO tunnel barrier, Wang *et al.*[129] have shown that depositing MgO directly on graphene also results in the clustering of the oxide and therefore the formation of pinholes. The roughness of the 1-nm MgO film deposited directly on graphene was found to be ~0.8 nm. By depositing a 0.5 monolayer of Ti before the MgO deposition, they were able to reduce the roughness to ~0.2 nm, which is close to the atomic spacing of MgO and suggests the formation of atomically smooth MgO film.

These improved methods for tunnel barrier deposition have indeed increased the spin injection into graphene. Using the Al_2O_3 tunnel barrier deposited by sputtering of Al and oxidizing in oxygen environment, Cubukcu *et al.*[153] observed an increase in both the spin injection efficiency (~32%) and the nonlocal resistance signal (~400 Ω) at 10 K. Han *et al.*[134] showed that the spin injection efficiency increased to ~30% and the nonlocal resistance signal to ~130 Ω when the MgO tunnel barrier used in their experiment was deposited on top of Ti seed layer.

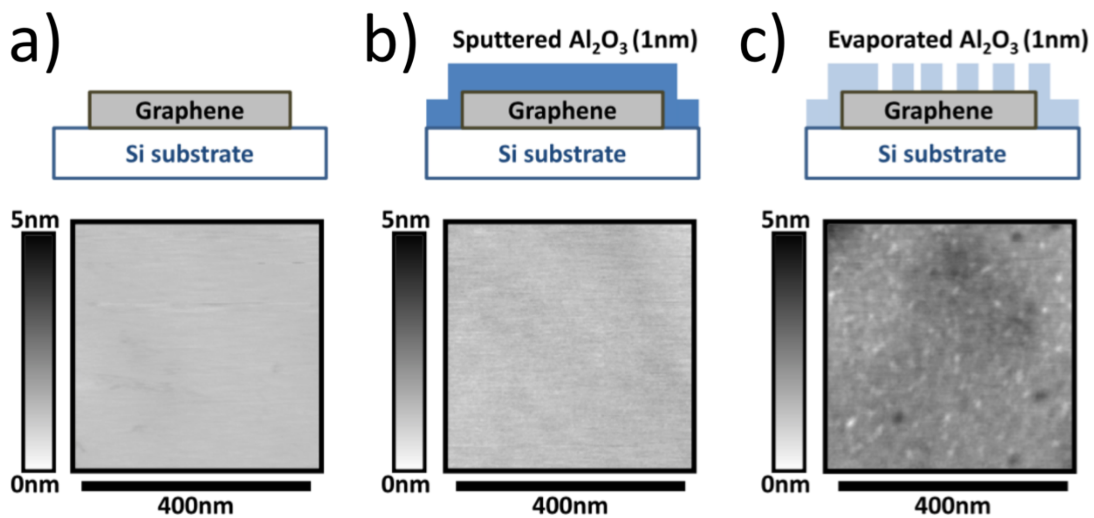

Figure 2-6 Illustration of the surface topography of and comparison of surface roughness before and after Al_2O_3 deposition. Comparison shown between a) graphene, and Al_2O_3 on graphene formed by b) sputtering and c) evaporation of Al. Reprinted with permission from Dlubak et al. [137]. Copyright 2012, AIP Publishing LLC.

Choosing the optimum tunnel barrier deposition method can be tricky. For example, while sputtered Al provides more uniform Al_2O_3 formation than evaporated Al, the act of sputtering can damage the graphene, offsetting the potential advantage. Evaporated Al, though a gentler process, results in clustered, pinhole-type Al_2O_3 formation. The Al_2O_3 film would need to be at least 5 nm thick[155] to eliminate pinholes and even then the tunnel

barrier thickness may not be uniform everywhere. Evaporated MgO on Ti seed layer has the advantage of uniform formation on graphene as well as causing minimal damage to the graphene surface. However, its reactive nature could complicate the handling of the material during processing. Alternative methods for tunnel barrier deposition that were not included in our discussion include: 1) atomic layer deposition (ALD) of Al_2O_3 on functionalized graphene[141] (to promote adhesion of Al_2O_3), 2) hexagonal boron nitride,[150] 3) TiO_2,[149] and 4) amorphous carbon,[147] among others, all of which have been shown to yield higher spin injection efficiency than the transparent contact case and are worth further investigating. The thinness of these films not only poses a problem with the film uniformity, but also the robustness. These thin films tend to break down after a few cycles of the device operation or after a relatively large current application, a problem that is worsened by the imperfection of the film, as the breakdown typically starts and escalates from the defect sites. A uniform, defect-less film therefore has a two-fold benefit, i.e. increased spin injection efficiency and enhanced robustness. Neumann *et al.*[147] reported that they were able to pass a 400 μA current through their ~0.1 μm^2 amorphous carbon tunnel barrier without causing breakdown. The robustness of aforementioned tunnel barriers can all potentially be enhanced as well by improving the uniformity. Spin injection into graphene is not the only important factor that needs to be considered in graphene spintronic devices. What happens after the spins are injected is also a key factor as we shall see in the next section.

2.3.2 Spin-orbit coupling in graphene

The major advantage that graphene possesses which makes it appealing for spintronic devices is its long intrinsic spin relaxation time, which is the result of weak spin-orbit coupling and negligible hyperfine interaction in atomic carbon. The earliest prediction of the spin-orbit coupling induced gap in graphene was given by Kane and Mele[179] in 2005. In their calculation based on the first order degenerate perturbation theory, they crudely estimated an intrinsic spin-orbit coupling (SOC) induced gap of ~100 μeV. More detailed calculations based on the tight-binding theory and *ab initio* calculations[180,181] revealed that the SOC induced gap in graphene should be around 1 μeV. This value was supported by first-principles calculations by Yao *et al.*[182] in 2007, which was also explained using the tight-binding model.

All of the detailed calculations performed above[180–182] assumed that the SOC originated from the *s* and *p* orbitals. Interestingly, it had been argued by Slonczewski and Weiss[44] in 1958 that the *p* orbitals contributed in the second order, while the nominally unoccupied *d* orbitals contributed in the first order to the spin-orbit induced gap in graphene. This is due to in the absence of spin-orbit coupling, p_z orbitals which form the states at K (K') points of the Brillouin zone do not hybridize with p_x and p_y orbitals. They do, however, hybridize with d_{xz} and d_{yz} orbitals, which are split by SOC. The hybridized orbitals form the π-band with increased SOC induced gap at the Dirac point. This was confirmed by the first-principles calculations performed by Gmitra *et al.*[183] where they obtained SOC induced gap of ~24 μeV. In another set of first-principles, all-electron density functional theory (DFT) calculations,[184] the SOC induced gap was found to be twice as large or ~ 50

μeV. Both these calculations considered the effect of the *d* orbitals. Konschuh *et al.*[116] successfully showed in their tight-binding calculations that the intrinsic SOC induced gap in graphene is indeed a second-order function of the SOC from the *p* orbitals and first-order function of the SOC from the *d* orbitals. In their calculations, the *p* orbitals alone induced a gap of ~1 μeV, while the *d* orbitals contributed ~23 μeV to the intrinsic SOC induced gap. These values are very much consistent with the previously reported values. They also pointed out that the discrepancy between the values reported by Gmitra *et al.*[183] and Boettger *et al.*[184] could be due to the idiosyncrasies of the *ab initio* codes used in the calculations and the actual value could range between ~25 to 50 μeV.

Besides the intrinsic origin, the SOC could also arise due to an extrinsic source in the form of electric field perpendicular to the graphene plane. This electric field could originate from different sources, such as applied gate voltage or charged impurities in the substrate, and its presence breaks the spatial inversion symmetry of graphene and therefore modifies its band structure. Specifically, the resulting extrinsic SOC causes the spin-splitting of the conduction and valence bands similar to the Bychkov-Rashba effect. In contrast to the intrinsic case, the extrinsic SOC induced gap is weakly dependent on the SOC of the *d* orbitals and strongly dependent on the SOC of the *p* orbitals. The SOC then is mainly due to the coupling of the $\sigma - \pi$ bands and the induced gap is linearly dependent on the electric field. The experimental demonstration of the linear dependence has also been reported.[149] Similarly, it has been calculated that the presence of miniripples in graphene, for example due to substrate topography, or lattice defects, strains, and curvature could also lead to an increase in the SOC induced gap. Gmitra *et al.*[183] showed in their

calculation that the SOC induced gap (Δ_I) increases as a function of the lattice deformation (δa) with respect to the lattice constant, as shown in figure 2-7, where the the results were shown both with *d* orbitals inclusion and without. It is obvious that the *d* orbitals change only the intrinsic SOC without any lattice deformation and the rate of the SOC change is unaffected by the presence of *d* orbitals. It can be concluded then that the SOC induced gap is solely due to the $\sigma - \pi$ mixing similar to the electric field effect. It should be noted that in the original work (figure 2-7), the y-axis ($2\lambda_I$) denotes (Δ_I) and the x-axis (Δ/a) denotes the lattice deformation ($\delta a/a$).

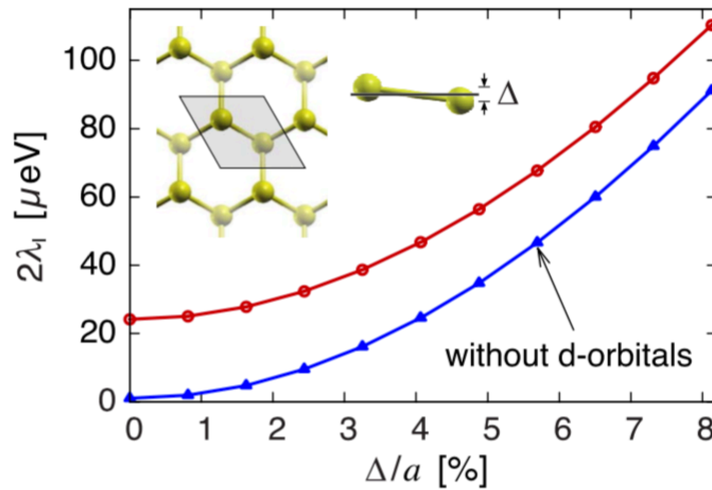

Figure 2-7 Calculated SOC as a function of the lattice deformation in graphene with (red) and without (blue) the inclusion of the SOC from d orbitals. The SOC change is independent of the d orbitals and solely due to the $\sigma - \pi$ mixing. Reprinted figure with permission from Gmitra et al. [183]. Copyright (2009) by the American Physical Society.

The intrinsic and extrinsic SOC discussed above can cause the spins to relax in graphene, either by the Elliot-Yafet or Dyakonov-Perel mechanism. Experimental methods have been developed to determine the main spin relaxation mechanism in graphene. It seems that many experimental results have pointed to Elliot-Yafet as the main mechanism

for spin relaxation in graphene,[113,133,135,152] which agrees with the prediction due to the presence of an inversion symmetry as discussed in the previous section. Huertas-Hernando, *et al.*[115] argued, however, that in actual graphene spin valve devices, the presence of adatoms modifies the SOC in graphene that favors the Elliot-Yafet mechanism. In their calculations where they considered the Rashba type SOC as the main contributor to the spin relaxation, they argued that in ultra clean graphene, the Dyakonov-Perel mechanism as well as the gauge fields due to ripples in graphene should dominate over the Elliot-Yafet mechanism. This is a reasonable take on the problem at hand since in real graphene spin valve devices the substrate effect is strong and ripples are most likely present. This prediction remains to be experimentally demonstrated in the future as it seems that the ability to produce ultra clean graphene has yet to be realized. It is also worth mentioning that a different spin relaxation mechanism due to magnetic defects has recently been proposed that explains the orders-of-magnitude faster spin relaxation rate in real graphene spin valve devices.[185] The idea is that at resonant energy a scattering electron can move around a scattering site centered at a magnetic impurity that provides spin flip exchange field to the electron before it escapes with equal probability to be either in spin-up or spin-down state. Consistent with this proposal, Kochan *et al.*[186] showed that using hydrogen atoms as magnetic scatterers in graphene, the spin relaxation time is reduced significantly to ~100 ps for only 1 ppm magnetic impurity concentration.

In the presence of adatoms, it has been shown that the SOC in graphene is a few orders of magnitude stronger, comparable to the value found in diamond and zinc blende semiconductors.[119,187] The adatoms serve as momentum scattering centers, reducing the

momentum scattering time and consequently the spin relaxation time, suggesting the Elliot-Yafet mechanism is the dominant spin relaxation mechanism. The adatoms break the inversion symmetry in graphene and their interaction with carbon atoms induces *sp³* hybridization. The SOC strength depends on how much the carbon atoms are displaced from the graphene plane during the *sp³* hybridization. In their experiments, Balakrishnan *et al.*[156] showed that by introducing hydrogen dopants on graphene, the SOC increased significantly to ~2.5 meV, or about two to three orders of magnitude larger than in intrinsic graphene. Moreover, they also demonstrated that in chemical vapor deposited graphene, the accidental residual copper adatoms on graphene (the origin of this will be explained in the next chapter) can act as strong spin scattering centers, increasing the SOC strength to ~20 meV[32] leading to the observation of Giant spin Hall effect in graphene. It should be noted that an earlier investigation by Han *et al.*[138] suggested that mobility change without the change in carrier concentration, while strongly affecting the momentum scattering time, has little effect on the spin scattering time. It also seems that not all adatoms are effective spin scatterers, as reflected in the experiment results by Pi *et al.*[188] which showed that while Au adatoms cause significant momentum scattering, they do not scatter spin as effectively. Even more surprisingly, they found that Au adatoms increase the spin relaxation time by a factor of ~3, which they attributed to the inhibition by Au adatoms of the lattice defects or edge sites that may otherwise contribute to spin scattering.

The actual dominant spin relaxation mechanism in graphene remains elusive. In the intrinsic case, both the Elliot-Yafet and Dyakonov-Perel mechanisms should yield a spin relaxation time of ~1 μs,[176] or about 3-4 orders of magnitude longer that 100 ps – 1 ns spin

relaxation times observed experimentally. The resonant scattering mechanism offers an explanation for the significantly shorter spin relaxation time in the presence of magnetic impurities. The Elliot-Yafet mechanism has been shown to dominate when charged impurities or adatoms distort the graphene lattice and convert the sp^2-bond to sp^3-bond, significantly increasing the SOC. In the case of ultra clean graphene surface, the Dyakonov-Perel mechanism and gauge fields due to curvature in graphene were predicted to be the dominant spin relaxation mechanism. Experimentally, it has been suggested that using atomically flat hexagonal boron nitride (h-BN) as a substrate for the graphene spin valve can significantly enhance the carrier mobility as well as diffusion coefficient. As a result, the spin diffusion length increases while the spin relaxation time remains unchanged. This shows that in graphene with minimum curvature, the spin relaxation is most likely not due to the substrate, but the impurities on the surface. It was also pointed out in the same work that the spin relaxation might have been due to roughly equal contribution by both the Elliot-Yafet and Dyakonov-Perel mechanisms.[142] In the case where the graphene is encapsulated by h-BN, an increase in the spin relaxation time was observed in addition to the increase in diffusion coefficient, probably due to less impurities in the encapsulated region of the graphene.[149] The ability to control the graphene condition as well as the measurement environment is of extreme importance in order to be able to truly understand the spin transport physics in graphene. In the next two chapters, the process of graphene production, its material characterization, and also the charge transport measurement are discussed which will help to understand where some of the impurities come from and how they affect graphene's properties.

CHAPTER 3 SYNTHESIS AND IDENTIFICATION OF GRAPHENE

In chapter 2, we have looked at some of the limitations to semiconductor spintronic devices, for example the conductivity mismatch that suppresses the spin current polarization and spin-orbit coupling due to external effects, in addition to the intrinsic spin orbit coupling, that may be responsible for the orders-of-magnitude shorter spin relaxation times compared to the theoretical prediction. Many works specifically on graphene were reviewed highlighting some of the significant progress made in the first decade after the first spin signal demonstration in graphene. In the present chapter, we will take a step back and review the methods that have made all the progress possible, the synthesis of graphene itself. There are several ways for producing graphene, e.g. exfoliation of bulk graphite, chemical vapor deposition (CVD) on metal substrates, epitaxial growth on SiC, carbon nanotube slicing, etc. In our experiments, graphene was produced both by the exfoliation and CVD methods, and therefore these two methods will be reviewed in more detail. Atomic force microscopy (AFM) and Raman spectroscopy methods to identify and characterize graphene after production will also be reviewed.

3.1 Graphene exfoliation from highly oriented pyrolitic graphite

In their paper published in 2004, Novoselov *et al.*[43] reported their work on electric field effect on monocrystalline graphitic films that are a few atoms thick with a height difference of ~0.4 nm between two adjacent films, approximately equal to the diameter of a carbon atom (~0.3 nm). This marked the first time a two-dimensional film was isolated

that was stable under ambient conditions. The films were prepared by repeated peeling of small mesas originating from highly oriented pyrolitic graphite (HOPG) source using scotch tape pieces. This method of isolating graphene layers has come to be known as the scotch-tape method or mechanical exfoliation method.

We too utilized the mechanical exfoliation method in preparing the graphene used in some of the experiments discussed in this dissertation. Only a few materials are needed in the process, namely the HOPG source, scotch tape, SiO_2-on-Si substrate, and a pair of tweezers. The SiO_2 needs to have a suitable thickness (typically ~90 nm or ~300 nm) for it to have the right optical reflection, which is important in identifying the graphene flakes later. The exfoliation process, which is summarized in figure 3-1, is done as follows:

a) A piece of scotch tape is put on the HOPG source and rubbed gently using the blunt end of the tweezers,
b) The scotch tape, which now has some HOPG stuck on it, is removed from the HOPG source,
c) The scotch tape with HOPG is put on another piece of fresh scotch tape and rubbed gently using the blunt end of the tweezers before being peeled apart. This step is done multiple times until the remaining HOPG on the scotch tape is thin or semi-transparent,
d) The scotch tape that has thin HOPG on it is put on top of the clean SiO_2-on-Si substrate and rubbed gently using the blunt end of the tweezers,
e) The scotch tape is removed from the substrate leaving a HOPG trace on the substrate.

Right before carrying out step d) above, the substrate has typically been baked on a hot plate at 150 ºC for 30 minutes to minimize the residual moisture that might later on be trapped underneath the graphene layer after exfoliation and act as a source of accidental dopants. It is not possible to precisely control the size, shape, location, or thickness of a flake since the process is for the most part a random process.

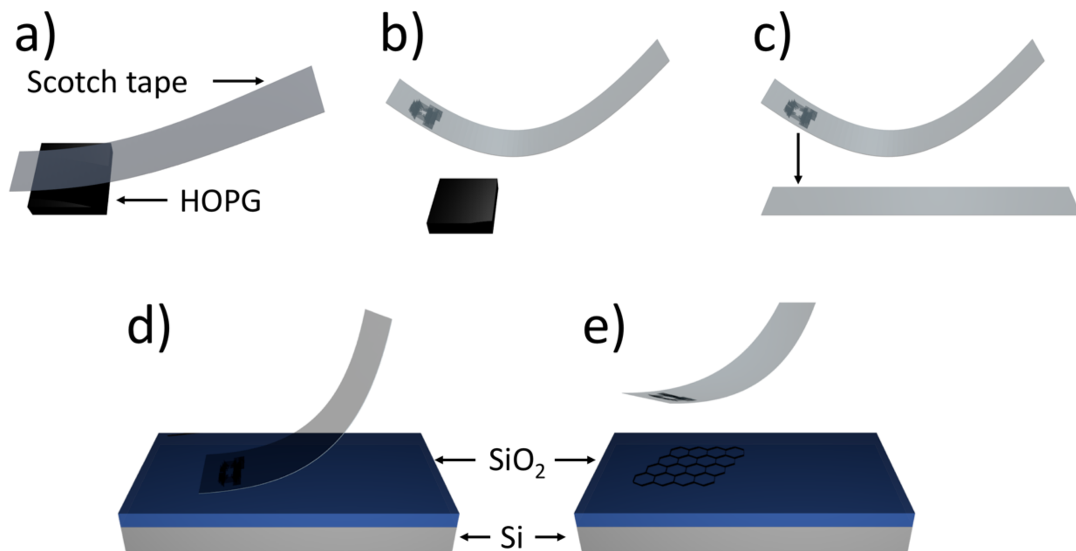

Figure 3-1 Sequence of steps for the scotch-tape method or mechanical exfoliation of graphene layers from HOPG. The descriptions for each step are available in the main text.

After the mechanical exfoliation process has been completed, the next step is to search for graphene flakes using a microscope and to identify the flakes that may be useful. Since graphene layers of interest are typically very thin (between a few angstroms to a few nanometers), they are not easily visible under the microscope. Preparing graphene devices for experimental studies unarguably requires the ability to visually observe graphene using optical microscopy, which generally utilizes a white light source. This is why a substrate with the right oxide thickness is needed to create a difference in the interference colors of

the reflected light from the graphene compared to the substrate. Figure 3-2 shows an example of an optical micrograph of few-layer graphene on 300 nm SiO_2 substrate. Even with the right oxide thickness, it is still quite challenging to scan through and visually inspect the sample using an optical microscope in search for flakes usable for making devices or material characterization. It has been reported by Blake *et al.*[189] that when a monochromatic illumination is used instead of a white light source, graphene layers can be distinguishable from the SiO_2 substrate regardless of its thickness.

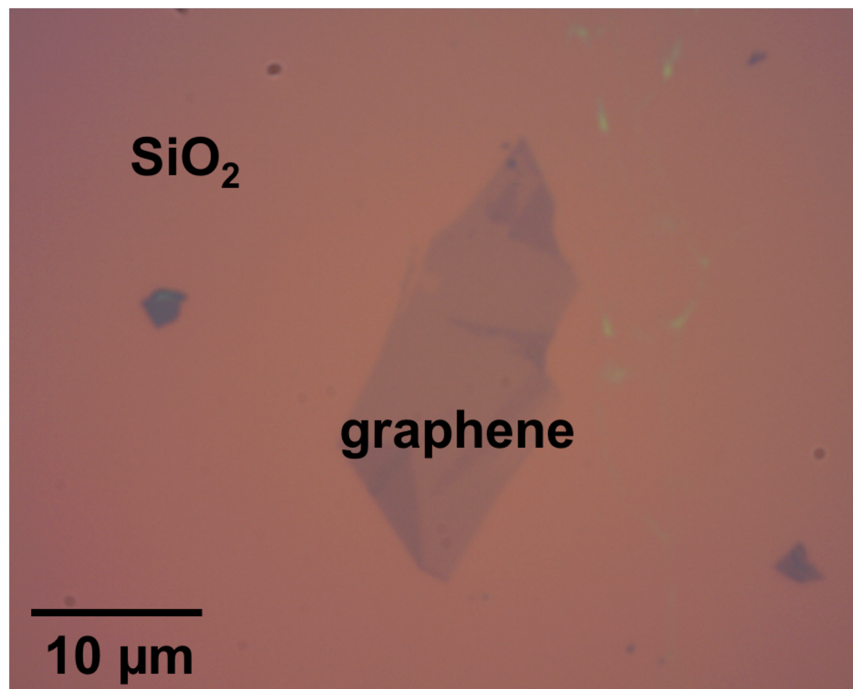

Figure 3-2 Optical micrograph of a few-layer graphene flake on 300-nm SiO_2 substrate.

3.2 Chemical vapor deposition (CVD) growth of graphene

Graphene isolated from bulk HOPG described in the previous section is typically single-grain, has excellent electronic properties and proved to be promising material for future low-dimensional field-effect transistors (FET). However, the randomness of the

mechanical exfoliation process makes the graphene flakes obtained in this way suitable only for small-scale experimental work. For technological applications, high quality graphene that can be produced in large scale is needed. One of the promising ways to mass-produce graphene is by CVD growth of graphene on metal substrates. Ni and Cu are among the most popular metals for graphene growth. Growths on Ni substrates result in various numbers of graphene layers,[74,190] while growths on Cu substrates produce mostly single-layer graphene with small regions of bi-layer and few-layer graphene.[73] This is due to the low solubility of carbon in Cu that results in the self-limiting behavior of the growth once the first layer of graphene covers the Cu surface. For the reason that the CVD growth of graphene on Cu substrates is highly controllable and low-cost, it is seen to be promising for future applications. It is also the substrate of choice for graphene growth in our laboratory.

CVD growth of graphene is done in a high-temperature environment with well controlled pressure. Figure 3-3 shows the schematic of a typical CVD system used for graphene synthesis which consists of the required gas sources (Ar, H_2, and CH_4), mass flow controller (MFC), furnace as heat source and insulation, quartz tube where the growth takes place, pressure regulator, vacuum pump, isolation valve, and vacuum gauge. CVD graphene in our lab is grown using a process that can be summarized as follows:

1) Since the quartz tube is pumped down after each run to maintain the purity inside the tube, it needs to be vented with Ar before each run. This is done by flowing in 500 sccm of Ar until the pressure inside the tube reaches ambient pressure, after which the Ar flow can be stopped.

2) A metal substrate, in our case Cu foil, is loaded into the quartz tube.
3) After the isolation valve between the tube and vacuum pump is opened, the pump is turned on to evacuate the quartz tube.
4) The tube is filled with H_2 at 21 sccm while the pressure is maintained at 60 mTorr.
5) The furnace power supply is turned on and the temperature is ramped to 1050 ºC.
6) Once the temperature reaches the setpoint (1050 ºC), the condition is maintained for 30 minutes to purge the Cu foil of possible organic contaminants.
7) 0.1 sccm of CH_4 is flowed into the tube while the pressure is maintained at 500 mTorr for 30 minutes. This is where graphene forms on the Cu foil.
8) The furnace power supply is turned off to let the temperature inside the tube to cool down.
9) Once the temperature reaches ~200 ºC, the isolation valve is closed and 500 sccm of Ar is flowed into the tube for venting.
10) The Cu foil is carefully unloaded from the tube after it is vented.
11) Ar flow is terminated and the isolation valve is opened to evacuate the tube before leaving.

Figure 3-4 shows an actual photograph of our graphene CVD system. The Cu foil should now have mainly single layer graphene on its surface. In step 7) when the CH_4 is flown into the tube, it is catalytically decomposed on the Cu surface. The carbon atoms are deposited on the Cu surface while the hydrogen byproducts are purged away by the flowing H_2 gas. Owing to the very low solubility of carbon atoms in Cu, the carbon atom deposition

on the Cu surface automatically stops once the Cu, which acts as the catalyst in this formation, is covered by the first layer graphene, suppressing further formation. Therefore, graphene formation on Cu is believed to be due to surface adsorption of carbon atoms, as opposed to the carbon segregation and precipitation mechanism in Ni.

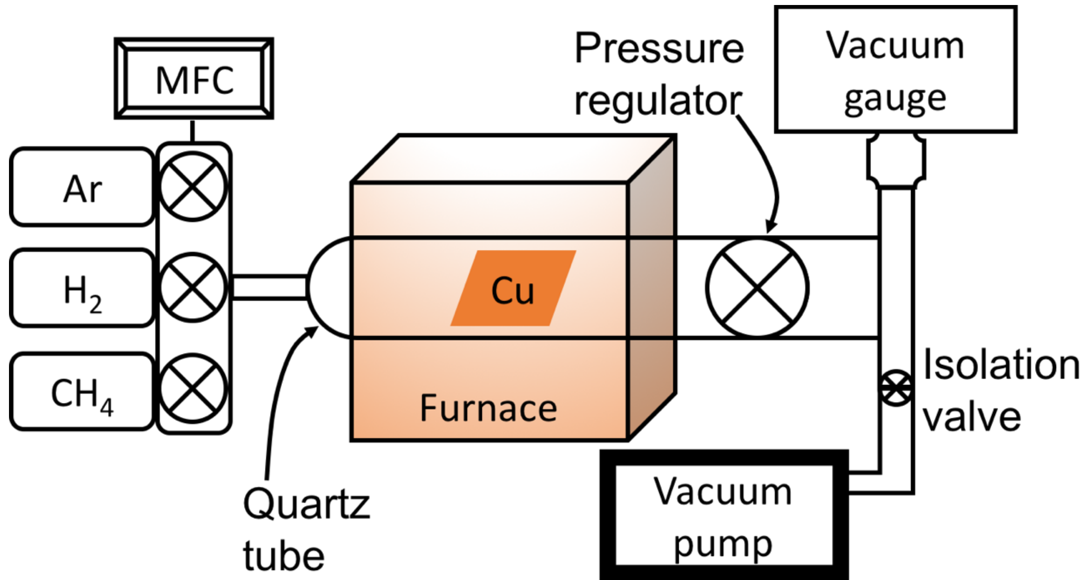

Figure 3-3 Schematic diagram of CVD system for graphene synthesis.

Figure 3-4 CVD system used for growing graphene in Koester Lab.

CVD graphene grown on Cu foil is not readily useful for device applications. It needs to be separated from the Cu foil and transferred onto an appropriate substrate. The transfer process involves several steps as shown in figure 3-5 in the order indicated by the green arrows:

1) The as-grown graphene on Cu foil covers both faces of the foil.
2) One face of the foil is covered with poly (methyl methacrylate) or PMMA resist.
3) Graphene on the uncovered face of the foil is etched using O_2 plasma.
4) Cu foil is floated on an ammonium persulfate solution with the PMMA-covered side facing up to etch the copper.
5) After the copper is completely etched, only graphene/PMMA film remains. The film is scooped out of the ammonium persulfate solution and moved to a deionized water bath to rinse off the residual ammonium persulfate. This step can be repeated to make sure the film is thoroughly rinsed before finally being brought into contact with the desired substrate.
6) The graphene/PMMA on substrate is baked at 80 ºC for about 15 minutes to dry off the deionized water. It is then soaked in acetone overnight for PMMA removal, after which the substrate is rinsed with fresh acetone, isopropanol, and gently blown dry using nitrogen gas. Only graphene should now remain on the substrate.

The copper foil used in our experiment was purchased from Alfa Aesar (Puratronic, 99.999% purity) and was 25 μm thick. The ammonium persulfate solution is prepared by diluting 1 g of ammonium persulfate purchased from Sigma Aldrich (ACS Reagent, ≥ 98%)

in 10 ml of deionized water. Completely etching the copper using this concentration has been found to take a few hours (~5 hours). Figure 3-6 shows an optical micrograph of graphene (dark purple) on SiO_2 (light purple) substrate. The difference in size between CVD grown graphene and mechanically exfoliated graphene is apparent here. For CVD graphene, the size of the graphene that can be grown is only limited by the size of the growth quartz tube or the size of the Cu foil used.

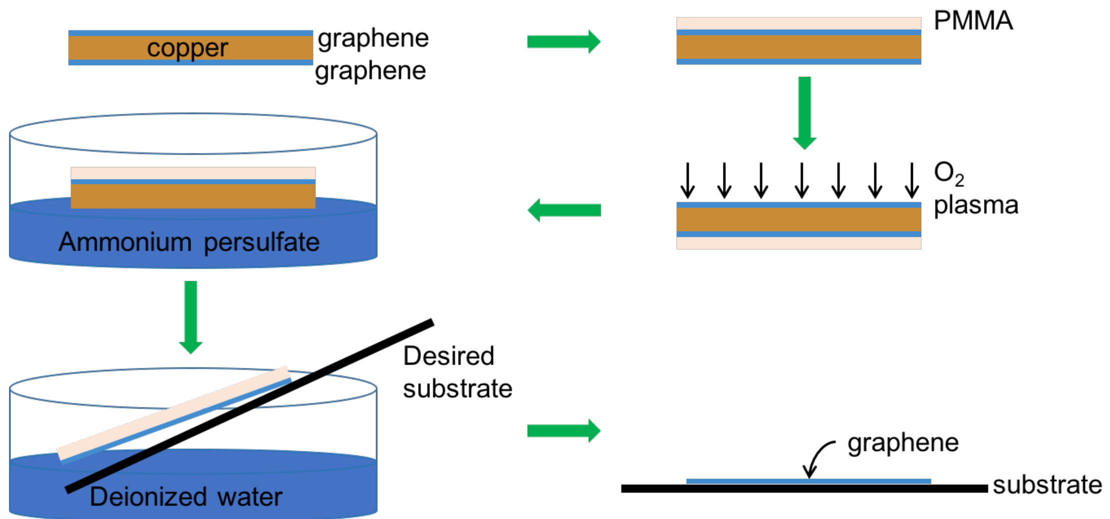

Figure 3-5 Graphene transfer process from Cu foil to a desired substrate ready for further fabrication.

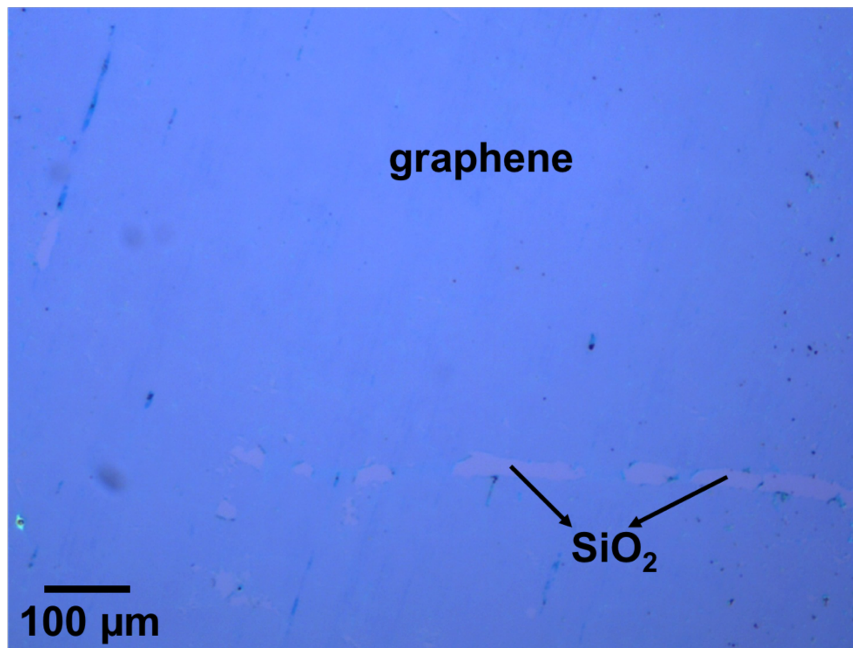

Figure 3-6 Optical micrograph of CVD grown graphene on 300-nm SiO_2 substrate.

Due to the difference in thermal expansion coefficient between graphene and Cu, wrinkles can usually be found in the graphene. It is common for small bilayer or trilayer graphene islands to be found in addition to the large single layer sheet of graphene. We found from our experiments that given the same growth time and H_2 flow rate, the bilayer and trilayer formation is enhanced as the CH_4 flow rate is increased. We also fround that, given the same CH_4 flow rate, the bilayer and trilayer formation is also enhanced as the growth time is increased. This result should not be surprising as the CH_4 gas is the main source of carbon atoms. Even though the graphene formation on Cu is self-limiting, the excess of carbon atoms makes it more likely for surface diffusion of the atoms to happen, causing further surface catalyzed adsorption of the atoms on Cu surface that leads to bilayer and trilayer graphene formation. The bilayer and trilayer regions start to develop from

small nucleation sites and expand over time. It is not entirely clear where the nucleation sites originate from. They could be the defects in the single layer graphene that expose the Cu surface and cause additional layer formation underneath the existing layer. The nucleation sites could also be due to rough Cu surface that provides low energy sites. To test this possibility, we conducted an experiment where we electropolished the Cu foil to smoothen the surface before the growth and found that electropolishing helps remove surface corrugations on the Cu foil and suppress the bilayer and trilayer formation. Luo *et al.*[191] showed a similar result where they could achieve large single layer graphene coverage on a flat, electropolished Cu foil.

Another important aspect in CVD grown graphene concerns the widely adopted transfer method that regularly leaves a significant amount of residual polymer, as shown in figure 3-7a. The PMMA residue left from the transfer is shown by the greenish regions on the graphene on SiO_2/Si substrate. We have found the residue to be persistent and not easily removed using the traditional method by soaking in acetone or NMP. The residue will cause inconsistency in fabricating fine structures of graphene devices and negatively impact the device performance. Several relatively gentle methods involving solvents such as acetic acid, chloroform, and anisole have been adopted at an attempt to remove the resist residue, but no obvious improvement has been observed, which is in disagreement with what has been reported.[95,192] This calls for a more aggressive method for cleaning the surface, for example by using forming gas at high temperature. Figure 3-7b shows the same area on the same sample as figure 3-7a after treatment in forming gas environment (95% Ar, 5% H_2) at 480 ºC for 35 minutes. The resist residue seems to have reduced in thickness,

however it does not seem to have been removed from the graphene surface. In some cases, we have observed graphene being torn in multiple areas of the sample after the forming gas cleaning, suggesting that the strongly attached PMMA residue may have taken some of the graphene in the process of being removed. Besides being an aggressive cleaning method, high temperature annealing could also induce thermal stress that can damage graphene's properties and even change its band structure. The resist residue has been found to be less pronounced in a crack-less, continuous graphene sheet compared to a graphene sheet with many holes or cracks where the residue seems to adhere better. Extreme care given during the transfer, in addition to our improved growth that consistently results in continuous graphene sheets, has resulted in cleaner graphene. However, even graphene that is visibly clean may still have very thin residue on its surface and the existing cleaning methods need to be constantly improved. Apart from the cleaning method, the transfer method could also be improved or potentially replaced by other methods, such as the polymer-free transfer method,[193] which has been shown to yield ultra-clean graphene surface as well as enhanced carrier mobility. The absence of polymer to hold the graphene during transfer necessitates a mechanism that can precisely control and minimize graphene surface tension which could make the process more complicated.

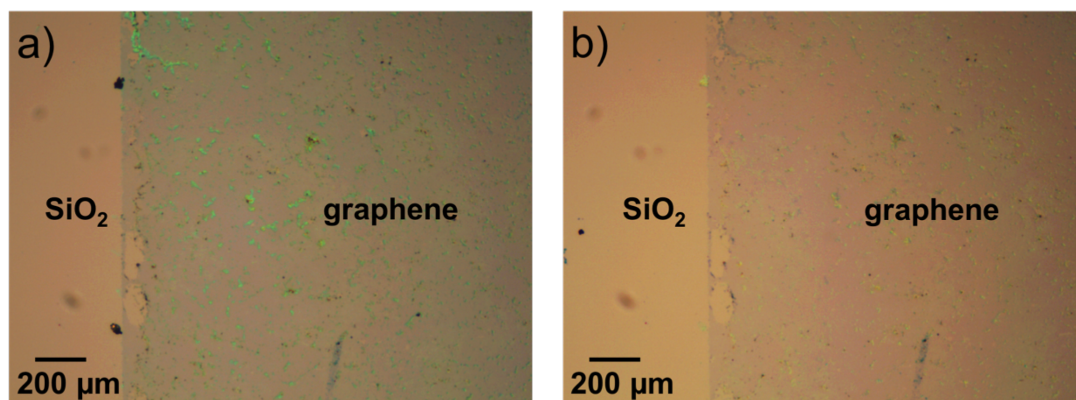

Figure 3-7 Optical image of CVD grown graphene on SiO_2/Si substrate showing PMMA residue. Residue (indicated by green regions) is shown for sample a) without any treatment and b) after high temperature anneal in forming gas.

Surface contaminants have been shown to negatively affect the intrinsic properties of graphene. For example, the reduction in carrier mobility caused by the polymer residue from the transfer not only degrades the charge transport properties of graphene but also harms graphene spintronic device performance. Another surface contaminant that is commonly present in CVD grown graphene is Cu residue that results from incomplete etching of Cu foil during transfer. This Cu residue introduces copper adatoms on graphene. The effect of these adatoms is not necessarily reflected in the reduction of the mobility. Rather, the adatoms can act as spin scattering centers that could reduce the spin relaxation time by orders of magnitude, as discussed in the previous chapter. It is obvious that obtaining pristine graphene surface is immensely challenging and caution is continuously taken in the fabrication of our devices to minimize the adverse effects of the surface contaminants.

3.3 Atomic Force Microscopy (AFM) and Raman spectroscopy for graphene characterization

Upon deposition on a substrate, graphene is usually characterized to determine the number of layers. One method to characterize graphene is by using atomic force microscope (AFM), which is known to accurately image materials down to the nanometer scale. AFM is typically used to extract information such as the layer thickness and roughness. Figure 3-8 shows an AFM image of the mechanically exfoliated graphene in figure 3-2. The height is represented by color mapping in the image with darker colors indicating lower height and brighter colors indicating higher elevation (see the scale on the far right).

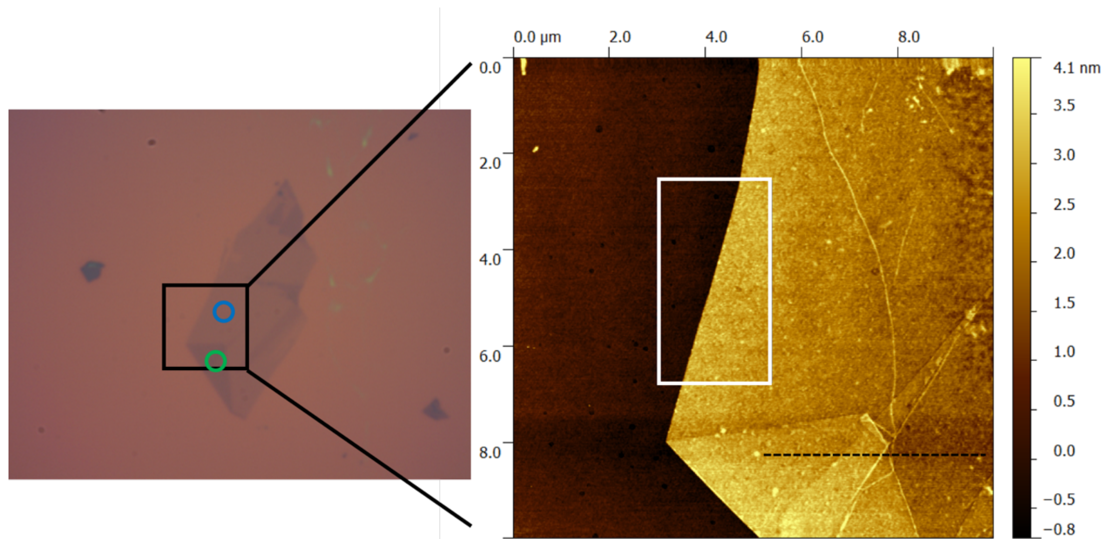

Figure 3-8 Optial and AFM images of few-layer exfoliated graphene. AFM image (right) of the region indicated by the black square in the left image, which is the same graphene sample as in figure 3-2.

The AFM operates by scanning through the area laterally using a sharp tip attached to a flexible cantilever. At each point during the scan, the vertical displacement of the cantilever is recorded by the reflected laser beam off the cantilever surface. The reflected

laser beam changes its angle of inclination depending on the cantilever bending and is eventually read by a position-sensitive detector. The cantilever bending is then translated into a height number at each scan point. At the end of the scan, a 2D image is produced that also has the surface topography information, meaning that basically a 3D image is generated. To acquire the thickness of the graphene, a 1D statistical function tool in the Gwyddion software (this is the software used to process AFM images) is used to calculate the height distribution in a specified area. The measurement of the area denoted by the white rectangle in the right image of figure 3-8 yields a height distribution profile as shown by figure 3-9a. The height distribution plot shows two distinct peaks, which can be attributed to the substrate and the graphene itself. The difference in the height is measured to be ~2.9 nm, which corresponds to about ~8 layers of graphene if a thickness of 3.5 – 4 Å is assumed for each layer. A 1D height profile can also be extracted as shown in figure 3-9b, which is produced by measuring the height along the dashed black line in the right image of figure 3-8. The plot clearly shows the different step heights along the dashed line, which is also visible in the AFM image in figure 3-8. The ~4 Å step most likely indicates one graphene layer while the ~11 Å step could suggest a 3-layer step. Such unambiguous results from AFM measurements have made it a popular tool for characterizing graphene layers.

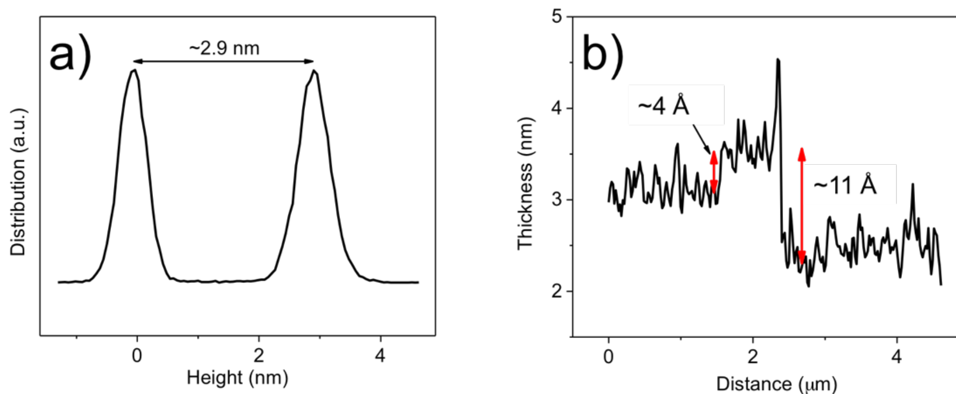

Figure 3-9 Height profiles obtained from AFM analysis. a) Height distribution in the white rectangle in figure 3-8, and b) profile along the dashed black line.

Although the very high resolution of AFM provides unambiguous results of the thickness of graphene and the step height between two graphene layers, it does not yield accurate information of the total number of layers in the graphene. This is due to the gap between the SiO_2 substrate and graphene. Single layer graphene has been found to be around ~1 nm thick[47,92] and this number can vary depending on the SiO_2/graphene contact. For example, there can be trapped moisture in the SiO_2/graphene gap or the graphene can be uniformly curved. Furthermore, AFM requires considerable sample preparation, which makes it a low-throughput tool more suitable for doing fine analysis of a sample. For a more straightforward analysis, Raman spectroscopy is preferred.

Raman spectroscopy relies on the inelastic scattering of incident photon on a material that gives rise to vibrations of chemical bonds within the molecules. No special preparation is usually needed and the measurement itself is nondestructive. Every chemical species has different atoms and bond structures, leading to unique Raman spectra. The carbon-carbon bonds in graphene lead to several peaks shown in figure 3-10a. The G peak (at Raman shift ~1580 cm^{-1}) is a first order peak due to the doubly degenerate zone center

mode. The 2D peak (~2700 cm^{-1}) is the second order peak due to the zone-boundary phonons. The first order peak, the D peak (~1350 cm^{-1}), is not visible in the first order Raman spectra because the Raman fundamental selection rule is not satisfied by these phonons. The D peak takes crystal defects for its activation and is absent in perfect crystalline graphene. The Raman spectrum of single layer graphene is unique and distinct from those with more than one layer. Therefore, Raman spectroscopy is preferable to AFM for the purpose of identifying single layer graphene.

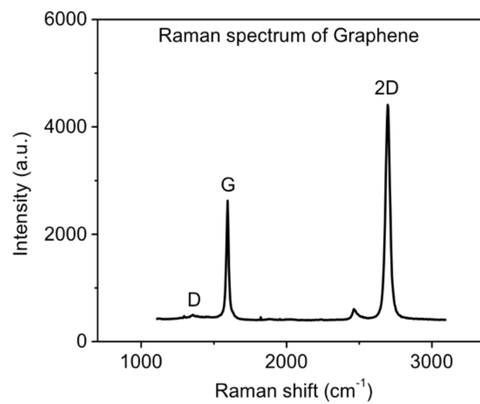

Figure 3-10 Raman spectrum of single-layer graphene.

The Raman spectrum of bilayer graphene is markedly different from single layer graphene. While the 2D peak of single layer graphene can be fitted perfectly by a single Gaussian curve, the 2D peak of bilayer graphene can only be fitted by a sum of four Gaussian curves. Two of the peaks, $2D_{1A}$ and $2D_{2A}$, have higher relative intensities than the other two peaks, $2D_{1B}$ and $2D_{2B}$. An explanation for the four curves in the 2D peak of bilayer graphene was first given by Ferrari *et al.*[194] where they argued that it could not have been due to the splitting of the phonon branches, which they had calculated to produce only < 1.5 cm^{-1} splitting, substantially smaller than the experimentally observed value. They

found that 2D splitting was because of the splitting of the electronic bands caused by the interaction between the graphene planes in bilayer graphene, with the π and π^* bands in single layer graphene splitting into π_1, π_1^*, π_2, and π_2^* bands. As the number of layers increases, the intensities of the $2D_1$ peaks decrease and beyond 5 layers, the spectrum is not distinguishable from that of bulk graphite. The 2D peak shape analysis helps in qualitatively differentiating single layer graphene from bilayer and few-layer graphene, and a more rigorous experimental method in determining the number of layers was proposed by Hao *et al.*[195] They collected a large body of statistics of different layers of graphene and analyzed them in terms of the full width at half maximum (FWHM) of their 2D peaks. Similar analysis was performed on our CVD grown graphene and mechanically exfoliated graphene in figure 3-8, where Raman spectra were taken at two different spots indicated by the blue and green circles. Our analysis show that the FWHM values turn out to be 35.2, 54.9, and 68.1 cm^{-1}, for the CVD grown graphene, and mechanically exfoliated graphene indicated by the blue and green circles, respectively. These values correspond to single layer, three-layer, and five-layer graphene as summarized by Hao *et al*. In addition to the FWHM analysis, an alternative approach by calculating the relative integrated intensities of G/2D was proposed by Graf *et al.*[196] The relative integrated intensities of G/2D for our graphene were found to be 0.31, 0.32, and 0.7, for the same three samples as above. These values correspond to single-layer, single-layer, and five- or six-layer graphene, respectively. The values clearly agree for the single layer and five-layer graphene samples, but disagree for the three-layer graphene. As the mechanically exfoliated graphene is definitely not single-layer, the result obtained for the second sample

using the integrated G/2D intensities was dismissed. We conclude that the region indicated by the blue circle in the exfoliated graphene most likely consists of three graphene layers. The region indicated by the green circle is most likely five or six-layer graphene, confirmed by both FWHM and integrated G/2D intensities analyses.

We have discussed the powerful methods to characterize graphene using both AFM and Raman spectroscopy. The SiO_2/graphene gap was also explained in relation to the reported thickness values for single-layer graphene obtained by AFM that far exceed the atomic diameter of carbon atoms. AFM is frequently used to measure the roughness of the graphene surface, which we found to be especially useful to analyze the roughness of the tunnel barrier deposited on graphene. Raman spectroscopy provides an unambiguous tool to identify single-layer graphene by generating a unique Raman spectrum. The analysis results obtained from graphene grown and exfoliated in our lab reinforce the empirical values that have been reported, with the exception of the discrepancy in the trilayer case compared to the values reported by Graf *et al.* A 2D Raman mapping is also widely used to obtain more detailed information of the graphene surface, for example the defect density. The scanning electron microscopy (SEM), which was not discussed, is particularly useful for imaging graphene nanodevices and can provide information of the chemical composition on the surface, for example Cu adatoms that may be present. All of these different tools are complementary to each other and are each useful in a different way. In the next chapter, we will discuss the fabrication and analysis of graphene field-effect devices to study the experimental charge transport properties of graphene.

CHAPTER 4 CHARGE TRANSPORT PROPERTIES OF GRAPHENE

The most straightforward way to characterize the electronic properties of graphene is probably by making an actual device using graphene. In this chapter, we will review how graphene field effect transistors are fabricated in our lab. The effect of different metals on the quality of Ohmic contact to graphene is discussed and our choice of adhesion layer for metallization in graphene devices is explained. The physical parameters extraction using analytical equations are explained and shown to produce consistent results. Finally, we will discuss the effects of water molecules on the electronic properties of graphene and several methods to reduce the adverse effects.

4.1 Graphene-based field effect transistors (GFET)

In the early days after its first isolation, the charge carrier mobility value in graphene was frequently quoted in papers and regarded as the single most important property of graphene for future post silicon CMOS applications. However, as Schwierz[61] argued, the high carrier mobility may not be the most important property for future FETs based on graphene. This is because in today's technology where the gate length in a transistor is typically of the order of 10 nm, the charge carriers experience a high field while traveling from the source to the drain of a transistor, a situation in which the mobility seems to have less importance. Furthermore, the impressive mobility values reported for graphene were obtained from large-area graphene, which we have seen in chapter one to have no band gap. The absence of a band gap causes the inability of a graphene field-effect

transistor to turn off. This results in constant static leakage power dissipation and makes the idea of using graphene in field-effect transistors less attractive. It is possible to induce a band gap in graphene by creating a quantum confinement effect in narrow ribbons of graphene, typically called graphene nanoribbons (GNR). Although this has been shown to open a band gap in graphene, it also reduced the curvature of the conduction and valence bands, resulting in increased effective mass of the charge carriers and significantly reduced mobility. It has been predicted that the larger the induced band gap is, the lower the mobility, and the mobility in graphene nanoribbons with band gap equal to that of silicon is less than the mobility in silicon as shown by figure 4-1, depriving graphene of its main advantage over silicon. In addition to the reduced mobility, patterning nanoribbons of graphene requires sophisticated techniques which have yet to be perfected. Rough edges in the nanoribbons could cause large fluctuations in the induced band gap and mobility along the nanoribbons that result in unpredictable behavior of these devices.

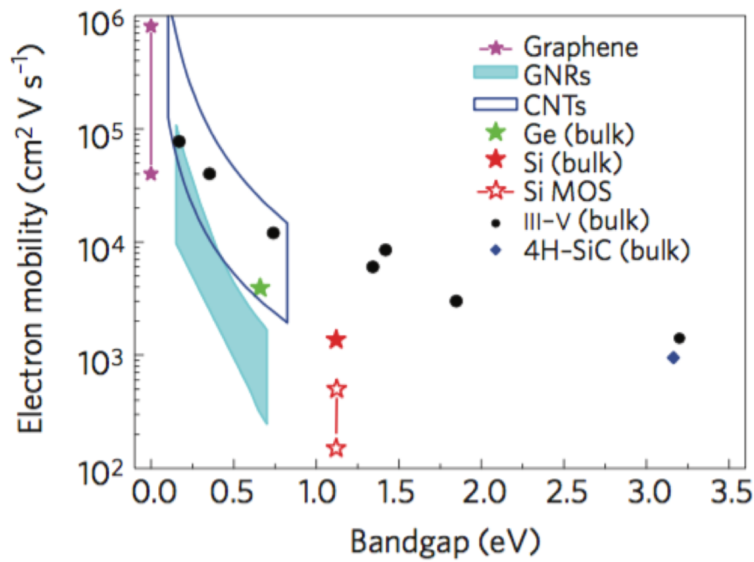

Figure 4-1 Electron mobility as a function of band gap for conventional semiconductors and graphene, graphene nanoribbons (GNRs), and carbon nanotubes (CNTs). Reprinted by permission from Macmillan Publishers Ltd: NATURE NANOTECHNOLOGY (Schwierz [61]), copyright 2010.

As the gate dimension in silicon CMOS gets smaller, short channel effects become very important and can cause severe reliability issue, for example threshold voltage roll-off due to the drain induced barrier lowering (DIBL) effect. It has been predicted by scaling theory[197] that a transistor with thin gate oxide and thin channel will be robust against the short channel effects even at very short gate lengths. Efforts to scale the channel thickness of silicon to sub-2 nm dimension[198] have resulted in rough topology that degraded the carrier mobility. Also, down to this dimension, control of the thickness has been shown to be difficult and thickness fluctuations have been shown to cause an unacceptable level of threshold voltage variations in the devices. Graphene, which is a two-dimensional material, represents the thinnest channel possible and therefore could enable more aggressive scaling for faster, more compact devices. However, the lack of band gap, and thus its inability to turn off, still remains a bottleneck for the realization of high-performance GFETs. RF devices do not necessarily need to turn off, and are therefore an application where large

area graphene with excellent mobility can be utilized. Indeed, a graphene RF device with cut-off frequency f_T exceeding 300 GHz has been reported.[199,200] Due to its extreme mechanical strength, graphene has also found its use in transparent and flexible electronics.[62,190]

We have seen that despite possessing superior electronic properties, i.e. high carrier mobility and minimum thickness which makes it robust against short channel effects, the prospect of putting these properties to use in FETs to compete with Si CMOS remains dubious. Inducing a band gap by patterning graphene nanoribbons has been shown to substantially degrade the mobility. Clearly, GFETs the way they are now are an unrealistic choice for logic applications. But it should be pointed out that at this point graphene FET research can still be considered to be in a relatively early stage and a lot more remains to be done. Nevertheless, graphene has found its use in many more applications. The focus of our work reported in this chapter shall not be on proving the excellent charge transport properties of graphene for superior post-Si CMOS, but rather on studying them. The large area graphene FET is a useful tool for studying the charge transport properties in graphene. We will discuss how these devices are generally fabricated and measured. The effect of metal contacts on graphene as well as the control of its carrier concentration will be discussed. These are some of the pieces in the bigger picture of continuous improvement of graphene devices, and particularly important for us, graphene-based spintronic devices.

4.1.1 Device fabrication

The graphene FETs in our lab are fabricated on Si substrates from a 4-inch Si wafer. The Si wafer is first cleaned following RCA cleaning procedure to remove any native oxide

and organic contaminants on the wafer. The wafer is then loaded into a furnace to thermally grow 300 nm SiO_2 using either the dry oxidation (O_2-based) or wet oxidation (H_2O-based) process. After the growth, the Si wafer is cut into small pieces of substrate (e.g. 1 cm × 1 cm) either by hand using a diamond scribe or a wafer saw for more precision. The substrates are soaked in an acetone-filled beaker placed in an ultrasonic bath to clean off dust that may have landed on the substrates during cutting, rinsed with isopropanol, and blown dry using nitrogen. Graphene is then transferred onto a substrate either by mechanical exfoliation or transfer of CVD grown graphene, both of which were explained in detail in the previous chapter. At this point, we have graphene with an irregular shape sitting on the SiO_2/Si substrate (figure 4-2a). To simplify the device analysis later on, we pattern the graphene into strips with well-defined geometry. This is done by photolithography followed by etching in oxygen plasma. Now that the graphene has a well-defined shape, another step of photolithography is performed to create photoresist patterns for the Ohmic contact formation on graphene. The metals for the Ohmic contact are then deposited by electron beam (e-beam) evaporation of metal sources in high vacuum. Since the surface of graphene is inert, adhesion of some metals on graphene is usually poor. Adhesion layers such as Ti or Cr are first deposited before putting down a thick layer of contact metal, such as Au. The metal deposition is followed by metal lift-off leaving only metal contacts with pre-designed shapes in designated locations. Figure 4-2b shows the top view schematic of a finished device. The cross-section of the device and the substrate stack is shown in figure 4-2c. The purpose of depositing multiple contacts will be discussed

further in the next section. For detailed steps of the fabrication, the reader is referred to Appendix (Nonmagnetic (NM) contacts).

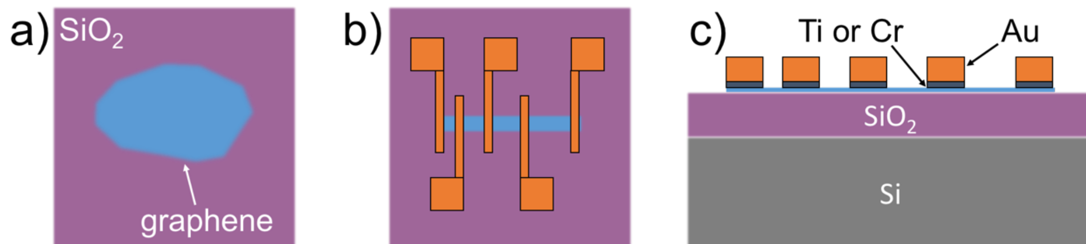

Figure 4-2 Graphene FET schematics. a) Top-view schematic of graphene on SiO_2/Si substrate before any patterning. b) Top-view schematic of the finished graphene FET. c) Cross-section view of the device showing the graphene FET and SiO_2/Si stack.

4.1.2 Ohmic contacts to graphene

The ability to make good Ohmic contact to graphene is crucial for achieving high-performance GFETs. The contact resistance (R_C) values (a measure of the contact quality between graphene and metal) that have been reported vary widely and are in most cases considerably larger than that of metal contact to silicon. The quality of the metal contact on graphene seems to be determined by two factors. The first one is the metal work function difference between graphene and the contact metal. A good contact metal should have a work function close to that of graphene since any difference in the work function can result in charge transfer that causes a dipole layer formation at the graphene/metal interface that serves a potential barrier.[94,200] However, determining the metal of choice is not quite so simple. Song *et al.*[201] performed a detailed analysis of the capacitance-voltage (C-V) characteristics of metal-graphene-oxide-semiconductor (MGOS) structures with different graphene contact areas and found that the work function of graphene underneath a metal was different from the actual work function of graphene. This result should not be

surprising, as graphene in contact with a metal is expected to experience charge transfer and shift in the Fermi level, as predicted by density functional theory calculation.[202] The key result from their experiments was that the work function of graphene in contact with metal depends on the contact metal, meaning that it is either pinned to the metal work function, e.g. when Ni or Cr contact is used, or has a work function that does not depend on the contact metal, which is shown by the similar work function value for both Pd and Au. The work function was suggested to be dependent on the interaction strength between the graphene and the metal, not only the work function difference. Interestingly, the experiments performed by Robinson *et al.*[93] provide a different take on the issue. They found that in real devices, how the graphene is processed probably has stronger influence on the contact resistance. They treated their graphene with gentle oxygen plasma and heat treatment before depositing the contact metals and obtained contact resistance reduction of more than three orders of magnitude. More importantly, the low contact resistance values were found to be independent of the metal-graphene work function difference. The graphene was indeed found to be defective after the treatment, however the treatment probably removed contaminants on graphene that may have otherwise hindered good contact formation.

The second factor that strongly affects the contact resistance in GFETs is the wettability of the metal on graphene due to intermolecular interaction that generates different attraction and repulsion forces between graphene and the metal. Metal delamination due to poor adhesion is often observed in GFETs. Metals with preferable work function difference with graphene may occasionally form contact with graphene with

low resistance. However, they may not necessarily have good wettability on graphene and the resulting devices from such poor contact may not be robust enough to be subjected to further processing, limiting the device process volatility. Furthermore, the quality of different contacts may vary greatly, causing reliability issues and offsetting the low contact resistance advantage. We studied the contact to graphene by using two metals, Ti and Cr, that are frequently used as adhesive layer between Si and metals. They are also routinely used as adhesion layer metals for GFETs.

The quality of the Ti and Cr as the adhesion layer for Ohmic contact in GFETs was studied as follows. We fabricated two different samples in parallel using the exact same conditions as explained in the previous section, except for the final metal deposition. Ti/Au was deposited on the first sample while Cr/Au was deposited on the second sample. The output characteristics of the GFETs on both samples were measured. The current in GFET (I_D) due to applied voltage between the source and drain (V_{DS}) flows through the metal/graphene interface at the drain with resistance of R_C, along the channel with resistance equal to the graphene channel resistance R_G, and then through the second metal/graphene interface at the source with resistance R_C, as shown in figure 4-3a. The resistances of the metal probes and connections were much smaller then the device resistance and therefore negligible. The length of the graphene channel is denoted by L, which is also equal to the distance between the source and the drain, while the width of the channel is W, as shown in figure 4-3b.

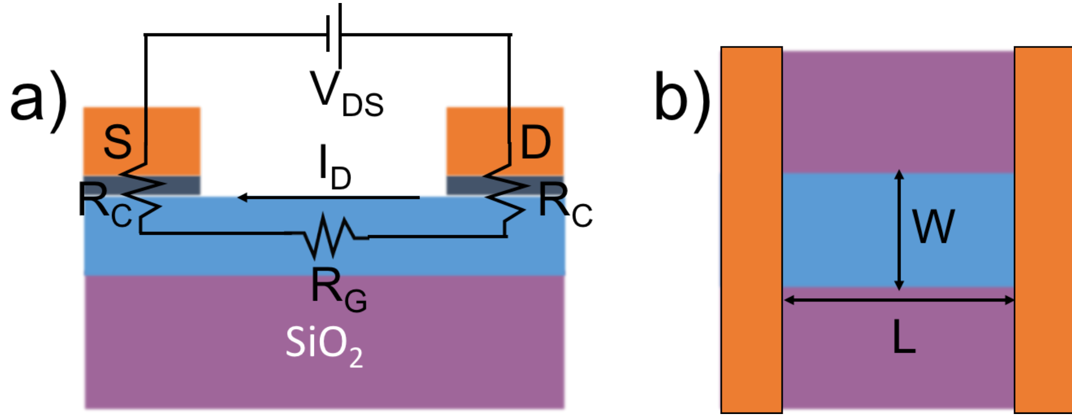

Figure 4-3 Graphene FET resistances and geometry. a) Cross-section view of GFET showing the close-loop current circuit with current I_D induced by applied drain-to-source voltage bias V_{DS} and the contact and channel resistances, R_C and R_G. b) Top-view of the GFET indicating the channel length L and width W.

Since the drain-to-source current (I_D) is simply a function of the applied voltage (V_{DS}) and the resistances (R_C and R_G), it can be written as:

$$I_D = \frac{V_{DS}}{R_C + R_G + R_C} = \frac{V_{DS}}{2R_C + R_G} \quad 4.1$$

The graphene channel resistance (R_G) is a function of the graphene's sheet resistivity (ρ) and the channel geometry, which can be expressed as:

$$R_G = \rho \frac{L}{W} \quad 4.2$$

Substituting R_G from equation 4.2 in equation 4.1, we obtain:

$$I_D = \frac{V_{DS}}{2R_C + \rho \frac{L}{W}} \quad 4.3$$

The total resistance of the device is then:

$$R = \frac{V_{DS}}{I_D} = 2R_C + \rho \frac{L}{W} \quad 4.4$$

Equation 4.4 is the reason behind designing the multiple contacts with different spacing on graphene field-effects transistors as shown in figures 4-2b and 4-2c; it equips us with a method to extract the contact resistance value by analyzing the dependence of the

total resistance on the channel length, commonly known as the transfer length measurement (TLM). Figure 4-4 shows the output characteristics of two sets of GFETs for different channel lengths. The first set (figure 4-4a) was fabricated with Ti/Au contacts and the second set (figure 4-4b) had Cr/Au contacts. We should expect from equation 4.3 that the slope of the $I_D - V_{DS}$ curve should be decreasing as the channel length (L) increases. While it is generally the case, it is usually hard to demonstrate in real experiments. The resistance values seem to scatter around the linear slope of the $I_D - V_{DS}$ curves, making accurate analysis difficult. In figure 4-5a, we show a typical resistance (R) vs. channel length (L) plot for a GFET fabricated with Ti/Au contacts. It can be seen from the plot that although R does decrease as L decreases (black squares), the deviation from linear function (red solid line) makes the extrapolation to zero channel length difficult. Figure 4-5b shows a similar plot but for GFETs fabricated with Cr/Au contacts. Here, we can see that R fits nicely to the linear line, indicating consistent contact across all devices in the array. We found that Cr/Au makes better contact to graphene. Furthermore, the contact resistance of the Cr/Au devices is relatively small. The total contact resistance value ($2R_C$) is simply given by the total resistance value extrapolated to zero channel length. R_C is usually normalized to the channel width ($R_C \times W$) with a unit of [Ω µm]. In the case of figure 4-5b, the extracted contact resistance is about 400 Ω µm, similar to the reported values in the literature.[94] For consistency, Cr/Au are the metals used for making Ohmic contact to graphene in our graphene devices.

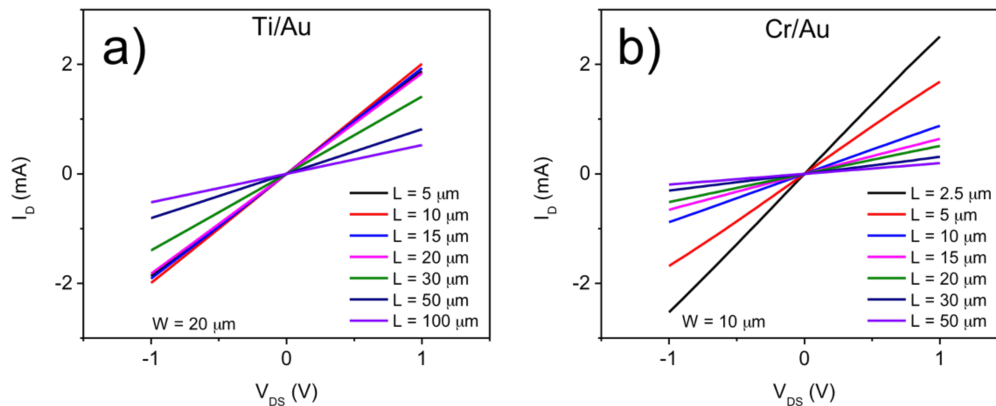

Figure 4-4 Output characteristics of GFETs for different channel lengths. Devices were fabricated with a) Ti/Au and b) Cr/Au contacts.

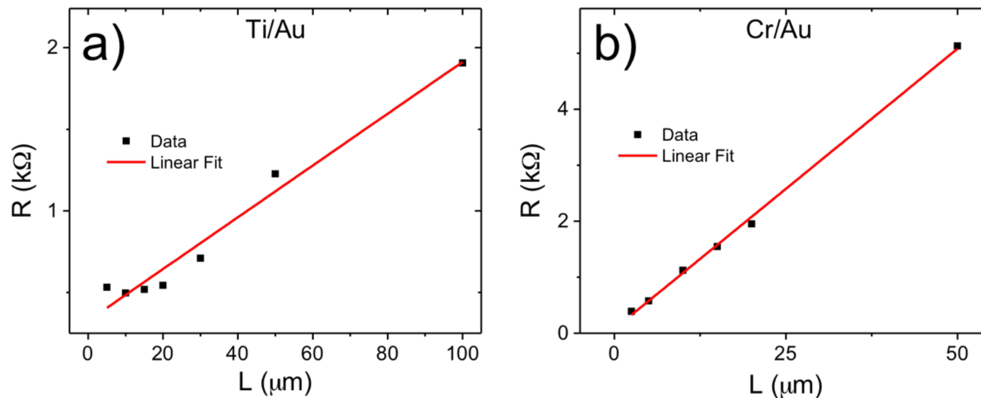

Figure 4-5 Total resistance (R) vs. channel length (L) for GFETs. Devices were fabricated with a) Ti/Au and b) Cr/Au contacts.

We have seen that the contact resistance is also not a straightforward function of the metal-graphene work function difference; the graphene Fermi level may or may not be pinned to the metal work function. We have also seen that it is important to consider not only the low contact resistance when making GFETs but also the consistency of the contacts. Our results suggest that Cr may make an excellent adhesion layer for Ohmic contact to graphene. The fundamental chemistry behind the metal-graphene interface still needs to be studied further. We discussed the relationship between the total resistance of a

GFET and its contact resistance and channel length. In the next section we shall see how the channel resistance can be tuned by applying gate voltage.

4.1.3 Electrostatic gating of GFET

The sheet resistivity (ρ) of graphene, and similarly the conductivity ($\sigma = 1/\rho$), is related to its carrier mobility (μ) and total number of carriers present (n) by:

$$\rho = \frac{1}{\sigma} = \frac{1}{e\,\mu\,n} \qquad 4.5$$

where e is the elementary charge ($\approx 1.602\times10^{-19}$ C. In a perfect graphene sheet free from defects and impurities, the electronic states in graphene should vanish at the Dirac point, as shown by its cone-shaped energy band that consists of two tip-to-tip cones that meet at the Dirac point. However, experimental results in graphene consistently show nonzero conductivity at the Dirac point. This is due to the presence of defects that cause potential fluctuations on the surface of graphene, resulting in equally probable electron-like and hole-like puddles, which give rise to the conductivity at the Dirac point. This residual conductivity together with the sheet conductivity due to the electronic states contribute to the total conductivity of the graphene:

$$\sigma = e\,\mu\,n = e\,\mu\sqrt{n_0^2 + n_G^2} \qquad 4.6$$

where n_0 refers to the density residual charges and n_G the charge density due to the electronic states in graphene. Due to the low density of states in graphene, the carrier population can easily be tuned by applying gate voltage. The gate in a GFET can either be a top-gate or back-gate. Figure 4-6a shows a GFET with a back-gate applied directly to the heavily doped Si substrate with resistivity of 0.001-0.005 Ωcm. The back-gate voltage is

applied across a gate oxide. Given the oxide thickness and dielectric constant, the charge induced in the graphene can be calculated as:

$$e\,n_G = C_{OX}(|V_G - V_{Dirac}|)$$

$$e\,n_G = \frac{\varepsilon_0 \varepsilon_{OX}}{t_{OX}}(|V_G - V_{Dirac}|) \quad 4.7$$

where ε_0 is the permittivity of free space ($\approx 8.854 \times 10^{-14}$ F/cm), ε_{OX} the relative permittivity of the oxide, t_{OX} the oxide thickness, and V_{Dirac} the gate voltage value where the Dirac point is reached. Due to unintentional doping on graphene, V_{Dirac} often does not correspond to $V_G = 0$ in real devices, as shown by the transfer characteristic in figure 4-6b, where the Dirac point corresponds to $V_G = 24$ V (marked by black dot). The applied back-gate voltage effectively moves the Fermi level up and down (as indicated by the dispersion relation curves) such that to the left of the Dirac point, the charge carriers are the holes, while to the right of the Dirac point, it is the electrons that carry the charges.

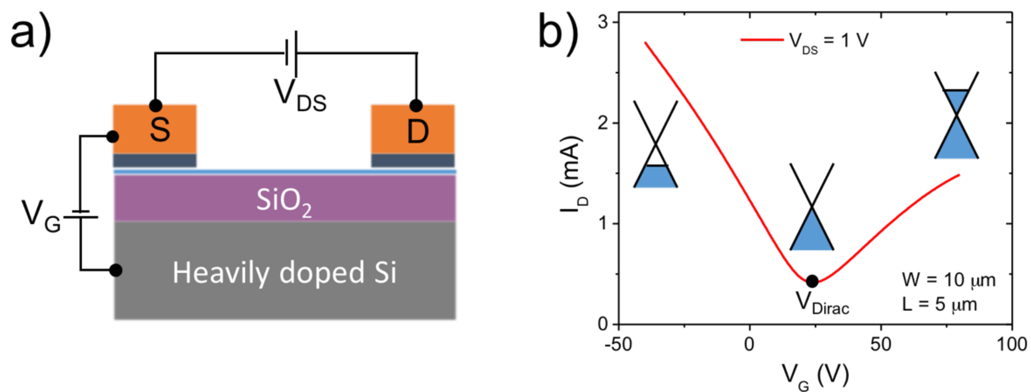

Figure 4-6 Channel conductivity measurement for a GFET. a) Cross-section schematic of a GFET with a back-gate using heavily doped Si. b) Transfer characteristic curve of a back-gated GFET showing ambipolar (hole and electron) conduction in graphene and Dirac point at 24 V.

The transfer characteristic of a GFET contains plenty of information about the device. For example, the Dirac point location tells us whether the graphene is intrinsically

electron-doped or hole-doped with the Dirac point located to the right of $V_G = 0$ V implying hole-doped, and vice versa. The slope of the transfer characteristic reveals how well the graphene can be modulated by applying gate voltage, which in turn reveals the mobility of the graphene. These physical properties can be extracted from the transfer characteristic by analyzing the relationship between the drain current (I_D) and the gate voltage (V_G). Substituting equation 4.5 in equation 4.2, we obtain:

$$R_G = \frac{L}{W\, e\, \mu\, n} \qquad 4.8$$

which relates the graphene channel resistance (R_G) to its carrier concentration (n). Equation 4.8 can be rewritten in terms of equations 4.6 and 4.7 as:

$$R_G = \frac{L}{W\, e\, \mu \sqrt{n_0^2 + n_G^2}}$$

$$R_G = \frac{L}{W\, e\, \mu \sqrt{n_0^2 + \left(\frac{C_{OX}}{e}(V_G - V_{Dirac})\right)^2}} \qquad 4.9$$

Equation 4.9 can be substituted in equation 4.1 to yield the exact equation for the transfer characteristic:

$$I_D = \frac{V_{DS}}{2R_C + \frac{L}{W\, e\, \mu \sqrt{n_0^2 + \left(\frac{C_{OX}}{e}(V_G - V_{Dirac})\right)^2}}} \qquad 4.10$$

The parameters such as the channel geometry ($L = 5\ \mu m$ and $W = 10\ \mu m$) and the oxide capacitance (C_{OX}) are the pre-determined design parameters and therefore known. The drain voltage (V_{DS}) is a measurement condition, which is also known. Equation 4.10 can then be used to fit the transfer characteristic obtained from measurement to extract the

physical parameters such as the contact resistance (R_C), intrinsic carrier concentration (n_0), and effective carrier mobility (μ) by setting them as the free parameters in the fit. It can be seen from figure 4-6b that the transfer characteristic is different to the left and right of the Dirac point. This is commonly seen in GFETs and could be due to the charge density pinning under the contact metal that changes the transport properties at the metal/graphene interface.[91] Due to this asymmetry, the transfer characteristic is analyzed separately for the hole regime (to the left of the Dirac point) and electron regime. Figures 4-7a and 4-7b show the fitted curves for the hole and electron regimes, respectively, of the transfer characteristic shown in figure 4-6b. The extracted intrinsic carrier mobility value is $\sim 5 - 7 \times 10^{11}$ cm^{-2} for both the hole and electron regimes. The extracted values of $R_C \approx 300\ \Omega$ µm and $\mu \approx 2400$ cm^2/Vs are obtained for the hole regime and $R_C \approx 1300\ \Omega$ µm and $\mu \approx 2000$ cm^2/Vs for the electron regime. The higher contact resistance and lower carrier mobility values for the electron regime are consistently observed in our devices and this is consistent with the explanation offered by Song *et al.*[201] that points to work function pinning at the graphene/metal (in our case Cr) interface that could cause a p-n junction formation[91] with the exposed graphene.

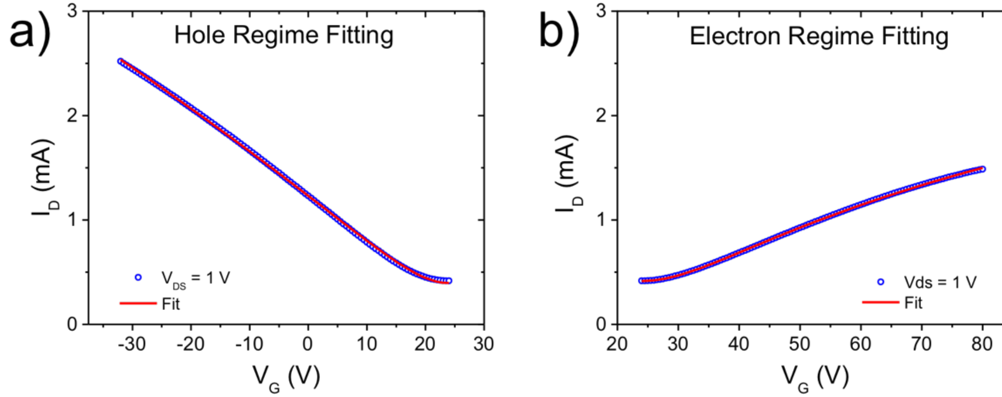

Figure 4-7 GFET parameter extraction by curve fitting. The fitted curves (red solid line) of the transfer characteristic in figure 4-6b were shown for the a) hole regime and b) electron regime. The blue circles indicate the measured values at V_{DS} = 1 V.

We have only considered the case where the electrostatics in the GFET is solely due to the perfect charge transfer between the graphene and the gate. It is very common, however, for the gate oxide to have defects. The oxide defects close to the surface and in close proximity to the graphene channel can potentially act as charge trapping sites. If the trapping sites have small recharging time, the carriers will have enough time to exchange carriers with the graphene, inducing a non-negligible effective capacitance, referred to as the interface trap capacitance (C_{it}), in parallel to the graphene channel given by:

$$C_{it} = \frac{d}{d\mu}\left(-eN_{it}(\mu)\right) \tag{4.11}$$

where μ is the electrochemical potential of the trap states and $N_{it}(\mu)$ is the density of the interface traps at μ. The derivation carried out by Zebrev[203] shows that C_{it} effectively reduces the gate effect on the electrostatics in graphene. In the presence of C_{it}, the carrier density in graphene in equation 4.7 is modified and becomes:

$$en_G = C_{OX}\left(|V_G - V_{Dirac}| + V_0\left(1 - \sqrt{1 + 2\frac{|V_G - V_{Dirac}|}{V_0}}\right)\right) \qquad 4.12$$

where $V_0 = \frac{m^2 \varepsilon_a}{e}$ is defined as the characteristic voltage of the device, $m \equiv 1 + \frac{C_{it}}{C_{OX}}$ the "ideality factor", and $\varepsilon_a = \frac{\pi \hbar^2 v_F^2 C_{OX}}{2e^2}$ the characteristic energy scale (v_F is the Fermi velocity in graphene). Figure 4-8 shows the plots for the carrier density as a function of the gate voltage for 300 nm back gate oxide made of SiO_2. The plots show that as C_{it} increases, the gate modulation of the carrier density gets weaker, which is expected when the interface traps are present and trapping some of carriers. The resulting curves change from linear curve for $C_{it} = 0$ to curves with larger curvatures for larger C_{it}.

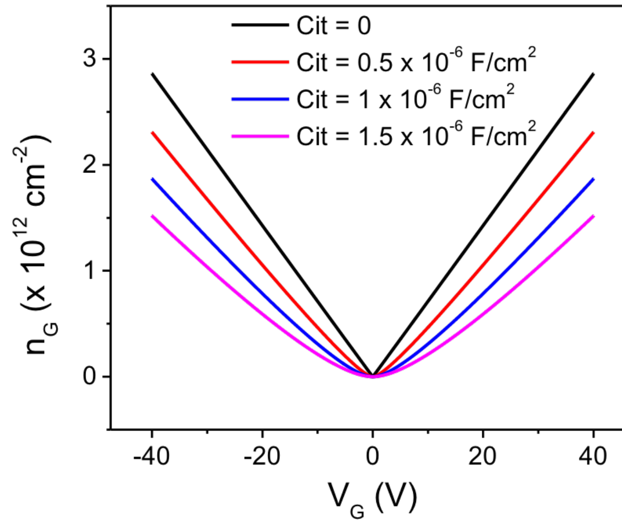

Figure 4-8 Carrier concentration as a function of the gate voltage for different interface trap capacitance values. The gate oxide in the simulated device is 300 nm SiO_2.

The effect of the interface trap capacitance on the transfer characteristic is shown in figure 4-9a. Similar to the carrier density, the transfer characteristic curve also sees an

increase in the curvature when there are interface traps present. The measured values of the drain current (blue circles) cannot be fitted well using the conventional drain current expression given by equation 4.10, as shown by the red solid line and the extracted hole mobility value from figure 4-9a is ~300 cm^2/Vs. Incorporating 4.12 into equation 4.10, which changes the carrier density as a function of the gate voltage, a modified equation is obtained for the transfer characteristic curve:

$$I_D = \frac{V_{DS}}{2R_C + \frac{L}{We\mu\sqrt{n_0^2 + \left(\frac{C_{OX}}{e}\left(|V_G - V_{Dirac}| + V_0\left(1 - \sqrt{1 + 2\frac{|V_G - V_{Dirac}|}{V_0}}\right)\right)\right)^2}}} \qquad 4.13$$

Using this modified equation, a good fit can be obtained for the same transfer characteristic as in figure 4-9a in the presence of interface trap capacitance, as shown by figure 4-9b. The extracted hole mobility value is now ~2600 cm^2/Vs, or about 8 times higher than the value obtained from the conventional equation, and consistent with the mobility value that we regularly obtain from our devices. The density of interface traps in SiO_2 grown by thermal oxidation of Si is generally quite low that its effects on the electrostatics of GFET can often be ignored. However, depending on the growth condition when dealing with other types of gate oxides, for example oxides grown by ALD, defects are sometimes unavoidable and ignoring them in device analysis could substantially underestimate the device properties.

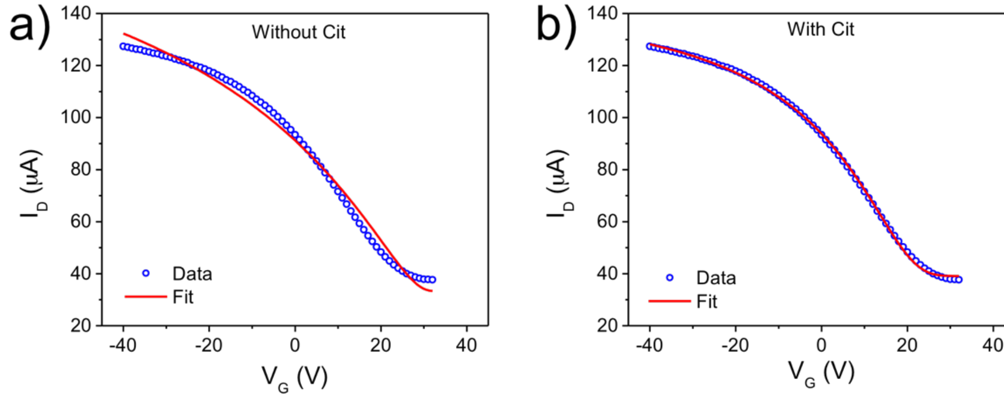

Figure 4-9 GFET curve fitting with and without interface trap capacitance. Measured (blue circles) and fitted curves (red solid line) using a) the conventional equation and b) the modified equation incorporating the interface trap capacitance.

An alternative method for extracting the carrier mobility in graphene is by directly substituting the intrinsic transconductance $\left(g_m = \frac{dI_D}{dV_G}\Big|_{V_{DS}=constant}\right)$ in an analytical equation assuming only gate-induced carriers in the channel:

$$\mu = \frac{Lg_m}{WC_{OX}V_{DS}} \quad 4.14$$

It is this so-called field effect mobility value that is usually reported in the literature. Caution must be taken, however, when quoting this number because it is usually not clear whether the reported values have been obtained by considering the contact resistance effect. g_m, which is basically the slope of the transfer characteristic, changes with V_G and therefore the mobility value extracted using this method may vary depending on where it is extracted with respect to V_G. Because the total resistance of the GFET close to the Dirac point is dominated by the low channel conductivity, the intrinsic transconductance and therefore field effect mobility value in equation 4.14 is usually extracted away from the Dirac point. Far away from the Dirac point, however, the current increase from increased

V_G is limited by the contact resistance. It is consequently tricky to extract the field effect mobility. For comparison, the value obtained by using equation 4.14 at $V_G = 5$ V for the transfer characteristic in figure 4-7a is ~2000 cm^2/Vs, which may have been underestimated compared to the ~2400 cm^2/Vs by analytical fitting to equation 4.10. Additionally, it should be pointed out that Hall bar and van der Pauw structures have frequently been used to investigate the intrinsic properties of graphene.

4.2 Doping control in graphene by surface chemical treatment

It is well-known that H_2O molecules in contact with graphene tend to form a dipole layer generating an electric field that causes the graphene to be hole- or p-type doped,[79–82,204] and together with the doping introduced by the photoresist residue from the processing,[205] graphene is often strongly p-type doped. This could limit our ability to reliably measure the GFET because the Dirac point could be shifted all the way beyond the gate voltage allowable before the gate oxide breaks down. In addition, water molecules also can cause hysteretic behavior indicated by the shift of the charge neutrality point (or Dirac point) with the change in the sweeping direction of the applied gate voltage. The lack of reproducibility caused by the hysteresis makes it impossible to determine the Fermi level, and equivalently the carrier density, accurately when measuring a GFET. This particular behavior has been consistently observed in graphene field-effect transistors (GFETs) fabricated on both exfoliated[87,88] and CVD[82] graphene. Previous work on exfoliated graphene on SiO_2 substrate has shown that the hysteretic behavior could be greatly suppressed, even under ambient conditions, by treating the surface of the substrate using hexamethyldisilazane (HMDS) before the graphene was exfoliated. In some cases, the

hysteresis completely vanished after a vacuum bake at ~200 ºC.[88] A significant increase in the mobility has also been observed by Lafkioti *et al.*[87] on graphene exfoliated on HMDS-treated SiO_2 substrate compared to those on bare SiO_2.

We found that surface pre-treatment of target substrates with HMDS shifts the Dirac-point closer to $V_G = 0$ V, indicating a reduction in p-type doping in graphene on HMDS treated substrates. We attribute this result to reduction of trapped water between the graphene and the substrate. Due to the hydrophobic nature of the HMDS-treated substrate, water molecules cannot easily self-assemble and form a dipole layer on its surface. The starting substrate used in the experiment was heavily-doped n-type Si upon which 280-nm of SiO_2 was grown using thermal oxidation. On top of the SiO_2, a 15-nm layer of aluminum oxide (Al_2O_3) was deposited using ALD. The equivalent oxide thickness (EOT) is therefore ~286 nm. The Al_2O_3 was annealed at high temperature (1050 ºC) for 90 seconds to let it form hardened crystalline structure. The HMDS vapor treatment was carried out as follows. The substrate was then put in a clean and dry petri dish that was left in a larger beaker filled with 1:1 solution of HMDS and acetone no deeper than the height of the small petri dish, as shown in figure 4-10. The beaker was then covered and left for 24 hours. This long exposure time to the HMDS vapor was found to be important to ensure a uniformly hydrophobic substrate was formed on the surface of the substrate.

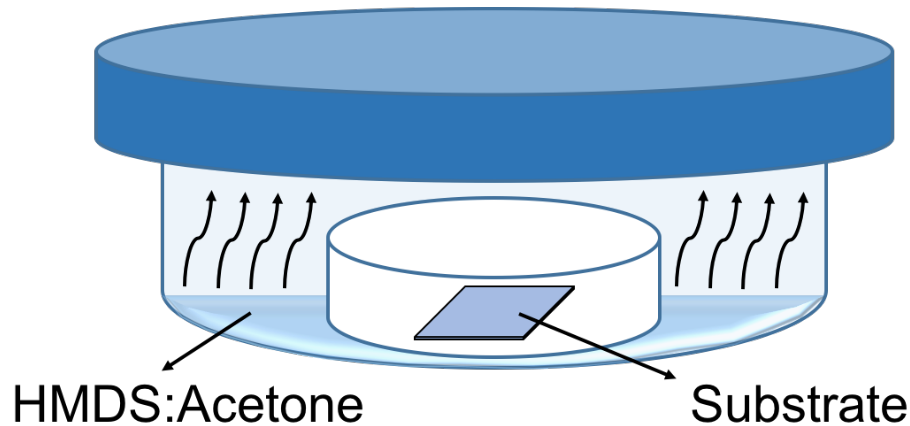

Figure 4-10 The HMDS:acetone vapor treatment environment. The substrate is sitting in a clean and dry petri dish inside the covered beaker slightly filled with the HMDS:acetone solution.

CVD graphene was transferred onto both HMDS-treated and non-HMDS-treated substrates using the method described in chapter 3, followed by device fabrication (Appendix: Nonmagnetic (NM) contacts). The devices were loaded into a vacuum chamber for measurement under controlled environment. Figure 4-11 compares the transfer characteristics of the two types of devices. Figure 4-11a shows the transfer characteristic of the device on the non-HMDS-treated substrate. The Dirac point can be seen to be located beyond $V_G = 100\,V$. Although this was one of the extreme-case examples, the devices from this batch that were fabricated on non-HMDS-treated substrates consistently showed Dirac point between $V_G \approx 60\,V$ to $V_G > 100\,V$. On the other hand, figure 4-11b shows that on the HMDS-treated substrate, the Dirac point can be reached at much smaller gate voltages, typically between 20 V to 40 V. The effect of the HMDS treatment on the gate hysteresis was also studied. We compared 25 GFETs fabricated on both HMDS-treated and non-HMDS treated substrates. The gate voltage was swept from -20 V to +80 V on all devices and the histogram in figure 4-12 shows a clear trend of small hysteresis variation

for the devices on HMDS-treated substrates. The devices on non-HMDS treated substrates, on the contrary, had a large variation in the gate hysteresis.

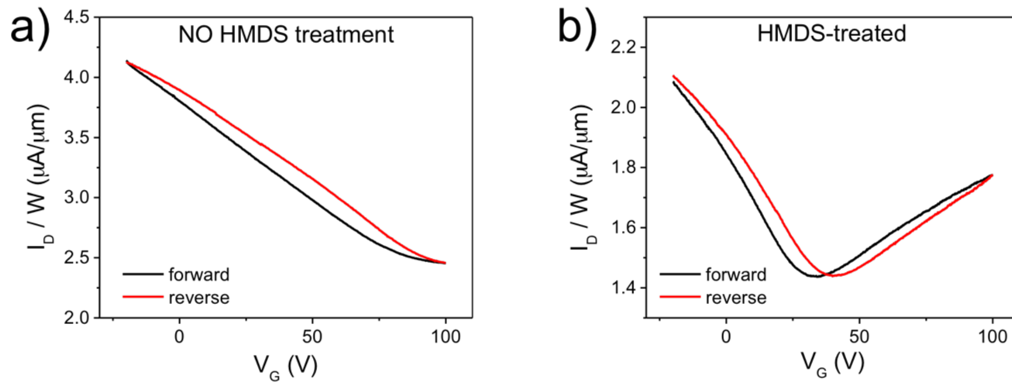

Figure 4-11 Transfer characteristics of GFETs with and without HMDS treatment. Devices were fabricated on a) non-HMDS-treated and b) HMDS-treated substrates.

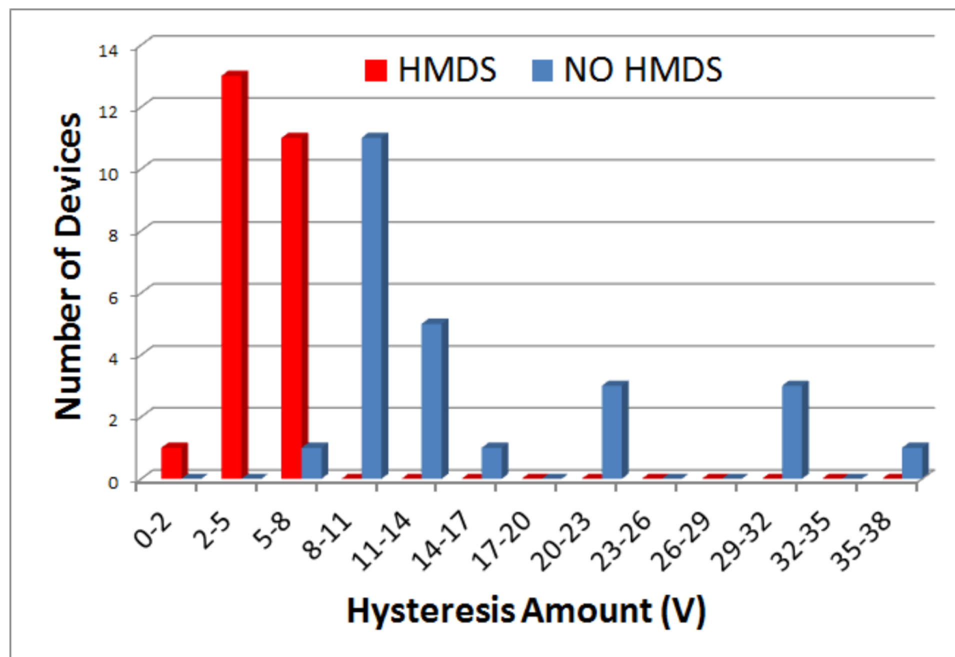

Figure 4-12 Histogram plot of the gate hysteresis for 50 GFETs fabricated on substrates with and without HMDS treatment.

The graphene surface is expected to have few water molecules due to the hydrophobic nature of graphite. However, water molecules can be trapped at defect sites or surface corrugations in the graphene.[204] Some of these molecules could sometimes be

removed either by baking out the sample in vacuum or even just leaving the sample in a continuously pumped vacuum measurement chamber over a long period of time (> 24 hours). On the other hand, water molecules trapped between graphene and the substrate are more difficult to remove and simply baking the sample often times does not solve the problem. The HMDS treatment aims to produce a hydrophobic substrate surface before the graphene is deposited to minimize the amount of water molecules trapped at the graphene/substrate interface. The gate hysteresis in GFETs is a result of charge transfer between the graphene and the water molecules. Since the HMDS treatment makes the substrate hydrophobic, the smaller gate hysteresis on devices on HMDS-treated substrates should not be surprising. In some cases, the hysteresis can also be suppressed by performing the electrical characterization at low temperature where the water molecules are frozen out. It is not clear to us how the hysteresis persists in some devices even at low temperature (~70 K). The HMDS treatment provides a method to minimize the effects of moisture on GFET characteristics and therefore increase the reproducibility. However, we found that especially for CVD-grown graphene where a wet transfer method is utilized to deposit the graphene, the hydrophobic substrate reduces the yield significantly. To maximize the device yield, we have not always adopted this surface treatment method in our experiments.

CHAPTER 5 GRAPHENE-BASED NONLOCAL SPIN VALVES

The nonlocal spin valves are shown to be an important tool to investigate the spin transport properties in graphene. The fabrication method and the tunnel barrier deposition effects on graphene are discussed. The spin injection into graphene is shown by the observed nonlocal resistance signal when the injector and detector ferromagnets switch magnetization directions. The spin transport in graphene is confirmed by the nonlocal Hanle measurement, from which important spin transport parameters can be extracted. The spin relaxation time in both CVD single-layer and exfoliated few-layer graphene was shown to be weakly dependent on the diffusion coefficient at T = 30 K which suggests the presence of spin scattering mechanisms other than the well-known Elliot-Yafet and Dyakonov-Perel mechanisms at this temperature.

5.1 Fabrication of graphene-based nonlocal spin valves

As we have seen from chapter 1, a spin valve is a device that consists of a nonmagnetic layer sandwiched between two ferromagnetic layers. The resistance of a spin valve changes depending on the relative magnetization direction of the two ferromagnetic layers. A nonlocal spin valve, discussed in chapter 2, is a four-terminal spin valve that enables pure spin current detection by isolating the charge current flow. It is widely used to study the spin transport properties such as the spin relaxation time and spin diffusion length in semiconductors, metals, and graphene alike. Here, we briefly describe the

fabrication process of our graphene-based nonlocal spin valves. For details, the reader is referred to Appendix.

The first step of the fabrication is to deposit graphene on an oxide substrate. This can either be done by mechanical exfoliation of HOPG or transfer from CVD graphene grown on a copper foil. If graphene exfoliated from HOPG is used, depending on the shape of the yielded graphene flake, it may or may not be patterned to form a well-defined strip of graphene. For example, in figure 5-1a, the as-exfoliated graphene flake shows an elongated shape ready for device fabrication. The patterning itself takes an additional photolithography step that could introduce contamination on the graphene surface and whenever possible this additional step is avoided. For large-area CVD grown graphene, however, this step cannot be avoided. In this case, the graphene is patterned into rectangles with well defined lengths and widths. The graphene flake shown in figure 5-1a is used for the illustration of the nonlocal spin valve fabrication process. The sample with graphene is spin-coated with Poly methyl methacrylate (PMMA) resist and exposed using electron beam from e-beam lithography tool to write patterns on the resist. The exposed regions written by the e-beam is developed and the resist is dissolved away, opening access to graphene. The sample is then loaded into the e-beam evaporation chamber. The contact metals are deposited on the sample for the Ohmic contacts in high vacuum environment (~10^{-6} Torr or higher). For reasons explained in the previous chapter, Cr/Au (10 nm/80 nm) is chosen. After the metal deposition, the sample is soaked in acetone for metal lift-off. Figure 5-1b shows the device after metal lift-off.

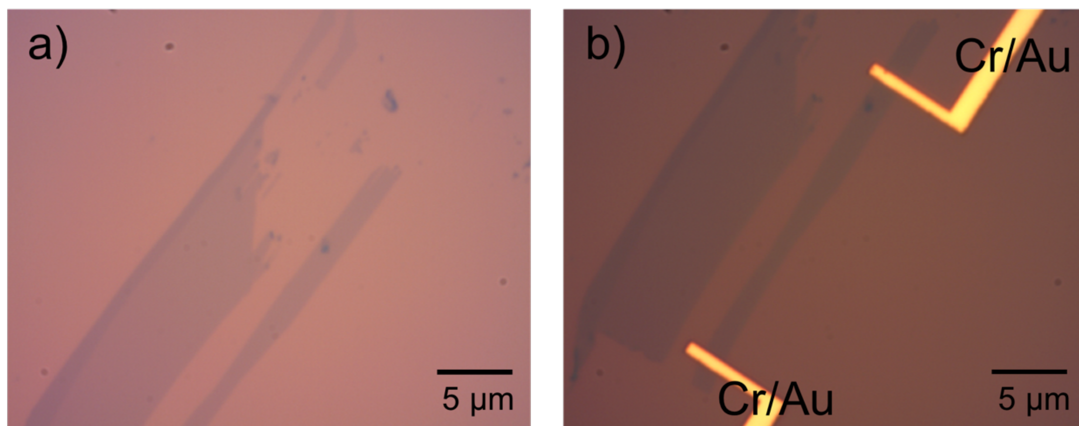

Figure 5-1 Exfoliated graphene flake with nonmagnetic contacts. a) Sample with graphene exfoliated from HOPG on SiO_2 substrate. b) The sample after Cr/Au deposition.

After the Ohmic metal deposition, the sample is spin-coated with methyl methacrylate (MMA) followed by PMMA to produce a double-layer resist stack, which is commonly used when a clean metal lift-off is crucial. The resist stack is exposed by e-beam to write patterns for the ferromagnetic metal contacts (Appendix: Ferromagnetic (FM) contacts). Resist development follows after the e-beam exposure. Due to its higher sensitivity compared to PMMA, the MMA resist is developed faster, which results in an undercut formation. The graphene underneath the exposed resist is now revealed. At this point, the tunnel barrier is deposited by sputtering 6 – 8 Å of Al in a high vacuum sputtering chamber, as illustrated by figure 5-2a. The Al deposition is followed by in-situ oxidation by flowing pure oxygen gas inside the sputtering chamber while keeping the chamber pressure at 80 mTorr (figure 5-2b).

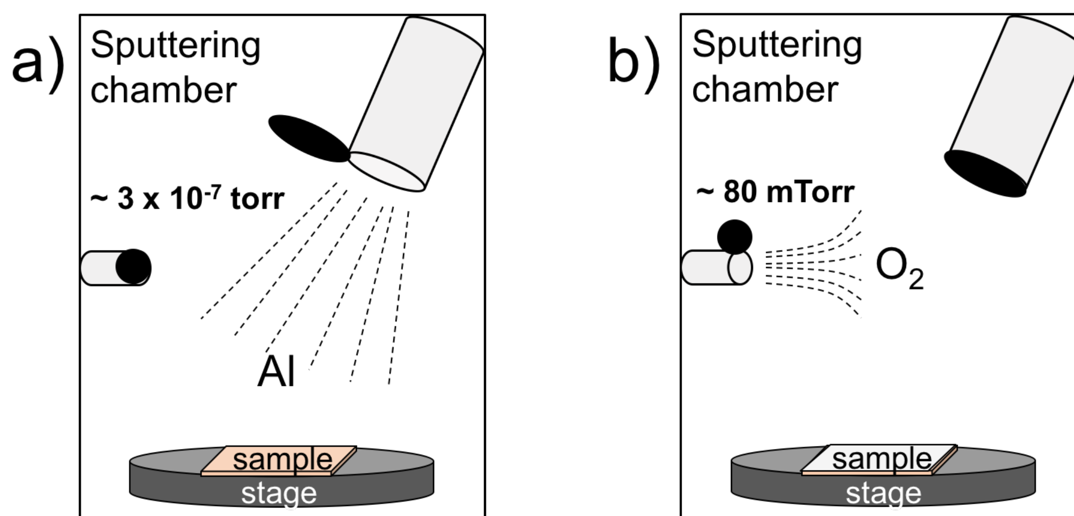

Figure 5-2 Illustration of the Al_2O_3 tunnel barrier deposition process. a) 6-8 Å of Al is sputtered on the sample in a high vacuum sputtering chamber. b) Pure oxygen is flown inside the chamber while the pressure is maintained at 80 mTorr to oxidize the sputtered Al.

Let us now take a step back to see how the Al sputtering affects the graphene quality. A separate experiment on a control sample was done to investigate the effect that Al sputtering has on graphene. Figure 5-3 shows an optical micrograph of an as-exfoliated graphene flake (left) and the Raman spectra (right) taken at the four spots indicated by the colored circles suggest that the flake being studied is a few-layer graphene flake (≥ 3 layers), consistent with our Raman analysis of the same flake in chapter 2. After the tunnel barrier was deposited on the flake using the method described above, the same Raman analysis was performed on the four spots. The Raman spectra of the flake after the tunnel barrier deposition shown in figure 5-4 show an emergence of a small defect-activated D peak. This suggests that the Al atoms sputtered off the Al target may have possessed enough kinetic energy to knock off a few carbon atoms while depositing themselves on the graphene surface. Nevertheless, the observed D peaks were not significant and the graphene was most likely only minimally damaged during the deposition. Furthermore, AFM analysis

performed on the sample showed an rms roughness of ~2 nm and ~3 nm before and after the tunnel barrier deposition, respectively.

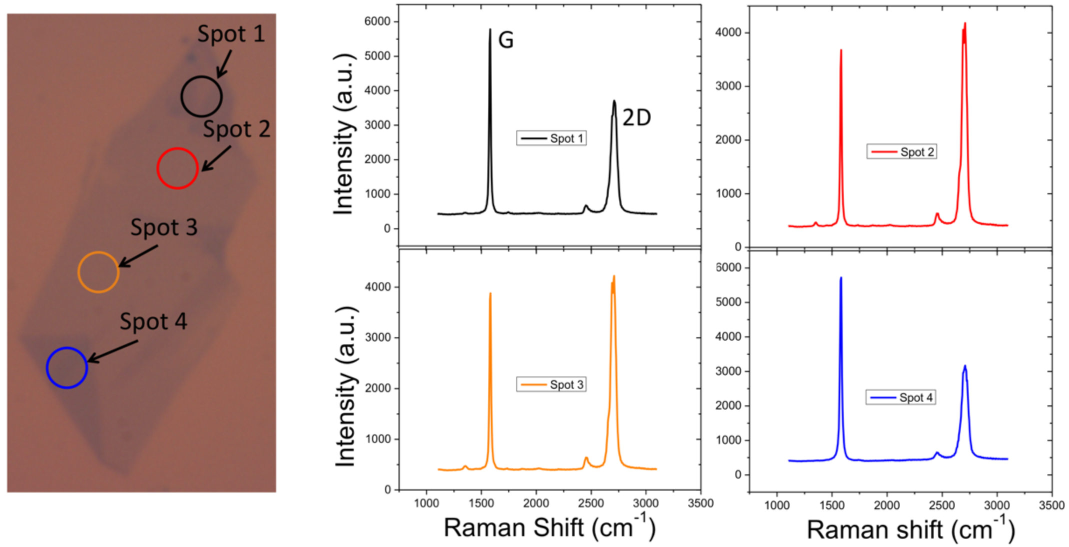

Figure 5-3 Raman spectra of exfoliated few-layer graphene before tunnel barrier deposition. (Left) Optical micrograph of an as-exfoliated few-layer graphene flake. The Raman spectra taken at the four spots indicated in the optical micrograph are shown on the right.

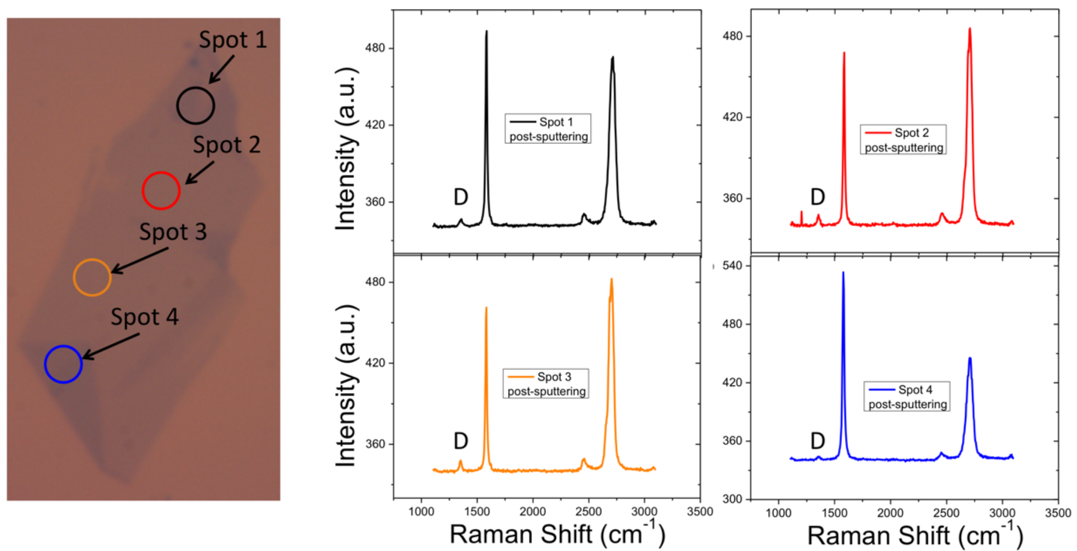

Figure 5-4 Raman spectra of exfoliated few-layer graphene after tunnel barrier deposition. Optical micrograph (left) and Raman spectra (right) of the same few-layer graphene flake as in figure 5-3 after the tunnel barrier deposition. Only small D peaks appear after the sputtering.

The tunnel barrier deposition is immediately succeeded by ferromagnetic metal deposition. This is done by quickly moving the sample from the sputtering chamber to the evaporation chamber. Also under high vacuum condition, 40 nm Co is then evaporated on the sample patterned by the double-layer resist process above. A capping layer of 20 nm Al is finally deposited to prevent rapid oxidation of the Co surface. After metal lift-off, the device should be loaded into a high vacuum storage to prevent device degradation. The finished device is shown in figure 5-5a, and 5-5b with lower magnification. Multiple contacts can be deposited on the nonlocal spin valve, as illustrated in figure 5-5, to study the spin signal dependence on the transport length. The ferromagnetic contacts are patterned to have different widths so that they each have a different coercive field. The Cr/Au contacts at the remote ends of the device are used as the ground for both the current injection and the nonlocal voltage detection. Since they are nonmagnetic, the device analysis is simplified by limiting the magnetization switching only to the center contacts, which are ferromagnetic.

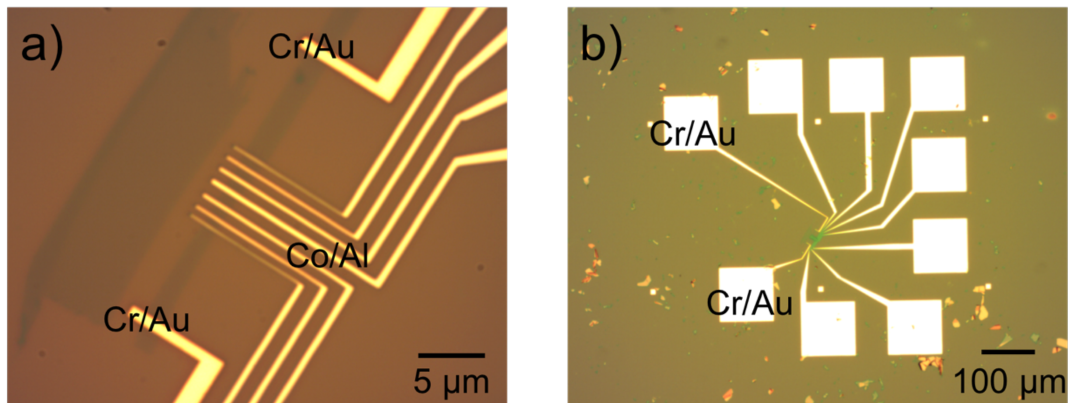

Figure 5-5 Optical images of the finished graphene nonlocal spin valve. a) Higher and b) lower magnification images of the spin valve.

5.2 Equipment set-up for nonlocal resistance measurement

For a quick measurement of the graphene nonlocal spin valves, usually to identify which devices produce spin signals, the cryogenic probe station (Lake Shore CRX-EM-HF) is used. The probe station is equipped with a vacuum storage where the sample sits during the measurement under controlled environment (~10^{-6} Torr pressure) as well as an electromagnet that can generate up to ± 0.6 T of in-plane magnetic field. The nonlocal spin valve is measured as illustrated by figure 5-6 for the nonlocal spin valve consisting of contacts A, B, C, and I. An AC excitation current (I_{AC}) is constantly supplied by the Keithley 6221 current source between contacts B and A. The nonlocal voltage (V_{NL}) is measured between contacts C and I with the detection frequency locked to the excitation current frequency. Keeping I_{AC} constant, V_{NL} is measured while an in-plane external magnetic field (H_{ext}) applied parallel to the easy axis of the ferromagnetic contacts is swept. The presence of a nonlocal spin signal is indicated by the change in V_{NL} at H_{ext} equal to the coercive fields of the ferromagnetic contacts. The nonlocal spin signal is usually normalized to the excitation current to yield a nonlocal resistance $\left(R_{NL} = \frac{\Delta V_{NL}}{I_{AC}}\right)$, where ΔV_{NL} is the change in V_{NL} between parallel and anti-parallel states of the ferromagnetic contacts. For nonlocal Hanle measurement where an out-of-plane magnetic field is required, the devices are measured in a cryostat after they have been wire-bonded to a chip carrier.

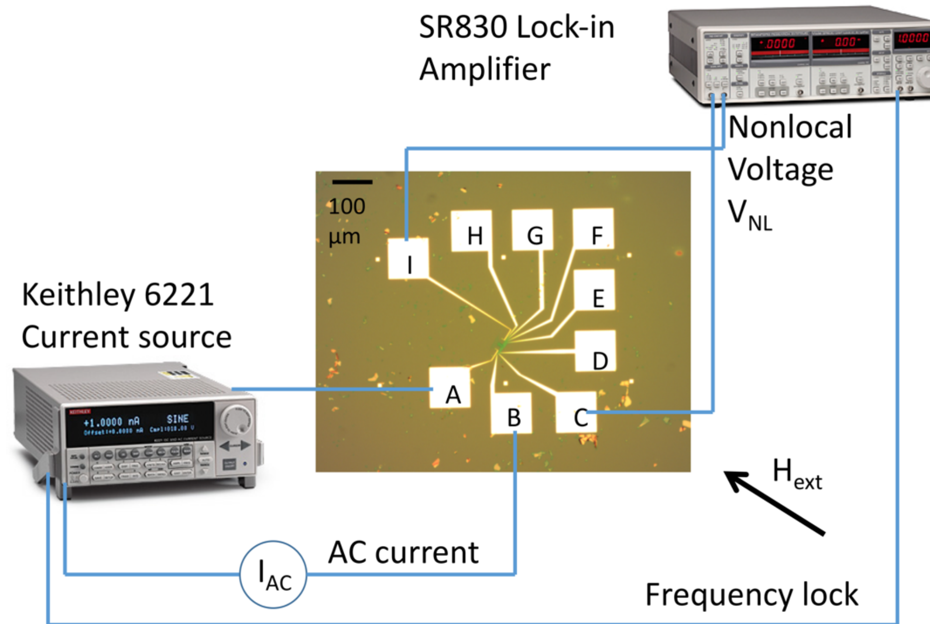

Figure 5-6 Illustration of the equipment connection for performing graphene nonlocal spin valve measurement.

5.3 Graphene nonlocal spin valve measurement

To study the spin transport properties of graphene in our devices, we have adopted both the nonlocal resistance and the nonlocal Hanle measurement methods. These two methods are reviewed in this section in relation to their function in determining the spin transport parameters of graphene.

5.3.1 Nonlocal resistance measurement of graphene nonlocal spin valve

The nonlocal resistance measurement aims to detect the change in the resistance in the detector due to the change of its magnetization direction relative to that of the injector electrode connected to it by a graphene sheet as the spin coherent material. Figure 5-7a shows the nonlocal resistance vs. in-plane magnetic field plot for a typical CVD single-layer graphene taken at T = 90 K. The magnitude of the nonlocal resistance (ΔR_{NL}) is given

by equation 2.21 and the spin signal is usually given in terms of the difference in the nonlocal resistance between the parallel (P) and anti-parallel (AP) states, which is equal to:

$$\Delta R_{NL} = R_{NL(P)} - R_{NL(AP)} = \frac{\alpha^2 R_{sq}\lambda}{W} e^{-L/\lambda} \qquad 5.1$$

where it has been assumed that $P_i = P_d = \alpha$. The graphene channel width (W) and length (L) are design parameters and R_{sq} is the graphene sheet resistivity, which can be determined from charge transport measurement. As a result, Equation 5.1 has two unknown parameters, α and λ, which are the spin injection/detection efficiency and the spin diffusion length. A graphene nonlocal spin valve can be designed to have multiple ferromagnetic contacts with different spacing, such as shown in figure 5-5. It is possible in theory to fit the measured ΔR_{NL} for different spacing (L) and obtain the free parameters α and λ. However, such fitting is difficult to do in practice because ΔR_{NL} is not only affected by L, but also by varying α at different contacts. Ideally, α should be constant for all contacts assuming identical graphene/tunnel barrier/ferromagnet interface quality. However, we have found that it often varies between contacts, which can be attributed to the non-uniform oxide thickness underneath each contact.

In deriving equation 2.21 for the nonlocal resistance, it has been assumed that the interface resistance is dominated by the resistance due to the tunnel barrier, or $R_C \gg R_S$, where R_C is the contact or interface resistance and $R_S = \frac{R_{sq}\lambda}{W}$ is the spin resistance in the graphene. In the case where $R_C \approx R_S$, equation 5.1 cannot accurately predict the magnitude of the nonlocal resistance. This is because in this limit, the injected spins tend to preferentially diffuse or sink back into the ferromagnetic contact and therefore the spins

that are actually diffusing to the detector and responsible for the nonlocal resistance are much fewer than what would be expected, a phenomenon commonly referred to as "spin sinking". Taking into account the spin sinking effect, equation 5.1 can be modified to[133]:

$$\Delta R_{NL} = \frac{\alpha^2 R_{sq}\lambda}{W}\frac{(2R/\lambda)^2 exp(-L/\lambda)}{(1+2R/\lambda)^2 - exp(-2L/\lambda)} \qquad 5.2$$

where $R/\lambda = R_C/R_S$, defined as the spin sinking parameter, is a measure of the number of spins that diffuse into the channel relative to the spins that sink back into the ferromagnetic contact. In the limit $R_C \gg R_S$, equation 5.2 is reduced to equation 5.1, which should be expected for this equation to be true at the high contact resistance limit. The quantity R is calculated for both the injector and detector contacts and in the case where they are not exactly equal to each other, an effective R can be calculated by[206] $1/R \approx \left(\frac{1}{R_i} + \frac{1}{R_d}\right)/2$, where R_i and R_d are the R value at the injector and detector, respectively.

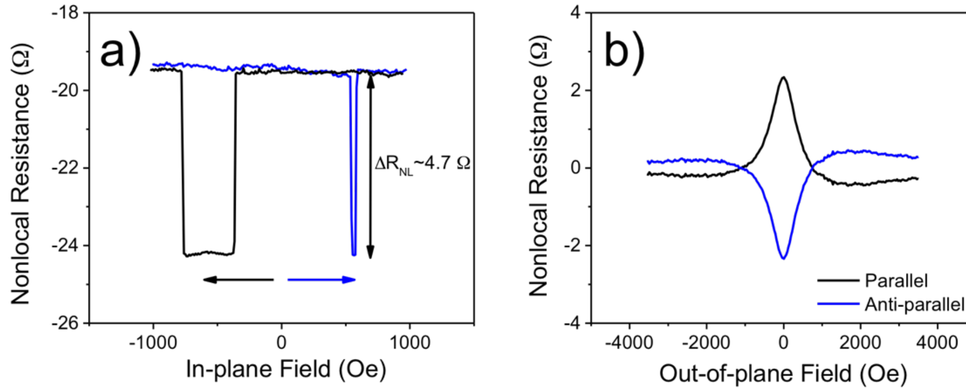

Figure 5-7 Nonlocal resistance and nonlocal Hanle plots of a CVD single-layer graphene spin valve. The nonlocal resistance (a) and nonlocal Hanle (b) data were taken at T = 90 K.

5.3.2 Nonlocal Hanle measurement of graphene nonlocal spin valve

In the presence of out-of-plane magnetic field, the spins injected into graphene precess in-plane around the magnetic field axis at the Larmor frequency. This causes the

spins to arrive at the detector electrode with a distribution of angles and therefore changes the signal depending on the magnetic field strength. Based on equation 2.25, the change in the nonlocal resistance between parallel and anti-parallel states can be written as:

$$\Delta R_{NL} \propto \int_0^\infty \sqrt{\frac{D}{4\pi t}}\, e^{\left(-\frac{L^2}{4Dt}\right)} \cos(\omega_L t)\, e^{\left(-\frac{t}{\tau_S}\right)} dt \qquad 5.3$$

where $\omega_L = \frac{g\mu_B B_\perp}{\hbar}$ is the Larmor precession frequency, which depends on the magnitude of the applied out-of-plane magnetic field ($B_\perp$). It has also been assumed that the contact resistance is much larger than the channel resistance. Equation 5.3 is usually utilized to fit the experimental data to extract the diffusion coefficient (D) and spin relaxation time (τ_S) in graphene. Figure 5-7b shows the nonlocal Hanle plot for the same sample as in figure 5-7a after the background signal had been subtracted. The data were also taken at T = 90 K. In the limit where $R_C \approx R_S$, equation 5.3 can be modified[207,208] to account for the effect of spin sinking:

$$\Delta R_{NL} = \mathrm{Re}\left[\frac{\left(\frac{4\alpha^2}{(1-\alpha^2)^2}\frac{R_{Ci}R_{Cd}}{R_S}\right)\times exp(-L/\lambda_\omega)}{\left(1+\frac{2R_{Ci}}{(1-\alpha^2)R_S}\right)\left(1+\frac{2R_{Cd}}{(1-\alpha^2)R_S}\right)-exp(-2L/\lambda_\omega)}\right] \qquad 5.4$$

where $\lambda_\omega = \sqrt{\frac{D\tau_S}{1+i\omega_L\tau_S}}$ and $R_S = \frac{R_{sq}\lambda_\omega}{W}$ are the complex spin diffusion length and spin resistance of the graphene, respectively. R_{Ci} and R_{Cd} are the contact resistances of the injector and detector. An effective spin injection/detection efficiency has also been assumed here where $P_i = P_d = \alpha$.

5.3.3 Spin transport properties of CVD single-layer graphene

Both the nonlocal resistance and nonlocal Hanle analyses allow a useful interpretation of spin measurement data and provide insight of spin behavior in graphene. CVD single-layer graphene is an interesting case to study due to its importance for large-scale integration of future graphene-based spin devices. Despite extensive studies, the spin transport in single-layer graphene is still not fully understood with different results being reported. Here, we report the results for the special case of CVD single-layer graphene-based nonlocal spin valves fabricated in our lab. Much of the information on the spin behavior of graphene can be deduced from its dependence on the conductivity, which is the reason why the transfer characteristics are a good starting point of the measurement. The solid black line in figure 5-8 shows the channel resistivity vs V_G of the CVD single-layer graphene nonlocal spin valve under investigation taken at T = 90 K with the Dirac point located at $V_G = -5$ V. The blue squares represent the ΔR_{NL} values measured at the corresponding V_G by the nonlocal resistance method described above.

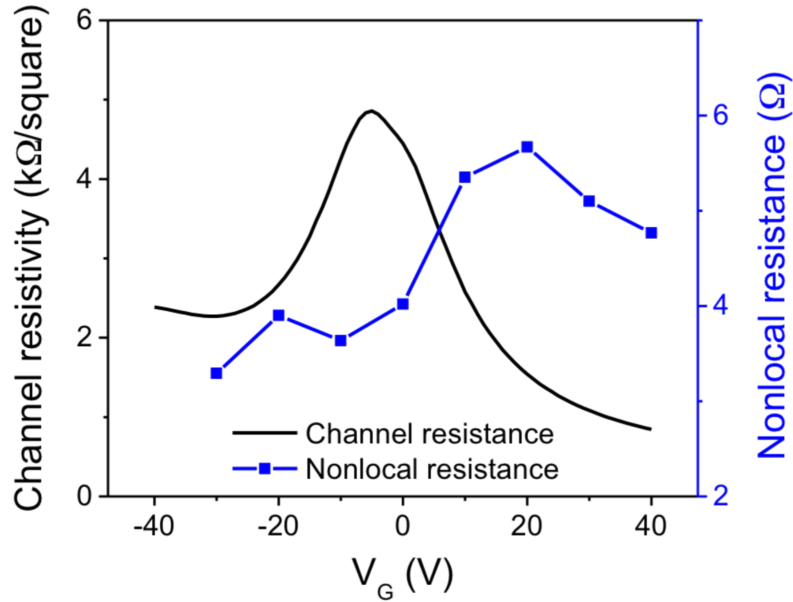

Figure 5-8 Channel resistivity (solid black line) and nonlocal resistance (blue squares) vs. applied gate voltage (V_G) of the CVD single-layer nonlocal spin valve. The device details were discussed in the text above.

The channel resistivity and the nonlocal resistance dependences on V_G in figure 5-8 show no direct correlation. The predicted relationship is shown in figure 5.9.[134] In the transparent regime where $R_C \ll R_S$, equation 5.4 is reduced to an inverse relationship between the nonlocal resistance and the channel resistivity, $\Delta R_{NL} \propto 1/R_{sq}$ (figure 5-9a). When the contact resistance is comparable to the channel resistivity $(R_C \approx R_S)$, the nonlocal resistance exhibits weak dependence on V_G with a dip at the Dirac point (figure 5-9b). In the tunneling regime, $\Delta R_{NL} \propto R_{sq}$ (figure 5-9c). These predictions are made assuming that the change in the spin diffusion length (λ) as a function of V_G is smaller than the change in the channel resistivity (R_{sq}) as a function of V_G. It is unclear at this point if the contacts are of pinhole or tunneling type. The transparent type can be ruled out given the observed magnitude of the nonlocal resistance.

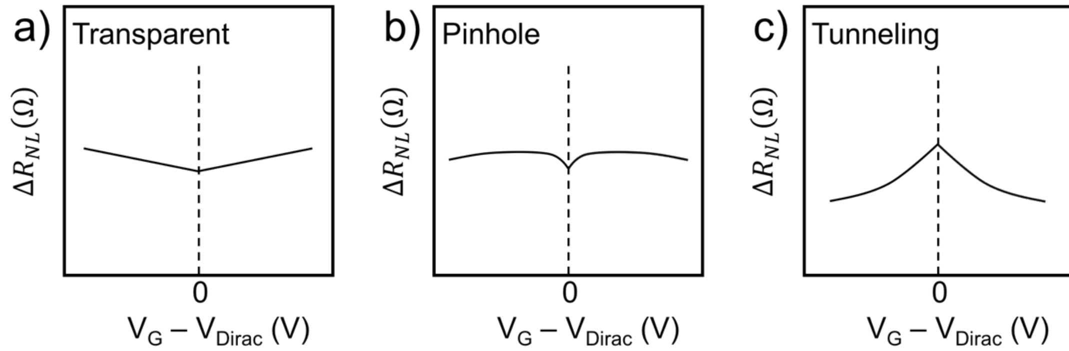

Figure 5-9 Predicted relationship between the nonlocal resistance (ΔR_{NL}) and the applied gate voltage (V_G). Plots shown are for the a) transparent, b) pinhole, and c) tunneling contacts.

As discussed above, the physical parameters of the spin transport in graphene can be obtained by performing the nonlocal Hanle measurement and fitting the data to equations 5.3 and 5.4. Figure 5-10 shows the curve fitting of the same CVD single-layer graphene sample taken at T = 90 K and $V_G = 0$ V to equation 5.4. Fitting the data to equation 5.3 yields similar result, which will be shown later. In the fitting, the spin injection/detection efficiency (α), diffusion coefficient (D), and relaxation time (τ_S) are used as the free parameters.

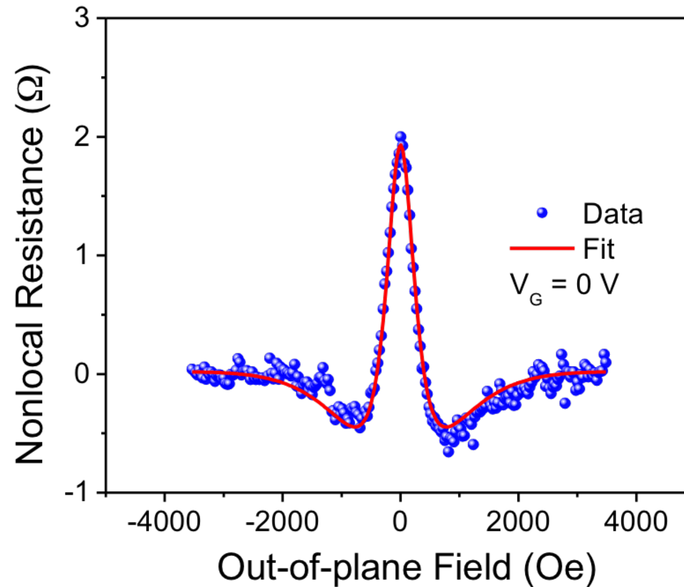

Figure 5-10 Nonlocal Hanle data and the fit result of the CVD single-layer nonlocal spin valve. The experimental data (blue dots) were fit (red line) based on equation 5.4 with the spin parameters being the spin injection/detection efficiency , diffusion coefficient, and spin relaxation time.

The spin injection/detection efficiency can also tell us what category of contacts the device falls into. Based on the results from the fitting, the value ranges from 12% to 21% across different V_G with the average value of ~17%, which means that the contact is most likely of pinhole type, with the efficiency of transparent contacts being ~1%[130] and tunneling contact being ~30%.[134] In figure 5-11, the results from fitting the nonlocal Hanle data to equation 5.3 (figure 5-11a) and 5.4 (figure 5-11b) are compared. The observed dependences of the diffusion coefficient and spin relaxation time on the applied gate voltage are similar in both cases. This means that spin sinking is not one of the dominant effects at play and could suggest that the contacts could be of the tunneling type.

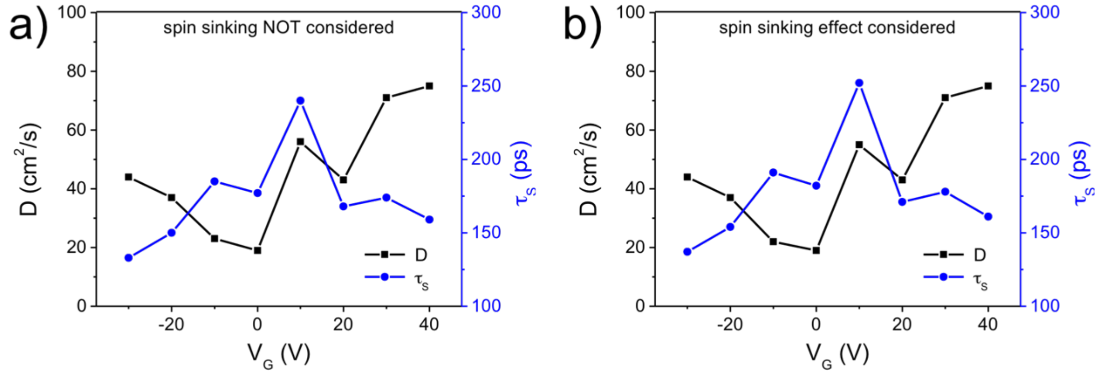

Figure 5-11 Comparison of the diffusion coefficient and spin relaxation time of the CVD single-layer nonlocal spin valve. The results were obtained from a) equation 5.3 and b) equation 5.4. Similar behavior observed in both cases suggests that spin sinking is likely not a dominant effect.

The interesting question that is often asked when talking about the spin properties of graphene is: what is the dominant spin scattering mechanism? Analysis of the nonlocal Hanle results can provide insight into this mechanism. As a reminder, the two main spin relaxation mechanisms in graphene are the Elliot-Yafet (EY) and Dyakonov-Perel (DP) mechanisms. In the EY mechanism, the spins scatter with a finite probability when they interact with phonons and impurities, similar to the momentum scattering. As a result, the spin relaxation time is proportional to the momentum scattering time ($\tau_S \propto \tau_P$). The DP mechanism is due to the spin-orbit field around which the spins precess. This field changes in direction and magnitude at each momentum scattering event, effectively causing the electron spins to experience a random walk (in Larmor phase) and therefore the spin relaxation time is inversely proportional to the momentum scattering time ($\tau_S \propto \tau_P^{-1}$). The momentum relaxation time can be determined by:

$$\tau_P = \frac{h\sigma}{e^2 v_F \sqrt{n g_s g_v \pi}} \qquad 5.5$$

where h is the Planck's constant, $\sigma = 1/R_{sq}$ is the channel conductivity, v_F is the Fermi velocity, n is the carrier concentration, and g_s and g_v are the spin and valley degeneracies of graphene, respectively. It is obvious from equation 5.5 that the momentum relaxation time is proportional to the channel conductivity. The charge diffusion coefficient can be obtained from the Einstein's relation as:

$$D = \frac{\sigma}{e^2 g(E)} \qquad 5.6$$

where $g(E)$ is the density of states at energy E and has a unit of states/eVcm^2. The charge diffusion coefficient is also shown to be proportional to the channel conductivity. The spin diffusion is often assumed to be proportional to the charge diffusion coefficient and therefore also proportional to the channel conductivity. This means that $D \propto \tau_P$ and we can then analyze the relationship between the diffusion coefficient, momentum relaxation time, and spin relaxation time. From figure 5-11b, the plot of τ_S vs. D can be constructed, as shown in figure 5-12. The spin relaxation time changes weakly as a function of the diffusion coefficient. This implies that the spin relaxation is not dominated alone by either the EY mechanism ($\tau_S \propto D$) or the DP mechanism ($\tau_S \propto D^{-1}$). This is consistent with the behavior observed by Han *et al.*[135] where they showed that at high temperatures the spin relaxation time depends very weakly on the diffusion coefficient, even down to 50 K, while at low temperatures (≤ 10 K) the spin relaxation time has a strong linear correlation to the diffusion coefficient, suggesting the EY mechanism as the dominant scattering mechanism. At high enough temperature (> 10 K), various spin scattering mechanisms may be present at the same time and the simple relationship between the spin relaxation time and the momentum scattering time vanishes. Volmer *et al.*,[209] however, observed the DP

mechanism-dominated scattering even at room temperature. Their result is consistent with the theoretical prediction for the spin relaxation mechanism in defect- and impurity-free graphene.[115] These results suggest that the actual spin scattering mechanism in graphene remains unclear and is likely sample-dependent. Some spin scatterers may also be activated at high temperatures. The mechanism is unclear at the moment and requires further investigation.

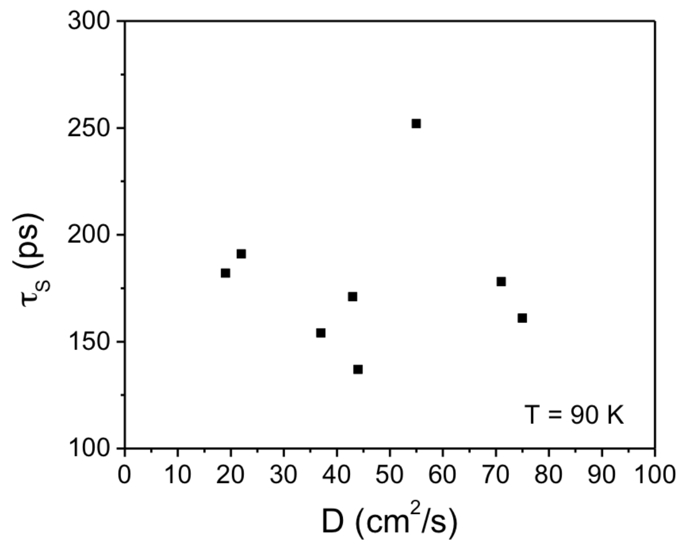

Figure 5-12 Spin relaxation time vs. diffusion coefficient for CVD single-layer graphene nonlocal spin valve. The same device as from figure 5-11 was measured at T = 90 K.

5.3.4 Spin transport properties of mechanically exfoliated few-layer graphene

From our experiments, we found the yield of our CVD single-layer nonlocal spin valves to be low; typically, fewer than 10% of the total fabricated devices showed a spin signal although this number has recently been brought up to ~50% using our improved fabrication process listed in the Appendix. We believe the low yield in these devices is not only due to the imperfect tunnel barrier, but also the deposition of the cobalt that might actually degrade the graphene. Indeed, Canto *et al.*[155] showed that depositing cobalt

directly on graphene degraded the graphene as indicated by the appearance of a large D peak in the Raman spectrum. In an attempt to increase the yield, we fabricated nonlocal spin valves on mechanically exfoliated few-layer graphene flakes. The yield of these devices is much higher (~80%). This could indicate that while the top layer may be damaged during cobalt deposition causing spin polarization reduction, the spin polarization in the bottom layers may be preserved.

The spin transport properties of few-layer graphene are also very interesting. This is because the spin relaxation time in few-layer graphene has actually been found to be a few times longer than that of single-layer graphene and an increasing function of the number of layers.[210] This is due to the screening of the scattering potentials in few-layer graphene. Coupling strength to the substrate is also reduced in few-layer graphene which results in weaker substrate-induced spin scattering and thus longer spin relaxation time. Goto *et al.*[127] have also demonstrated a spin diffusion length of ~8 μm in few-layer graphene. Besides providing screening of scattering potentials due to its larger intrinsic charge carriers, the more conductive few-layer graphene compared to single-layer graphene can also reduce the conductivity mismatch with the ferromagnet. Moreover, our CVD graphene growth results (data not shown) indicate that it is possible to grow up to three-layer, or possibly more, graphene by tuning the growth conditions such as growth time and hydrogen/methane ratio. With the right growth conditions, it may possible, for example, to grow wafer-scale three-layer graphene with large grain size suitable for large-scale applications of few-layer graphene-based spintronic devices.

To study the spin transport properties in few-layer graphene, a similar nonlocal spin valve to the one used in the single-layer graphene was fabricated. Based on the AFM analysis, the few-layer graphene used in the nonlocal spin valve was determined to be a three-layer flake. Similar measurement was also performed at T = 30 K to extract an equivalent set of information. Figure 5-13 shows the channel resistivity (R_{sq}, black squares) and nonlocal resistance (ΔR_{NL}, blue squares) as a function of the applied gate voltage (V_G). The nonlocal resistance shows a minimum at the Dirac point ($V_G = 20\ V$), which indicates that the contact is either transparent or pinhole type. The relatively large nonlocal resistance values of a few Ohms suggest that the contact is more likely of pinhole type, rather than transparent.

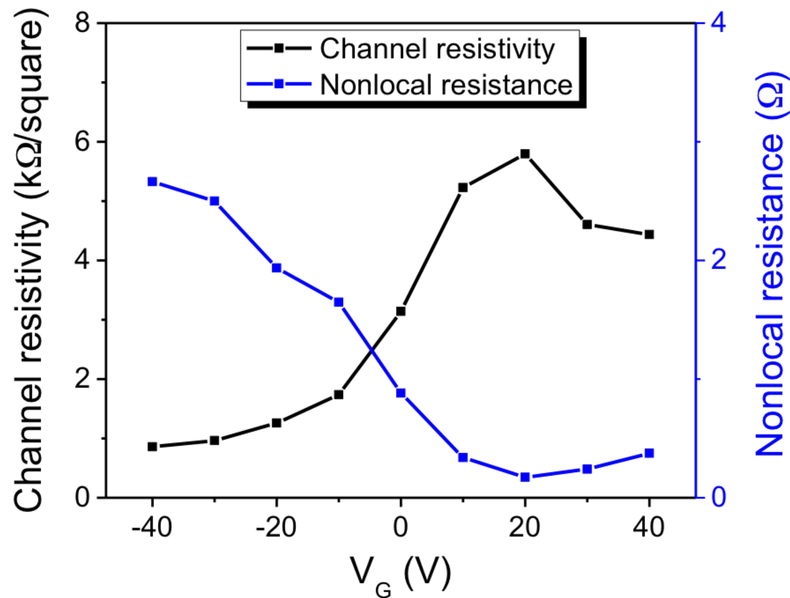

Figure 5-13 Channel resistivity and nonlocal resistance vs. applied gate voltage of the exfoliated few-layer graphene nonlocal spin valve. The inverse relationship between the channel resistivity (black squares) and the nonlocal resistance (blue squares) suggests pinhole type of contact.

The nonlocal Hanle measurement was subsequently performed to extract the spin transport parameters in the three-layer graphene. Figure 5-14a shows the plot for the

extracted values of D and τ_S as a function of V_G. The spin sinking effect was considered for the data analysis, i.e. equation 5.4 was used as opposed to equation 5.3. As expected, D exhibits a minimum at the Dirac point and increases with conductivity or V_G. Once again, no strong correlation between τ_S and V_G is observed. The relationship between the spin relaxation time and the diffusion coefficient is shown in figure 5-14b. Similar to the single-layer case at this temperature (30 K), no strong correlation can be observed here. This also suggests that at this temperature, the spin scattering is neither dominated by the EY mechanism nor by the DP mechanism.

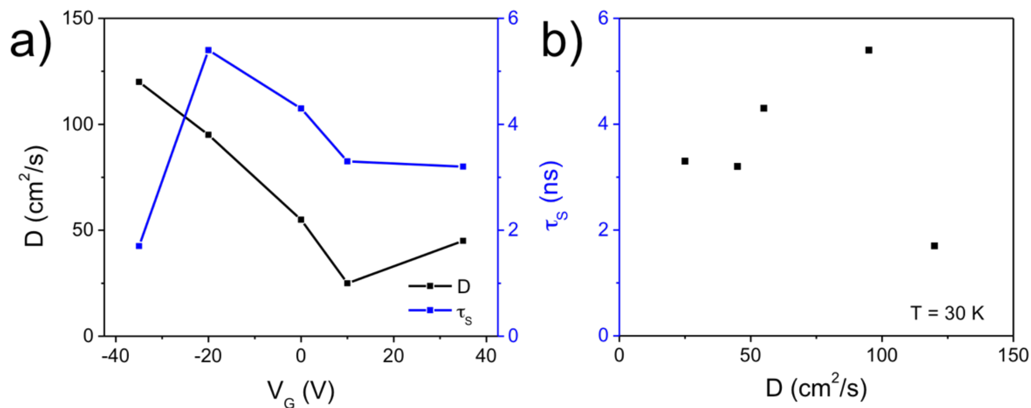

Figure 5-14 Relationship between D and τ_S of the exfoliated few-layer graphene nonlocal spin valve. a) D and τ_S as a function of V_G. b) Weak correlation is observed between τ_S and D.

In summary, the fabrication of graphene nonlocal spin valves was reviewed including the tunnel barrier deposition method and its effect on graphene quality. The nonlocal resistance and nonlocal Hanle measurements and their usefulness for studying the spin transport properties in graphene were discussed. The spin sinking effect may dominate at low contact resistance regime and the appropriate equations must be used in the data analysis in order to obtain accurate results. In both the CVD single-layer and exfoliated three-layer graphene cases, the spin relaxation time exhibits very weak correlation to the

diffusion coefficient at T = 30 K, suggesting that mechanisms other than the EY and DP mechanisms may be dominant in some of our devices. In other devices, as we will see in the next chapter, clear EY mechanism-dominated behavior was observed in the case of CVD single-layer graphene devices.

CHAPTER 6 ELECTRIC FIELD AND DOPING ASYMMETRY EFFECTS ON SPIN TRANSPORT IN GRAPHENE

Different methods to control spin transport in graphene are explored in this chapter. External electric field is shown to alter the spin diffusion length in graphene, which is consistent with theory and earlier experimental work. The double buried-gate structure is proposed to study the spin transport in the presence of doping asymmetry in the graphene channel. The observed effect on the spin signal in our current device is shown to be weak, the origin of which requires further investigation. A possible ASL devices design with incorporated double buried-gates is proposed.

6.1 Asymmetric spin transport in graphene nonlocal spin valve due to applied electric field effect

6.1.1 Electric field effect on spin transport in semiconductors

In studying the spin transport in semiconductors, it is common to assume that the spin polarization obeys the diffusion equation:

$$\nabla^2(\mu_\uparrow - \mu_\downarrow) - \frac{(\mu_\uparrow - \mu_\downarrow)}{\lambda^2} = 0 \qquad 6.1$$

where $\mu_\uparrow$ ($\mu_\downarrow$) is the electrochemical potential of the spin-up (spin-down) electrons and λ is the diffusion length. Equation 6.1 implies that the spin polarization $(\mu_\uparrow - \mu_\downarrow)$ decays away as a function of position from the initial point $(\mu_\uparrow - \mu_\downarrow)|_{x=0}$ with a length scale of λ. This equation is the same as the one used to describe the spin transport in metals and

considers only diffusion of the spins. In metals, any electric field that is present is essentially screened and equation 6.1 can accurately describe the spin transport. This is not the case in semiconductors and the electric field effect on the spin transport may not be negligible. Indeed, Yu and Flatté[211,212] showed that in the presence of an electric field in the direction of the spin transport in nondegenerate semiconductors, the spin polarization of the electrons is governed by the drift-diffusion equation:

$$\nabla^2(n_\uparrow - n_\downarrow) + \frac{e\boldsymbol{E}}{k_B T} \cdot \nabla(n_\uparrow - n_\downarrow) - \frac{(n_\uparrow - n_\downarrow)}{\lambda^2} = 0 \qquad 6.2$$

where $n_\uparrow$ ($n_\downarrow$) is the deviation of the spin-up (spin-down) electron density from its equilibrium value, k_B the Boltzmann constant, T the temperature, and $\boldsymbol{E}$ the electric field. They also derived a more general drift-diffusion equation that applies to both degenerate and nondegenerate semiconductors, where the spin polarization is now given by:

$$\nabla^2(n_\uparrow - n_\downarrow) + \frac{\mu}{D}\boldsymbol{E} \cdot \nabla(n_\uparrow - n_\downarrow) - \frac{(n_\uparrow - n_\downarrow)}{\lambda^2} = 0 \qquad 6.3$$

with μ being the electron mobility and D the diffusion coefficient. Using the Einstein relation for the nondegenerate statistics case, $\frac{\mu}{D} = \frac{e}{k_B T}$, equation 6.3 can be shown to reduce to equation 6.2. The second-order differential equation in equation 6.3 can be solved directly and the general solution for the spin imbalance has the form:

$$n_\uparrow - n_\downarrow = A_1 exp(-x r_1) + A_2 exp(-x r_2) \qquad 6.4$$

where $(r_1 = 1/\lambda_1)$ and $(r_2 = 1/\lambda_2)$ are the roots of the characteristic equation of equation 6.3, i.e. $r^2 + (\mu E/D)r + 1/\lambda^2 = 0$. The exact solutions to equation 6.4 can be obtained by applying the boundary condition that the spin imbalance should decay to zero infinitely

far away from the injection point and setting the electric field to point to the $-x$ direction ($\boldsymbol{E} = -E\hat{x}$), yielding:

$$n_\uparrow - n_\downarrow = (n_\uparrow - n_\downarrow)|_{x=0}\, exp\left(-\frac{x}{\lambda_d}\right), \qquad x > 0 \qquad 6.5a$$

$$n_\uparrow - n_\downarrow = (n_\uparrow - n_\downarrow)|_{x=0}\, exp\left(\frac{x}{\lambda_u}\right), \qquad x < 0 \qquad 6.5b$$

Here, $(n_\uparrow - n_\downarrow)|_{x=0}$ is the continuous spin imbalance injected at the injection point defined at $x = 0$ and the spin imbalance vanishes at $\pm\infty$ due to spin relaxation. λ_d and λ_u are the diffusion lengths of the electron spins traveling downstream and upstream from the electric field, respectively, and can be expressed as:

$$\lambda_d = \left[-\frac{\mu|E|}{2D} + \sqrt{\left(\frac{\mu|E|}{2D}\right)^2 + \left(\frac{1}{\lambda}\right)^2}\,\right]^{-1} \qquad 6.6a$$

$$\lambda_u = \left[\frac{\mu|E|}{2D} + \sqrt{\left(\frac{\mu|E|}{2D}\right)^2 + \left(\frac{1}{\lambda}\right)^2}\,\right]^{-1} \qquad 6.6b$$

Equation 6.6 states that the presence of an electric field in the direction of the spin transport (either parallel or anti-parallel to the spin flow) causes the diffusion length to change depending on the magnitude and direction of the field. In the analysis above where the carriers were assumed to be electrons, the diffusion length of the spin flow in the direction anti-parallel to the electric field direction is increased $(\lambda_d > \lambda)$, while the diffusion length of the spin flow in the direction parallel to the electric field is decreased $(\lambda_u < \lambda)$. In the absence of an electric field ($|E| = 0$), the diffusion lengths reduce to the intrinsic (zero-field) value, $\lambda_d = \lambda_u = \lambda$. The results derived by Yu and Flatté are

important because in practice the electric fields present in spintronic devices are often large enough to cause substantial deviation of the diffusion length from the intrinsic value.

6.1.2 Tuning of nonlocal resistance in graphene nonlocal spin valve by electric field application

The ability to tune the diffusion length in semiconductors by applying an electric field along the direction of the spin transport introduces an additional control parameter that brings more versatility in spintronic devices. This phenomenon could also generate novel ideas for designing spintronic devices. For example, all spin logic (ASL) device applications require that the information flow is unidirectional, i.e. the inputs determine the output states while the outputs should provide no feedback that can change the input states. This could be achieved by enhancing the spin diffusion length of the electrons travel from the inputs to the outputs and suppressing the spin diffusion length in the reverse direction. Given its excellent spin diffusion length that has been observed experimentally, which could even be much higher in theory, graphene is undoubtedly an excellent candidate for the ASL device channel material. It is therefore important to explore methods that not only improve the intrinsic spin transport properties in graphene, but also yield more useful device structures.

Graphene is a semimetal and should obey the drift-diffusion equation for degenerate semiconductors. The spin diffusion length in graphene in the presence of an electric field should in theory be described by equation 6.6. To investigate the predicted phenomenon, a graphene nonlocal spin valve is used together with an independent DC current source connected as shown in figure 6-1. The purpose of the DC current source is

to provide an electric field along the graphene channel, or equivalently the spin flow direction. The spin polarized current is injected through FM1 and spin imbalance is induced in the graphene underneath FM1. In the absence of electric field, part of the induced spin imbalance diffuses to the right of FM1 and arrives at FM2 where it is read as a voltage. Applying DC current (I_E) produces an electric field along the entire length of the graphene channel. By tuning the magnitude and polarity of the current, the magnitude and direction of the resulting electric field can be precisely controlled, if the channel resistance of the graphene is known.

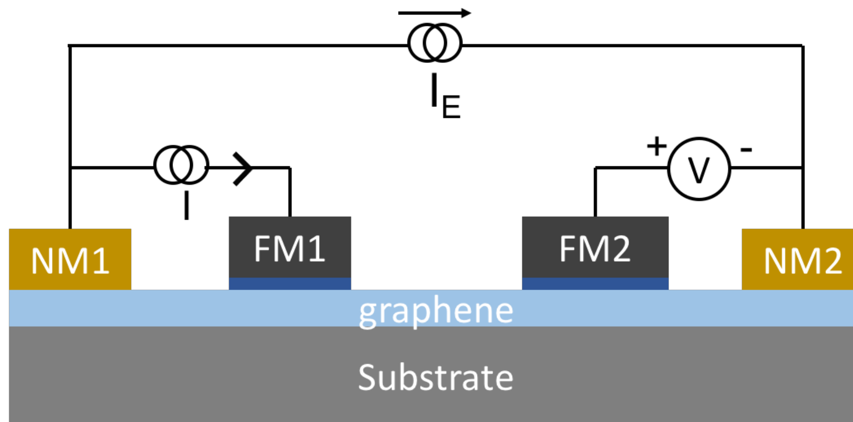

Figure 6-1 Graphene nonlocal spin valve with an independent DC current (I_E) source to produce an electric field along the graphene channel.

The same few-layer graphene nonlocal spin valve, of which the channel resistance and nonlocal resistance dependences on the gate voltage (V_G) were shown in figure 5-13, was used to study the electric field effect. The measurement was performed as follows. After the nonlocal resistance measurement was performed over V_G ranging from -40 V to +40 V, it was determined that the nonlocal resistance value reached a minimum at the Dirac point ($V_G = +20$ V). A constant voltage of $V_G = -35$ V was then applied to the gate to

bring the Fermi level away from the Dirac point and increase the nonlocal resistance. Since this gate voltage value was located to the left of the Dirac point, the carriers in the graphene channel were holes. Keeping V_G constant, the nonlocal resistance was measured while the applied DC current was varied from +400 μA to -400 μA. The plots in figure 6-2 show the evolution of the nonlocal resistance signal at different applied DC currents (I_E). The plots have been intentionally offset in the y-axis to separate out the plots for clarity. Given the configuration shown in figure 6-1, positive applied DC current generates electric field that points to the left (-x direction), while the negative current generates electric field that points to the right. Since the carriers are holes, the electric field pointing to the left relative to the current injection point is expected to suppress the spin diffusion length, resulting in smaller nonlocal resistance signals as the current is increased. This is exactly what is observed in figure 6-2. At large positive I_E, the nonlocal resistance vanished because the suppressed spin diffusion length was much smaller than the injector/detector separation. The opposite effect was observed when negative I_E was applied. The nonlocal resistance signal increased as I_E became more negative and seems to demonstrate saturation at large negative I_E. It remains unclear what causes the saturation of the nonlocal signal at this electric field level. The drift saturation velocity in graphene on SiO_2 was measured to be $> 1 \times 10^7$ cm/s at temperatures ranging from 80 K to 300 K[56], which is about 2 orders of magnitude higher than the drift velocity predicted in our case. Consequently, the saturation at high field could possibly arise due to some other effects, for example the impurities or defects in graphene and/or substrate effect, rather than the intrinsic drift velocity saturation of graphene.

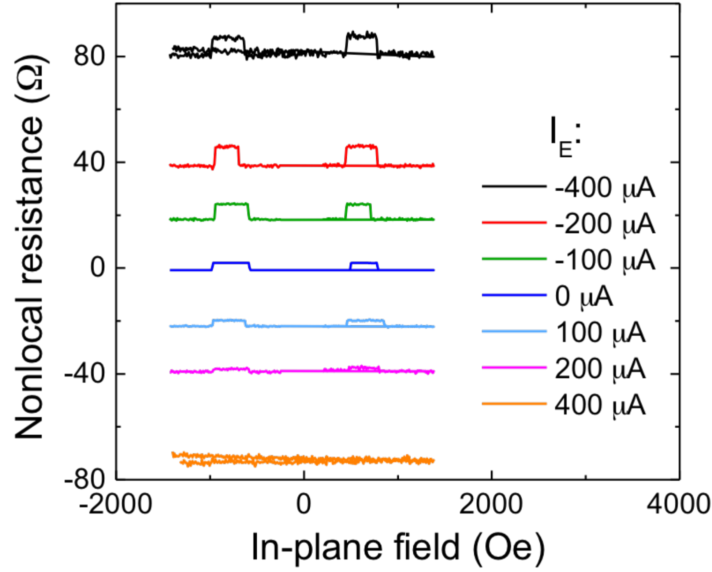

Figure 6-2 Nonlocal resistance plots of the few-layer graphene nonlocal spin valve for different applied current values (I_E). The device, as discussed in the text, was measured at T = 30 K.

In order to provide additional insight into the electric field effect, the spin diffusion length was determined as follows. The device was gated through a back gate with Al_2O_3 oxide thickness of ~170 nm. The channel resistivity at $V_G = -35$ V was measured to be ~915 Ω/sq. The effective mobility at the specified V_G can then be estimated to be $\mu \sim 440\ \mathrm{cm}^2/\mathrm{Vs}$. The injector/detector separation was 5 μm and the graphene channel width was estimated to be around ~2 μm by using AFM. Therefore, the channel resistance between the injector and detector is $R = 915 \frac{\Omega}{sq} \times \frac{L}{W} = 2287.5\ \Omega$. The diffusion coefficient was extracted from the nonlocal Hanle measurement data using the method described in the previous chapter to be $D = 150\ \mathrm{cm}^2/\mathrm{s}$. The electric field in the direction of spin flow between the injector and detector can then be determined by:

$$E = \frac{I_E R}{L} \tag{6.7}$$

Now that the electric field has been determined for all applied DC current values, the upstream and downstream spin diffusion lengths can be determined from equation 6.6 above. Based on these effective diffusion lengths, the expected nonlocal resistance values were calculated as follows. The nonlocal resistance without any applied electric field extrapolated to zero injector/detector separation can be calculated by:

$$\Delta R_{NL0} = \Delta R_{NL} exp(d/\lambda) \tag{6.8}$$

where d is the injector/detector separation, λ the intrinsic diffusion length at $V_G = -35$ V, and ΔR_{NL} the nonlocal resistance at the same gate voltage without any applied electric field. The measured values for these parameters are $\lambda = 4.6$ µm and $\Delta R_{NL} \approx 2.7$ Ω. Therefore, ΔR_{NL0} is essentially the nonlocal resistance that would be measured at zero injector/detector separation in the absence of electric field. In the presence of an electric field, the nonlocal resistance (ΔR_{NL}^*) is then related to the modified spin diffusion lengths by:

$$\Delta R_{NL}^* = \Delta R_{NL0} exp(-d/\lambda^*) \tag{6.9}$$

where $\lambda^* = \lambda_d$ when the electric field negative and $\lambda^* = \lambda_u$ when the electric field is positive. The nonlocal resistance signal as a function of the electric field is shown in figure 6-3. The blue dots represent the measured data and the red solid line represents the calculated values based on the model in equation 6.9. In the positive field regime, the model agrees very well with the measured data up to large electric field values, where the nonlocal resistance almost vanishes. In this regime, the spin diffusion length at E = 1830 V/cm was reduced to 1.6 µm. In the negative field regime, however, the observed data showed larger increase in the nonlocal resistance compared to the predicted values from the model and

the spin diffusion length was increased to 13 μm at E = -1830 V. The calculated spin diffusion length as a function of the applied electric field is shown in figure 6-3b, where the data were obtained from the model in figure 6-3a (solid red line). It should also be pointed out that the slope of the measured nonlocal resistance change in figure 6-3a is not similar between the positive and negative field regimes. It appears that the electric field application through the same contact for the nonlocal voltage detection may have some effects on the spin signal detection efficiency. This effect was not included in the model and further investigation is needed to explain the discrepancy that was observed mainly in the negative electric field case. The efficiency might also arise due to the fact that a few-layer graphene flake which had nonuniform width and thickness was used in this particular experiment. A slightly different experiment performed by Józsa *et al.*[128] where the applied DC current path was completely separate from the nonlocal voltage detection contacts showed electric field effect that was symmetric in the positive and negative regimes, which could be due to more uniform single-layer flake used in the experiment.

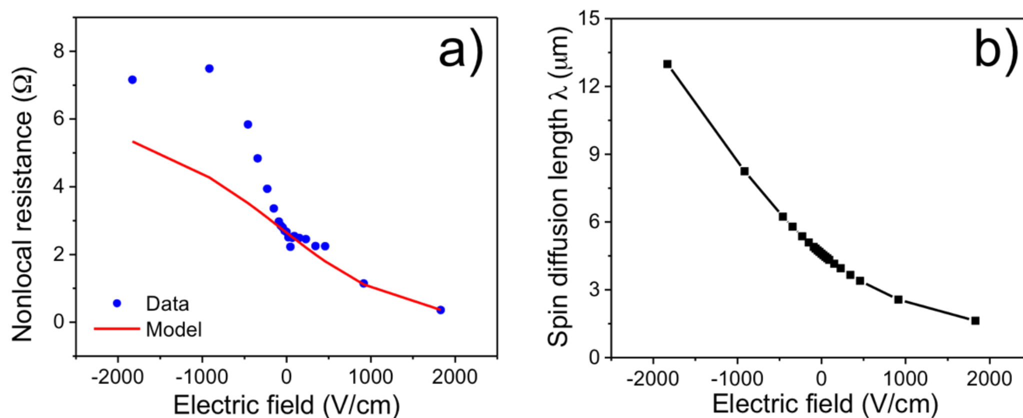

Figure 6-3 The applied electric field effect on spin parameters in few-layer exfoliated graphene. a) Nonlocal resistance as a function of the applied electric field. Blue dots indicate measured data and red solid line the predicted values. b) Calculated spin diffusion length (corresponding to the solid red line in figure a) as a function of the applied electric field.

6.2 Graphene nonlocal spin valve with incorporated double buried-gate structure for asymmetric doping effect investigation

6.2.1 Double buried-gate structure

We have seen that the electric field causes a spin drift effect in graphene spin transport that is comparable to the diffusion effect and therefore is non-negligible. This effect can also be utilized for applications such as graphene-based ASL devices. However, the need for the applied DC current causes extra power dissipation that offsets the advantages that come from the spin signal tuning ability. We investigated an alternative method to control the spin transport properties in graphene by creating a doping asymmetry in the channel between the injector and detector.

6.2.1.1 Device fabrication

To create the doping asymmetry in the graphene channel, the channel is split into two regions independently controlled by two back gates which we refer to as the "double buried-gate" since the two gates are intentionally buried underneath the graphene channel. The structure is fabricated by first patterning two thin Cr/Au metal structures (~30 nm in total) closely separated (~200 nm distance) from each other on a SiO_2/Si substrate (Appendix: Double buried-gate (DBG) structures). Due to its close separation exceeding photolithography resolution, the double buried-gates are patterned using e-beam lithography. Caution must be taken when choosing the right exposure dose as a low dose may be needed to make prevent shorting of the two gates but may result in under-exposure that causes rough gate topography and consequently, rough substrate's surface that could hurt the graphene mobility. A higher dose is therefore chosen to ensure complete exposure

and the offset between the defined gate separation value and the actual value can be determined. By calibrating the exposure dose based on results from test exposures, the desired separation value can then be obtained. The thin metal deposition is followed by Al_2O_3 gate oxide deposition using ALD at 300 ºC. To enable access to the buried gate, a via layer is patterned above the large pads on the thin metal layer. The oxide inside the via layer is etched and a thick metal is deposited to facilitate probing using the gates. After the double-buried gate structure is formed, graphene is deposited on the surface and patterned into mesas of graphene which creates a well-defined geometry. Ohmic contacts are subsequently deposited using the graphene FET fabrication method described in detail in Appendix. The graphene and the Ohmic contacts are positioned such that the gap between the two gates is located exactly in the middle of the graphene channel. The working mechanism of this double buried-gate structure is similar to the regular back-gated graphene FETs, except that now the two halves of the graphene channel are controlled independently by the two gates. Figure 6-4a shows a cross-section schematic view of the structure and figure 6-4b shows an optical micrograph of the double buried-gate graphene FET viewed from the top.

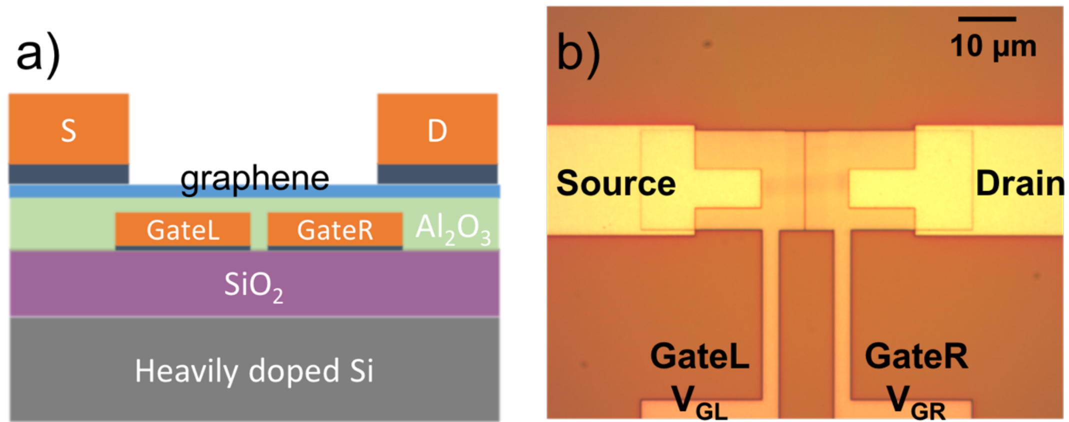

Figure 6-4 Double buried-gate structure. a) Cross-section schematic and b) top-view optical micrograph of graphene FET with double buried-gate structure. Figure a) is exaggerated for clarity.

6.2.1.2 Charge transport characterization

We studied the charge transport characteristics of the double buried-gate FETs fabricated on both mechanically exfoliated few-layer graphene and CVD single-layer graphene. We shall first analyze the few-layer graphene case. The gate oxide used in this device was ~170 nm Al_2O_3. The device structure as shown in figure 6-4b was checked to ensure the two gates are not shorted by applying a voltage between them. Once this has been verified, the drain current was measured as a function of the intentionally shorted two gates, i.e. both gates were applying the same voltage simultaneously. The shorted-gates transfer characteristic curve is shown by the black line in figure 6-5 where the x-axis represents V_{GL}. The Dirac point occurs at $V_{GL} = V_{GR} = 5$ V. The two gates were then swept simultaneously with a differential voltage between them. The transfer characteristics for the differential voltages of 5 , 15 , and 25 V are shown by the solid red, blue, and magenta lines, respectively. There are two noticeable differences between each of the two curves with different differential voltages between the two gates. The first difference is the positions of the Dirac points. Since applying a differential voltage between the two gates

changes the Fermi level of the graphene above one gate relative to the other, the Dirac point is reached twice during the gate sweep. For example, in the case where V_{GR} = V_{GL} + 5 V, the Fermi level of the graphene on the right gate reaches the Dirac point first, and then followed by the graphene on the left gate. This effect is observed in the broadening of the transfer characteristic curve as the different voltage increases and a global Dirac point due to the differential gate voltages emerges in each case. The global Dirac point shifts from 5, 3, 0.5, to -0.5 V, when the differential voltage is changed from 0, 5, 15, to 25 V between the two gates. The second difference is the minimum conductivity which increases monotonically as a function of the differential voltage. As the differential voltage is increased, the Fermi levels of the graphene on the left and right gates move further from each other. As a result, when the Fermi level of the graphene on one gate reaches the Dirac point, the Fermi level on the other gate is still substantially away from the Dirac point, and thus the increased minimum conductivity. The increase in the minimum conductivity displayed in figure 6-5 is small because of the few-layer graphene flake used in the device. In the double buried-gate FET with few-layer graphene, the gates mainly tune the conductivity of the bottom layer, while the top layers are essentially screened from the electric field applied by the gates. The drain current is flowing in all of the layers with the top-most layer, which is directly contacted by the Ohmic contact, carrying the most current compared to any of the layers below it due to the presence of interlayer resistance.

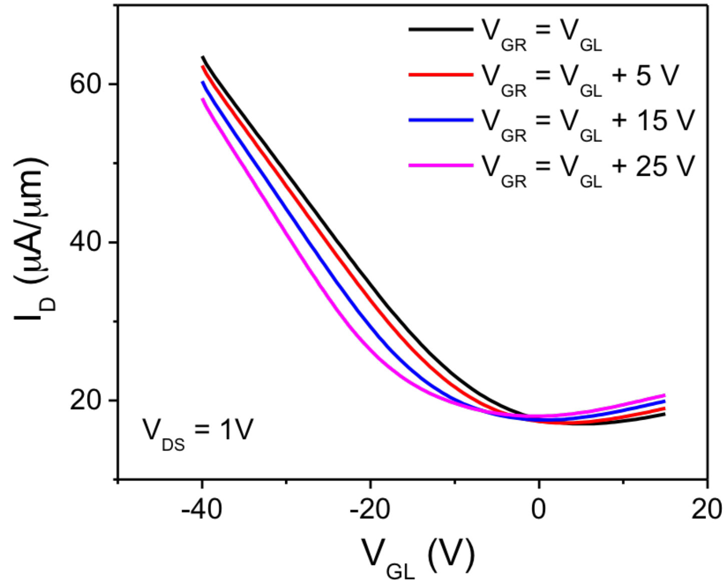

Figure 6-5 Transfer characteristic curves of the double buried-gate FET with few-layer graphene channel.

The electric field from the gate voltage is experienced by the single-layer graphene without being screened. This results in a stronger gate effect on the conductivity of the single-layer graphene, which also carries all of the drain current. The transfer characteristics of the double buried-gate single-layer graphene FET are shown in figure 6-6. The black line corresponds to the case where the two gates are shorted. A sharp single Dirac point is observed in this case, which should be expected because the Fermi level is the same everywhere on the graphene at each gate voltage. The transfer characteristic curves with a gate differential voltage of 5, 15, and 25 V are shown by the red, blue, and magenta lines, respectively. At differential voltage equal to 5 V, the transfer characteristic curve is slightly broadened near the Dirac point. At differential voltages of 15 V and 25 V, two distinct Dirac points are observed. This is because the different Fermi levels that reach the Dirac point at different gate voltages. The same case was not observed in the few-layer

case above because the conductivity change in the few-layer case is small compared to the total conductivity of the channel due to the electric field screening. It can also be seen from figure 6-6 that the minimum conductivity increases as the gate differential voltage increases, which follows the same explanation given in the case of the few-layer graphene above.

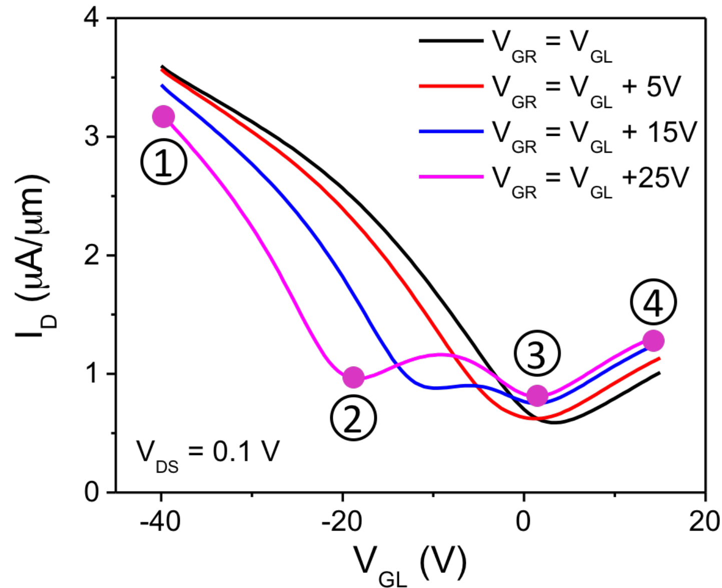

Figure 6-6 Transfer characteristic curves of the double buried-gate FET with CVD single-layer graphene channel. Two Dirac points appear when the gate differential voltages are more than or equal to 15 V.

The positions of the Fermi levels of the graphene channel on the left and right gates relative to each other as well as to the Dirac point for the case of $V_{GR} = V_{GL} + 25$ V in figure 6-6 are shown in figure 7-7. The Fermi levels are shown for the four points indicated by the magenta filled circles in figure 6-6. At point 1, both the Fermi levels of the graphene on both the left and right gates are far below the Dirac point, and thus high hole conductivity. At point 2, the Fermi level of the graphene on the right gate reaches the Dirac

point and the first minimum conductivity is reached. Between point 2 and point 3, the charge carriers in the graphene are different on the left and right gates, which implies that a graphene p-n junction is formed. Point 3 corresponds to the Dirac point of the left gate. At point 4, both Fermi levels are above the Dirac point and the conductivity is now due to electrons. This simple experiment gives a clear picture of the working mechanism of the double buried-gate FET. The difference in gate voltage between two Dirac points that increases with the differential gate voltage clearly indicates that the channel is divided into two regions with different carrier densities that depend on the gate voltage applied to each region. The double buried-gate structure provides a means to control the carrier densities in the two halves of the graphene channel independently, enabling investigation of charge transport across junctions between graphene regions with asymmetric doping concentration or carrier types.

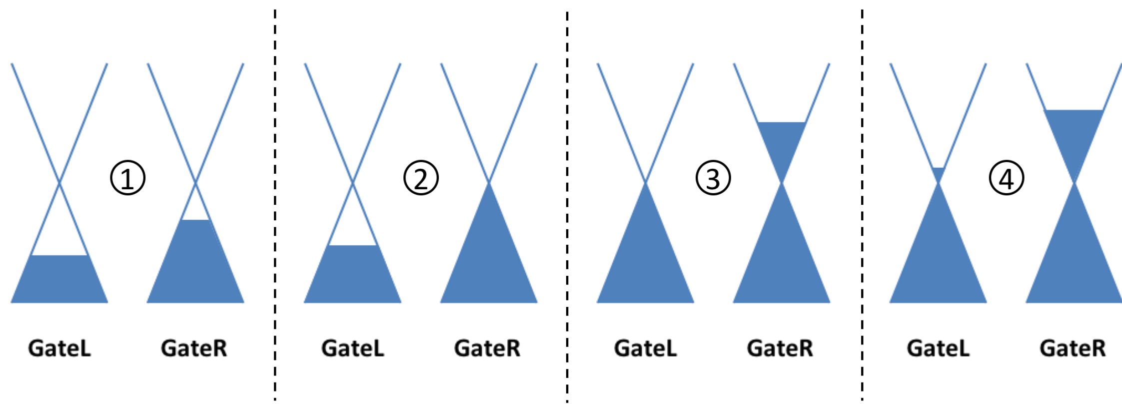

Figure 6-7 Fermi level positions on the left and right gates corresponding to the four points in figure 6-6. The plots are shown for the case where $V_{GR} = V_{GL} + 25$ V. The figure only aims to demonstrate the carrier densities above the two gate regions relative to each other and not the actual band alignment where the Fermi levels on gateL and gateR align at equilibrium.

6.2.2 Graphene nonlocal spin valve with double buried gate

We have looked at how the double buried-gate structure can be incorporated into a graphene FET that has the capability to independently control the doping in the two halves of the graphene channel. This structure enables investigation of the transport properties in graphene across different types of junctions that could be interesting for understanding novel properties of graphene. In this section, we shall look at how the structure was incorporated into a nonlocal spin valve to explore the spin properties of graphene in channels with asymmetric doping.

6.2.2.1 Device fabrication

The fabrication of the graphene nonlocal spin valve with incorporated double buried-gate structure is straightforward and literally a combination of two main steps, i.e. the double buried-gate FET and the nonlocal spin valve. The graphene double buried-gate FET is first fabricated using the procedure described above. The ferromagnetic contacts are then patterned using e-beam lithography, followed by tunnel barrier deposition and ferromagnetic metal and capping layer depositions, similar to the ferromagnetic contact formation in the nonlocal spin valve described in chapter 5. The ferromagnetic injector and detector electrodes are aligned with the double buried-gate underneath such that the separation between the two gates is located half way between the injector and detector to ensure the formation of a junction between two asymmetrically doped regions. The two optical micrographs on the top of figure 6-8 show the top views of the double buried-gate FET structure (left) and the nonlocal spin valve (right). The optical micrograph on the bottom shows the top view of the graphene nonlocal spin valve with incorporated double

buried-gate structure, which is a combination of the two structures shown above it. The illustration in figure 6-9 shows how the different layers are stacked in the incorporated structure and their relative positions to each other.

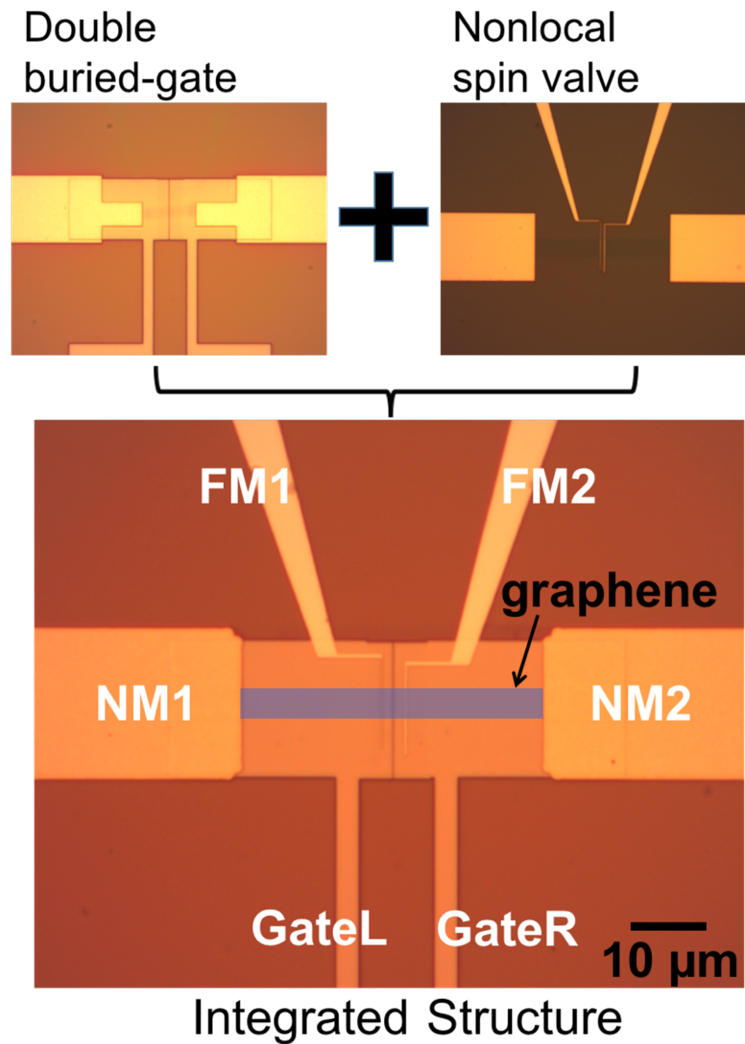

Figure 6-8 Integrated structure: Graphene nonlocal spin valve with double buried-gate. Top: Double buried-gate graphene FET (left) and nonlocal spin valve (right). Bottom: The graphene nonlocal spin valve with incorporated double buried-gate structure.

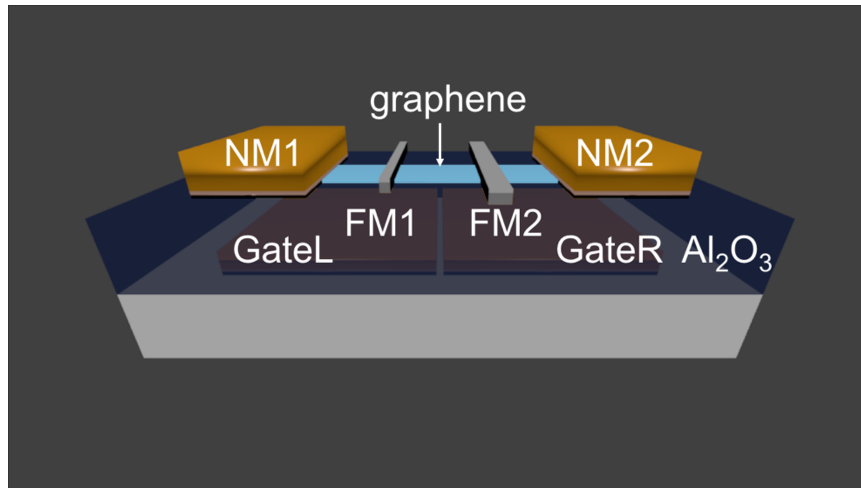

Figure 6-9 Illustration of the integrated graphene nonlocal spin valve with double buried-gate structure.

6.2.2.2 Characterization of the exfoliated few-layer graphene device

The first experiment performed using the nonlocal spin valve with the incorporated double buried-gate structure utilized an exfoliated few-layer graphene channel. Using the two nonmagnetic contacts (NM1 and NM2) and two ferromagnetic contacts (FM1 and FM2), a four-terminal measurement was performed to obtain the channel resistivity of the graphene. Figure 6-10 shows the 2D color contour plot of the exfoliated few-layer graphene channel resistivity as a function of the left and right gate voltages, V_{GL} and V_{GR} at T = 30 K. The Dirac point was shown to be at $V_{GL} \approx 15$ V and $V_{GR} \approx 22$ V. It can be seen from the plot that the channel resistivity decreases as V_{GL} and V_{GR} get further away from the Dirac point, as expected. The plot also gives information on the channel resistivity when one of the gate voltages is kept constant. For example, a vertical line can be drawn at $V_{GR} = -30$ V (shown by the black arrow) as a visual aid that helps in tracing the change in the channel resistivity at constant V_{GR} while V_{GL} is swept. The red arrow indicates the trace for constant $V_{GL} = -30$ V and varying V_{GR}. The channel resistivity can then be obtained for every combination of V_{GL} and V_{GR}.

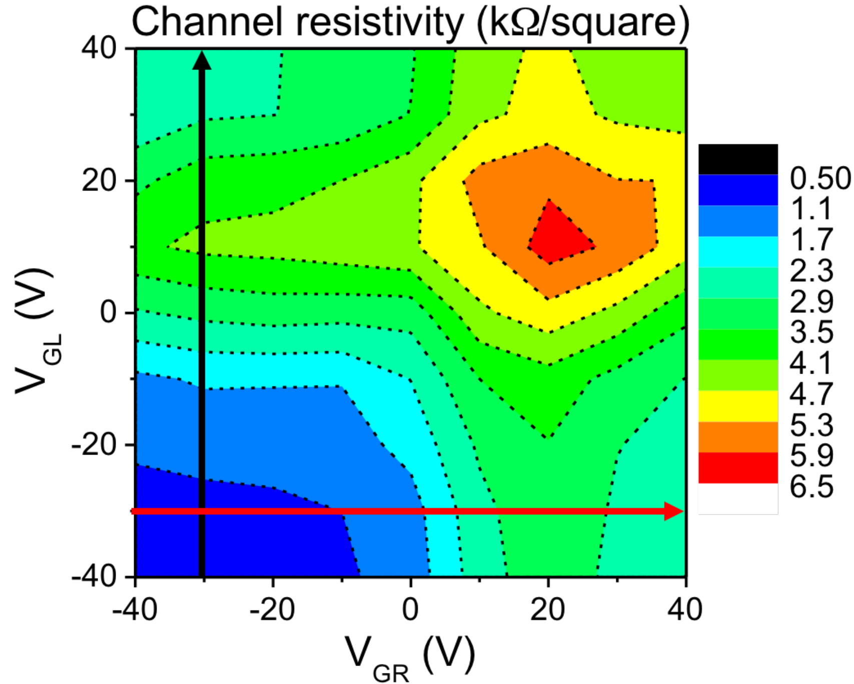

Figure 6-10 Color contour plot of the few-layer graphene channel resistivity as a function of the left and right gate voltages.

Besides the channel resistivity, the nonlocal resistance measurement was also performed at each V_{GL} and V_{GR} combination at T = 30 K. The spin polarized current was injected through the ferromagnetic contact on the left gate region and the nonlocal resistance was measured on the right gate region. The result is displayed in figure 6-11, which shows that the nonlocal resistance reaches a minimum value near the Dirac point. It should be point out that from our previous discussion, this behavior indicates the presence of pinholes in the tunnel barrier between the ferromagnetic contact and the graphene. We shall now analyze the nonlocal resistance change as a function of the left and right gate voltages. The contour plot indicates that the nonlocal resistance changed by a factor of ~10 between the Dirac point and the value at $V_{GL} = V_{GR} = -40\text{ V}$. In this device, the asymmetric gating effect was investigated mainly in the hole regime because the p-type

doping of the channel would require large gate voltages to be applied to access the electron regime. The gate voltages were limited to $\pm 40\ V$ to prevent dielectric breakdown. Along the black arrow, the hole concentration was kept high on the right gate and reduced on the left gate. The nonlocal resistance value decreased as the hole concentration on the left gate decreased. Similarly, along the red arrow, the nonlocal resistance value decreased as the hole concentration on the right gate decreased.

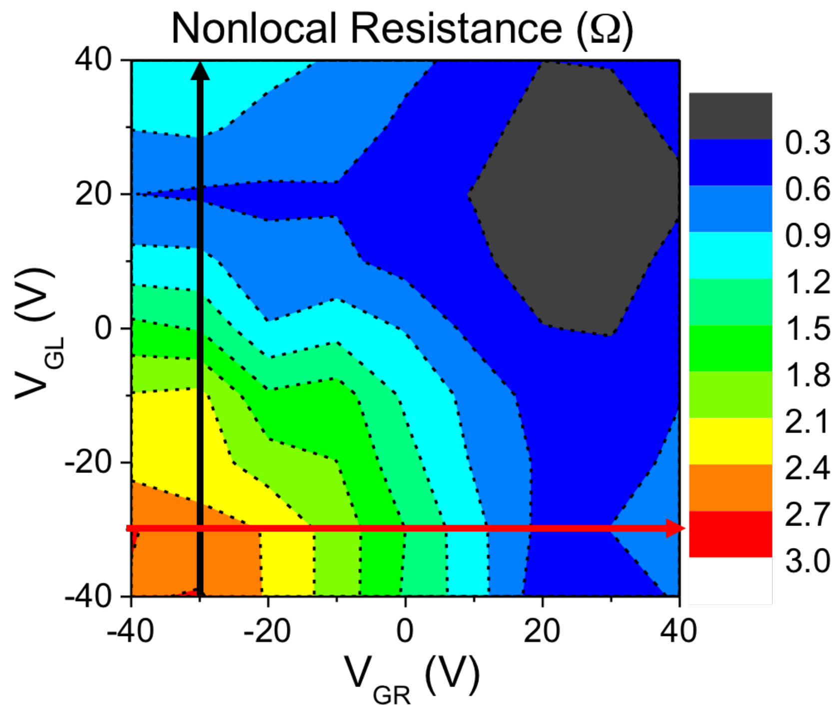

Figure 6-11 Color contour plot of the nonlocal resistance of the exfoliated few-layer graphene device as a function of the left and right gate voltages.

The nonlocal resistance was found to decrease as the hole concentration was decreased for both the left and right gate voltages shown in figure 6-11. No difference in the nonlocal resistance was observed between the case where the spin transport was from a low to a high conductivity regime and the opposite transport direction. The black arrow indicates the case where the spin transport was from the increasingly lower hole

concentration on the left to the high hole concentration on the right. The red arrow indicates the case where the spin transport was from the high hole concentration on the left to the increasingly lower hole concentration on the right. Similar behavior was observed for the spin transport across the two different types of junction and therefore no clear asymmetry arose. Another interesting result from the color contour plot is the transport across a p-n junction. From the charge transport measurement result in figure 6-10, the channel on the left gate entered the electron regime at $V_{GL} > 15$ V and the right gate at $V_{GR} > 22$ V. The nonlocal resistance plot exhibits the same gate voltage dependence when the carrier type changes from hole to electron. It appears that the spin transport is not altered by the p-n junction and theoretical studies on spin transport across a graphene p-n junction could be an interesting topic to investigate.

6.2.2.3 Characterization of the CVD single-layer device

While it is possible to induce doping asymmetry in the few-layer graphene using the double buried-gate structure, the electric field from the gate is screened such that its effect on the layers above the first layer (closest to the substrate) is reduced, resulting in a small change in total doping level and thus weak asymmetry. The theoretical maximum level of doping asymmetry should then be achieved in single-layer graphene. A nonlocal spin valve with incorporated double buried-gate structure was therefore fabricated on CVD single-layer graphene to investigate the maximum doping asymmetry effect. The device was then characterized in the same manner as the exfoliated few-layer graphene device and the measurement was also performed at T = 30 K. Figure 6-12 shows the graphene resistivity plots as a function of V_{GL} and V_{GR} where the maximum resistivity (Dirac) point

is located at $V_{GL} = V_{GR} \approx 18$ V. Since the device exhibited a small gate hysteresis even at T = 30 K (data not shown), the channel resistivity was measured using two different scan patterns. Figure 6-12a shows the results obtained by sweeping V_{GR} at each fixed V_{GL} value, while figure 6-12b shows the results obtained by sweeping V_{GL} at each V_{GR} value. The two plots show that the small gate hysteresis effect was negligible and did not affect the measurement results.

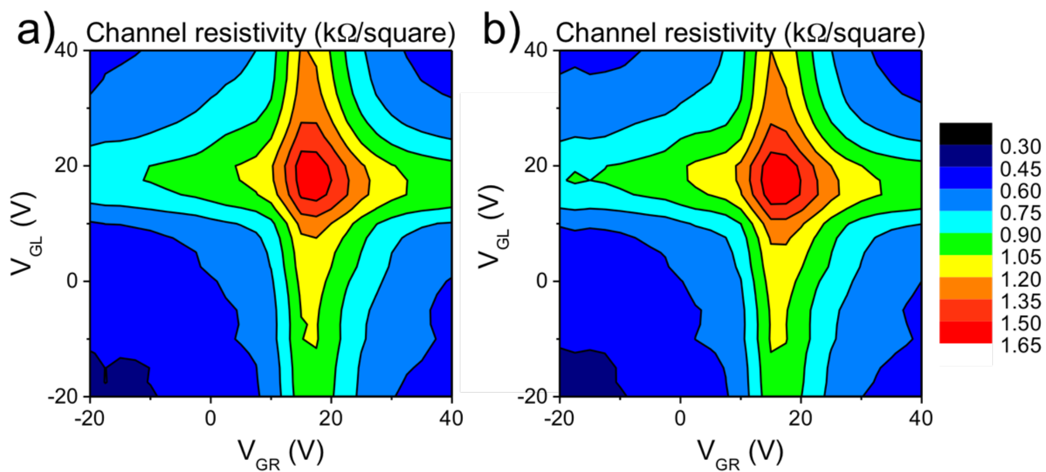

Figure 6-12 Color contour plots of the CVD single-layer graphene resistivity as a function of the left and right gate voltages. Data were obtained by a) sweeping V_{GR} at each V_{GL} point and b) sweeping V_{GL} at each V_{GR} point.

The nonlocal resistance measurement was also performed at each gate combination and the results are plotted in figure 6-13. It can be seen from the plot that the nonlocal resistance reaches its maximum value near the Dirac point, which is indicative of tunneling interface between the ferromagnetic contact and the graphene layer. Following the black arrow at $V_{GR} = -15$ V, the nonlocal resistance is shown to increase as V_{GL} value increased from -15 V and finally reach its maximum near the Dirac point, indicating tunneling behavior. Following the red arrow at $V_{GL} = -15$ V while V_{GR} increased from -15 V, on the

other hand, does not yield the same effect. The nonlocal resistance did not exhibit a substantial increase as V_{GR} got closer to the Dirac point. An asymmetry in the spin transport is present, however the results are at this point inconclusive.

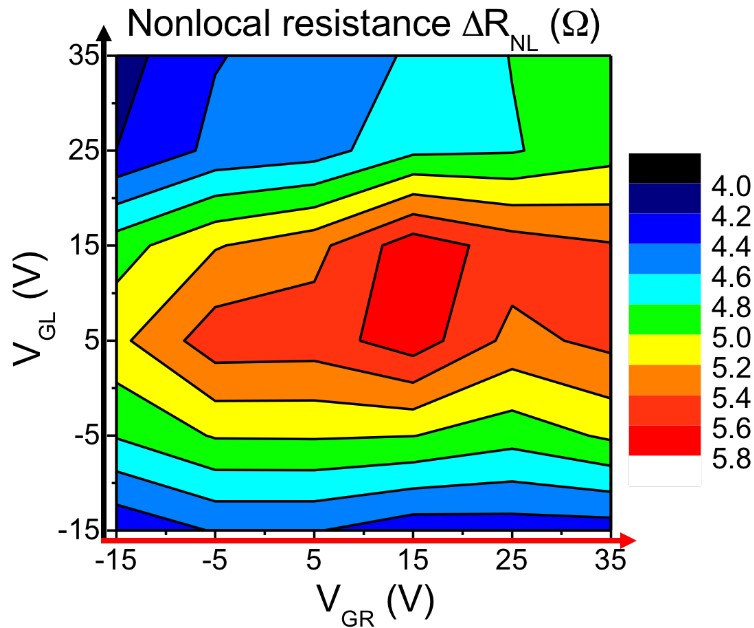

Figure 6-13 Nonlocal resistance plot for the CVD single-layer graphene as a function of the left and right gate voltages with the spin polarized current injected from FM1. The black arrow traces the V_{GL} sweep as V_{GR} is kept at -15 V and the red arrow traces the V_{GR} sweep as V_{GL} is kept at -15 V.

The black arrow in figure 6-13 indicates spin transport from a region with increasingly lower doping to a region with high carrier density, and the red arrow indicates the opposite transport direction. The results shown in figure 13 were obtained where the spin polarized current was injected through FM1 and the nonlocal voltage was measured between FM2 and NM2. The real asymmetry effect would then be reversed if the spin polarized current was injected from the opposite direction. Figure 6-14 shows the nonlocal resistance plot when the spin polarized current was injected through FM2 and the nonlocal voltage was measured between FM1 and NM1. The black arrow in figure 6-14 then

corresponds to spin transport from a region of high doping to a region with increasingly lower doping and the red arrow corresponds to spin transport from an increasingly lower doping region to a region of high doping. Only a weak asymmetry was observed in this case as a function of V_{GR}. The weak dependence of the nonlocal resistance as a function of V_{GR} suggests a contact with weak tunneling behavior. Therefore, it is likely that in our case the contact at FM1 had a tunnel contact with high resistance and good tunneling, while FM2 had a low-resistance tunnel barrier with weak tunneling behavior. This could cause the weak asymmetry observed when the spin current was injected from FM2.

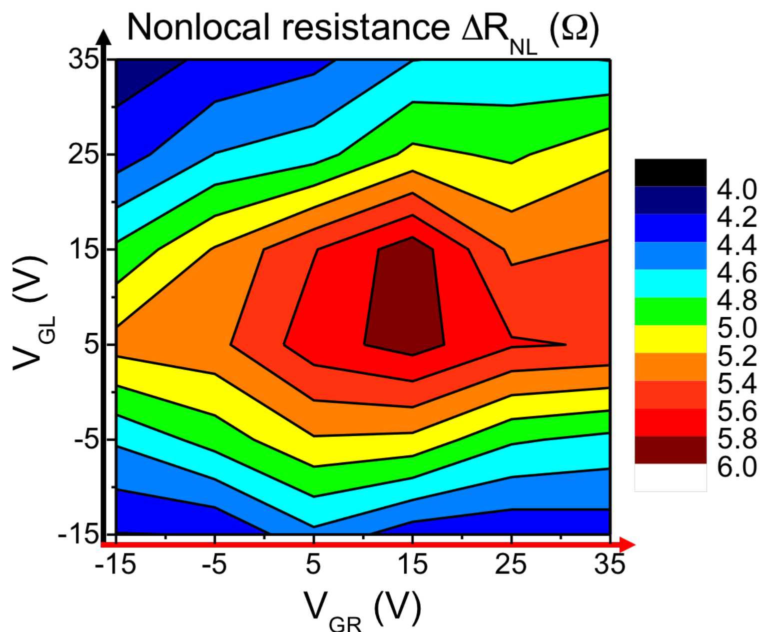

Figure 6-14 Nonlocal resistance plot for the CVD single-layer graphene as a function of the left and right gate voltages with the spin polarized current injected from FM2.

6.2.2.4 Local spin scattering mechanism probed by the double buried-gate structures

It remained to be determined what actually caused the difference in the nonlocal resistance between changing V_{GL} (black arrow) and changing V_{GR} (red arrow). Since no

significant difference was observed between injecting the spin polarized current from FM1 or FM2, only one of the two cases shall be analyzed here in more detail. In figure 6-15, the nonlocal resistance (red squares) is plotted as a function of V_{GL} at fixed $V_{GR} = -15$ V for the case from figure 6-13. As discussed before, the nonlocal resistance appears to increase as V_{GL} gets closer to the Dirac point. The nonlocal resistance is proportional to the channel resistivity (R_{sq}), channel width (W), and effective spin diffusion length (λ) by $\Delta R_{NL} \propto R_{sq}\lambda/W$. The value of R_{sq} (blue line) increases as V_{GL} gets closer to the Dirac point. The effective spin diffusion length (black squares) exhibits a slight increase as V_{GL} gets closer to the Dirac point. This direct dependence between the channel resistivity and the spin diffusion length results in the nonlocal resistance peaking near the Dirac point.

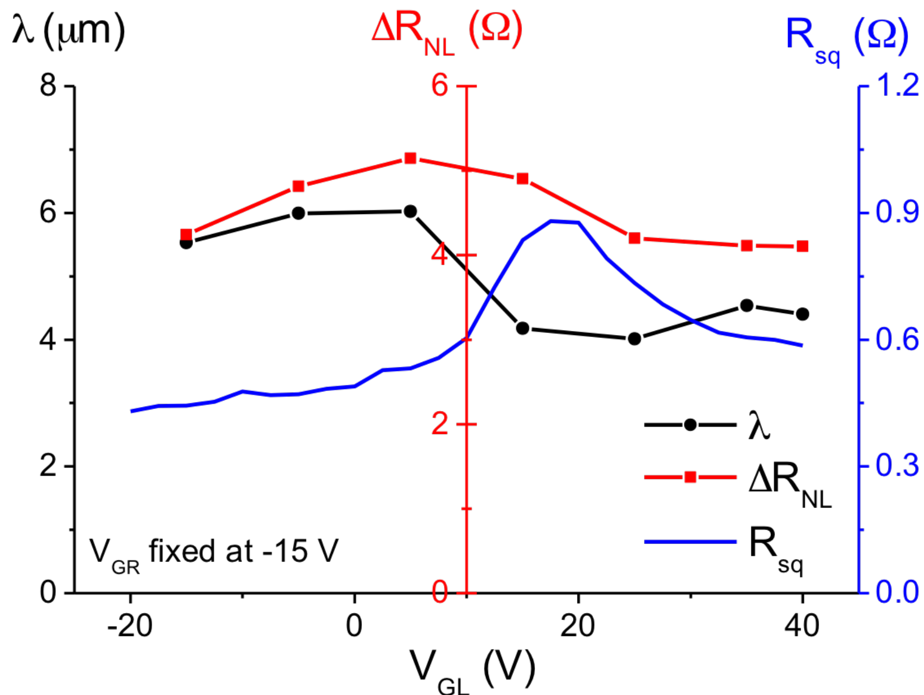

Figure 6-15 Measurement results as a function of only the left gate voltage. Spin diffusion length (black dots), nonlocal resistance (red squares), and channel resistivity (blue line) as functions of V_{GL} at fixed $V_{GR} = -15\,V$.

The situation was different when V_{GR} was swept while V_{GL} was kept constant. From figure 6-13 (indicated by the red arrow), the nonlocal resistance did not experience a significant change as V_{GR} moved closer or away from the Dirac point. The reason behind this different behavior can be seen in figure 6-16. The channel resistivity (R_{sq}, blue line) reaches its maximum at the Dirac point. The effective spin diffusion length in this case (λ, black dots) reaches a minimum at the Dirac point, which is opposite of the observed behavior by sweeping V_{GL}. The inverse dependence of the spin diffusion length and the channel resistivity results in a competing effect on the nonlocal resistance (ΔR_{NL}, red squares), which stays unchanged for a wide range of V_{GR}.

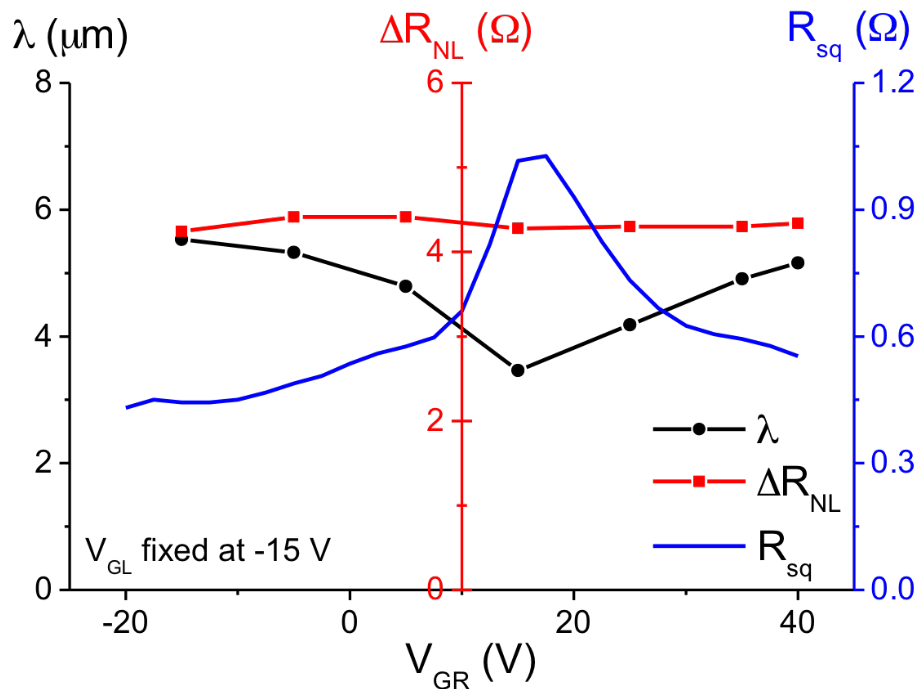

Figure 6-16 Measurement results as a function of only the right gate voltage. Spin diffusion length (black dots), nonlocal resistance (red squares), and channel resistivity (blue line) as functions of V_{GR} at fixed $V_{GL} = -15\ V$.

Changing the injection point from FM1 to FM2 has been shown to result in the same behavior of the nonlocal resistance. This means that the observed asymmetry is not a result of the different injection points, but rather the result of the change in the spin diffusion length in the graphene regions locally gated by the left and right gates. Figure 6-17 shows the relationship between the effective spin relaxation time (τ_S, black dots) and diffusion coefficient (D, blue dots) as the gate voltage is changed. In figure 6-17a, the spin relaxation time appears to show weak correlation to the diffusion coefficient. On the other hand, figure 6-17b shows stronger correlation between the effective spin relaxation time and the effective diffusion coefficient with the increase in the effective diffusion coefficient being accompanied by the increase in the effective spin relaxation time.

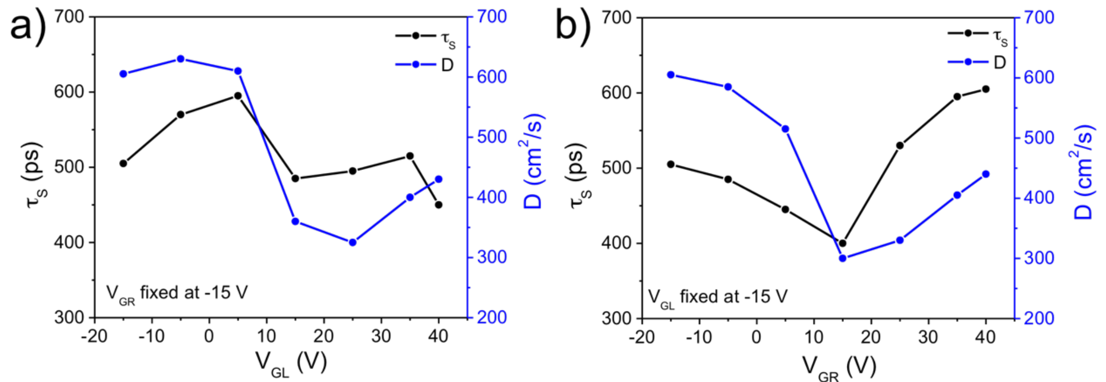

Figure 6-17 Spin parameter comparison between the left and right gate effects. Effective spin relaxation time (τ_S) and diffusion coefficient (D) as functions of the a) left gate voltage (V_{GL}) and b) right gate voltage (V_{GR}).

An interesting phenomenon is revealed by the data in figure 6-17. While the nonlocal resistance value is independent of the injection point, it is dependent on the change in the effective spin diffusion length due to the local change in the left and right halves of the channel. The change in the diffusion coefficient in the left-gated region does not have a strong effect on the spin relaxation time. The scattering mechanism is therefore unclear

in this region. In the right-gated region, however, the change in the diffusion coefficient is followed by the direct change in the spin relaxation time ($\tau_S \propto D$), indicating that the spin scattering in this region is due to the EY mechanism. The above result has a significant implication: the spin scattering mechanism in graphene is strongly dependent on the local condition of the graphene. The spin scattering mechanism in graphene can differ not only between different samples or devices, but it can also differ between two local regions of a graphene channel. In our case, the spin scattering mechanism differs between two small regions within the length of the graphene channel that is only ~2 μm.

6.2.3 Double buried-gate in graphene-based ASL devices

The weak asymmetry in the form of the nonlocal resistance could be due to the interface effect (e.g. tunneling at FM1 while pinhole at FM2) that dominates the measured nonlocal resistance value. However, it is clear that the measured spin signal appears to peak near the Dirac point. Here, we attempt to estimate the spin current injected into the detector for the case of figures 6-13 and 6-14. The measured nonlocal voltage $\Delta V_{NL} = \Delta R_{NL} \times I_{inj}$, where I_{inj} is the current injected from FM1, can be expressed as:

$$\Delta V_{NL} = \frac{\alpha}{e}(\mu_{\uparrow} - \mu_{\downarrow}) \qquad 6.10$$

where $\mu_{\uparrow}$ ($\mu_{\downarrow}$) is the spin-up (spin-down) electrochemical potential in the graphene underneath the detector. Since the ferromagnet is much more conductive than the interface resistance, the total resistance of the contact (ferromagnet plus interface) is then approximately equal to the interface resistance. The spin current density going into the detector can then be estimated by:

$$j_{s,det} = \frac{1}{eR_C}(\mu_\uparrow - \mu_\downarrow) = \frac{\Delta V_{NL}}{\alpha R_C} \quad 6.11$$

where R_C is the interface (contact) resistance. Figure 6-18 shows the plots for the estimated $j_{s,det}$. The plots do not perfectly correspond to the nonlocal resistance plots due to the changing R_C with changing gate voltages. Let us now consider two points on the plots indicated by the black dots in figures 6-18a and 6-18b, which correspond to the cases plotted in figures 6-13 and 6-14, respectively. In figure 6-18a, where V_{GL} is near the Dirac point while V_{GR} is far from the Dirac point, $j_{s,det} \approx 3.5\ \mathrm{A/cm^2}$, while in figure 6-18b $j_{s,det} \approx 2.4\ \mathrm{A/cm^2}$. This asymmetry was most likely due to the difference in the interface at FM1 (tunneling) and FM2 (weak tunneling) that led to more current flowing into FM2.

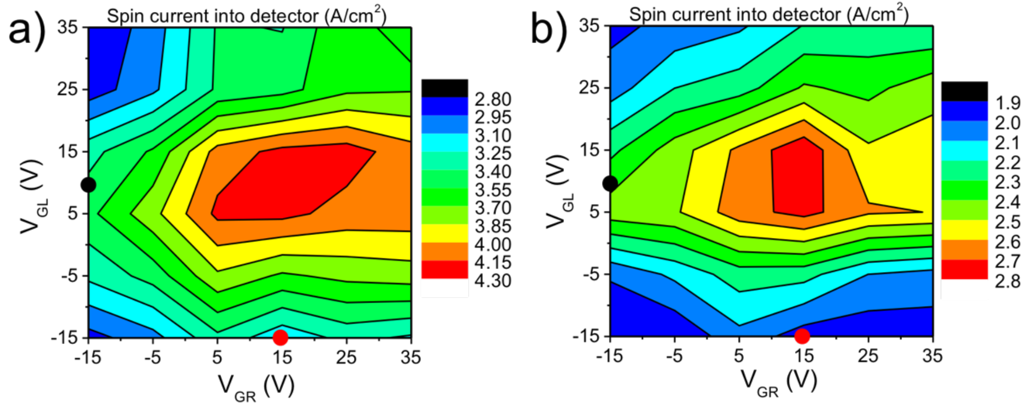

Figure 6-18 Estimated spin current injected into the detector. The spin current was injected from a) FM1 and detected at FM2 (figure 6-13) and b) FM2 and detected at FM1 (figure 6-14).

Now let us consider the asymmetry due to the gating effect. To do this, let us compare the two points indicated by the black and red dots in figure 6-18a. The black dot marks the case where the spin current was injected into the low-doped region $V_{GL} = 10$ V and detected in the highly-doped region $V_{GR} = -15$ V. The red dot, on the other hand, marks the case where the spin current was injected into the highly-doped region $V_{GL} =$

-15 V and detected in the low-doped region $V_{GR} = 15$ V. At the black dot, $j_{s,det} \approx 3.5\ \mathrm{A/cm^2}$ and at the red dot, $j_{s,det} \approx 3.2\ \mathrm{A/cm^2}$. Indeed, some asymmetry was observed when the spin current was flowing from the lower doped region to the more highly doped region, compared to the opposite case. It is unclear why the situation was not reversed in figure 6-18b, where the spin current injected into the detector (in this case FM1) remained to be dependent mainly on V_{GL}. Future experiments could provide additional insight in devices where both V_{GL} and V_{GR} have equally strong effect on the spin signal.

The double buried-gate structure could also be incorporated into graphene-based ASL devices. One way to do that is shown in figure 6-19. The structure could be fabricated as follows. The double buried-gate structures are buried inside the gate oxide, same as the previously described double buried-gate structures. The oxide is then etched and a metal layer is deposited as the ground for spin current injection. A tunnel barrier is deposited on top of the ground metal to reduce the injected spin current flowing into the metal ground. Graphene is deposited on the substrate and patterned into isolated strips. A resist layer is patterned for the tunnel barrier and FM deposition. The tunnel barrier is deposited at an angle such that only the graphene on the input side is covered by the tunnel barrier. The FM metal is deposited last. A single device consisting of an input and an output is marked by the red dashed line. In this device, the spin polarized current is injected from the input with tunnel barrier and travels to the output where it can be used to switch the magnetization direction during the logic operation. The spin polarized current can be maximized by applying the left gate voltage close to the Dirac point. The right gate can be tuned accordingly to maximize the spin current injected into the detector.

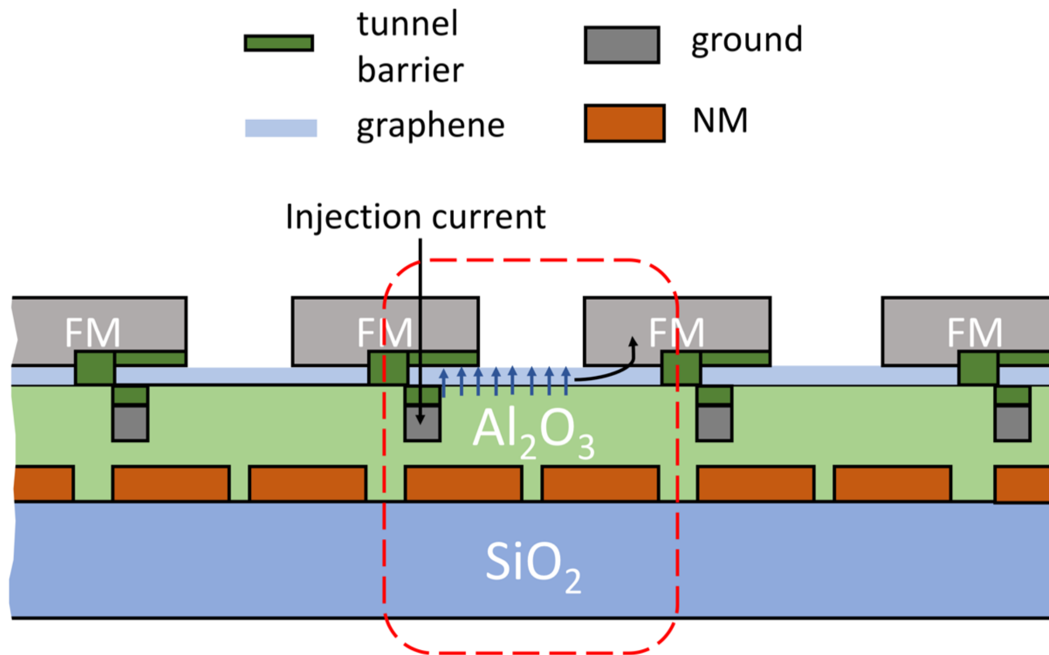

Figure 6-19 Possible design for graphene-based ASL devices with double buried-gate structures. The tunnel barrier is deposited using angled-deposition method to cover the graphene strips underneath the input magnets to improve the spin injection efficiency. At the output magnets, the graphene/FM interface is transparent to maximize the spin current going into the output magnets.

The asymmetry due to the different interfaces at the spin injector (tunneling interface) and detector (pinhole or transparent) that favors the spin transport from the injector to the detector rather than the spin transport in the opposite direction makes intuitive sense because the tunneling contact produces larger spin polarization. Through the gating effect, we expect that larger spin polarized current should be generated in graphene with lower doping than with higher doping. Although our experimental results did not exhibit strong asymmetry, we believe further investigation is needed to draw a more definitive conclusion. Furthermore, the double buried-gate structure could still provide the flexibility in tuning the amount of spin current flowing into the output in ASL devices without affecting the input condition, which could not be done by using only one global gate.

CHAPTER 7 FUTURE DIRECTIONS AND CONCLUSION

7.1 Potential applications of graphene spintronics

The all spin logic (ASL) device with built-in memory concept originally proposed by Behin-Aein *et al.*[37] could be an application where graphene can potentially play a critical role. Graphene is very suitable for the channel material in ASL devices due to its long spin diffusion length, which could substantially reduce the power consumption in these devices by reducing the number of buffers needed.[213] In an ASL device, it is the torque exerted by the spins that switches the magnetization direction of the output magnet through the mechanism referred to as the spin transfer torque (STT). The switching of the magnetization direction purely by the carrier spins has not been demonstrated experimentally in graphene lateral spin valve devices. The magnetization switching assisted by externally applied magnetic field, however, has been demonstrated.[157] In the experiment, the externally applied magnetic field was brought close to the coercive field of the output magnet before a large DC current (a few mA) was injected from the input magnet. This highlights the difficulty in realizing STT switching of magnetization in graphene devices. One of the two schemes proposed by Behin-Aein *et al.* utilizes a power supply that is directly applied to the output magnet to set its magnetization direction to the neutral state. This could significantly reduce the amount of injected current required to switch the output magnet. However, this scheme would require a more sophisticated clocking scheme and it is unclear whether the structure can indeed be designed and fabricated to realize the voltage controlled anisotropy at the output magnet.

One way to bring graphene-based ASL devices closer to realization is by closing the gap between the experimentally measured spin diffusion length and the theoretically predicted limit, which could enhance the spin current and consequently the spin transfer torque. This is being addressed by all experimental work on spin transport in graphene aimed at determining the main scattering mechanism as well as increasing the spin relaxation time in graphene. An increase in the spin injection efficiency by developing high-quality and pinhole-free tunnel barriers would also be beneficial in achieving larger spin current. The use of Heusler alloys, which have an almost complete spin polarization, as an alternative spin injector into graphene as opposed to the traditional ferromagnets such as cobalt and permalloy, for example, is also currently being studied. Due to its close to 100% spin polarization, spin injection from a Heusler alloy could potentially result in larger spin current in the graphene channel.

While it is important to continue to improve the spin injection and transport properties in graphene, it is equally important to be able to engineer a magnet with low damping constant that could be switched by much smaller spin torque. Recent results on enhanced perpendicular magnetic anisotropy (PMA) in thin graphene-coated cobalt show that it is possible to engineer graphene/ferromagnet heterostructures with large PMA.[214] Their orbital-hybridization-resolved analysis revealed that the enhanced PMA is due to the hybridization of the d_z^2 and d_{yz} orbitals in the presence of graphene. The first-principles calculations showed that in when a thin cobalt layer is in contact with graphene on its top and bottom surfaces, the PMA can be maintained for cobalt layer with thickness up to ~25 Å or equivalent to 12.5 monolayers (ML), beyond which the effective anisotropy switches

signs and the easy axis of the magnetization changes from perpendicular to parallel to the cobalt surface. The results were also confirmed by the experiments with only one side of the cobalt layer covered by graphene. The PMA was shown to persist up to 13 ML of cobalt in this case, which was higher than the predicted 6 ML. The results mark a promising start for graphene spintronic devices with PMA materials. In addition to the low damping constant, PMA materials also have high thermal density and can yield higher device density compared to materials with parallel magnetic anisotropy. Therefore, by incorporating PMA materials could potentially enable the realization of thermally stable, low power, and high density graphene-based ASL devices.

7.2 Phosphorene for spintronics beyond graphene

The spin properties of other emerging materials besides graphene are also interesting. For example, MoS_2, which has large spin-orbit coupling, is interesting for exploring the spin Hall effects. Unlike graphene, single-layer MoS_2 has a finite band gap and therefore high current on/off ratio, which makes it readily incorporable to the field-effect transistors. Engineering heterostructures of graphene and MoS_2 or other transition metal dichalcogenides could enable new device concepts that utilize both the strong spin Hall effects in the transition metal dichalcogenides and the long spin diffusion length in graphene for better spin current generation and detection.

Besides transition metal dichalcogenides, another material that is also interesting is phosphorene, which is the few-layer form of black phosphorus that has recently been reported to have numerous interesting properties, such as a thickness-dependent band gap, high carrier mobility, asymmetric in-plane effective mass, and a variety of other

attributes.[215–220] While the electronic and optoelectronic applications of this material have been widely studied,[221–223] its spintronic aspects are for the most part unexplored. Due to its low spin-orbit coupling coupled with its high carrier mobility, phosphorene is likely to have long spin diffusion length at room temperature. The +1/2 nuclear spin of phosphorus[224,225] offers an interesting platform to investigate spin transport in a material where only the hyperfine interaction is important. Furthermore, semiconductor-to-metallic transition in phosphorene[226] when the material is strained could also reveal spin behavior as the material phase is tuned between different states.

Spin transport studies in two-dimensional (2D) materials have primarily been focused on graphene.[113,126,127,130,131,134,142] The conductivity mismatch problem, which inhibits the spin injection from a ferromagnetic (FM) contact into most semiconductor channels,[160,165] is also observed in graphene-based spin valves. The tunnel barrier insertion at the interface between FM and graphene or semiconductor has been shown to circumvent the conductivity mismatch, as indicated by the increased nonlocal magnetoresistance signal compared to the transparent (no tunnel barrier) contact case.[130,173] The tunnel barrier is made of a thin oxide layer (~1 nm) and therefore requires additional fabrication steps. The small thickness also causes the tunnel barrier to be easily broken by application of large voltages or static charges. The Schottky barrier is also known to enable injection of spin polarized electrons and it has been used in FM/AlGaAs semiconductor spin-LEDs[172] and FM/GaAs spin valves.[174] The efficient spin injection using a simpler, tunable structure by utilizing the Schottky barrier has been demonstrated. Unlike in graphene, where the zero band gap prevents the formation of Schottky barrier, the presence of band gap in

phosphorene could enable spin injection using the Schottky barrier. We investigated the direct cobalt (Co) and permalloy (Py) contacts to few-layer phosphorene in detail. The results are presented here that show the Schottky barrier height of each contact and the tunability of the effective barrier height using an applied back gate voltage.

The few-layer phosphorene was obtained from a bulk black phosphorus crystal onto a 300-nm SiO_2 layer using the scotch-tape method similar to that for graphene. The SiO_2 oxide had been grown on a heavily n-doped silicon substrate, which was also used as the back gate. The few-layer phosphorene flake was protected with PMMA resist right after exfoliation to minimize flake degradation due to ambient condition.[227] The ferromagnetic contacts were patterned using electron beam lithography, after which 40 nm of Co or permalloy was deposited by electron beam physical evaporation system under high vacuum. The fabricated device was immediately transferred into a high-vacuum (10^{-6} Torr base pressure) cryogenic probe station after the metal lift-off step for electrical characterization. Figure 7-1 shows a schematic of the device geometry. For both devices, the separation between the two FM contacts was 1 μm, while the channel widths were 1.8 μm and 2.3 μm for the Co and Py devices, respectively. The step heights obtained by AFM indicate that the flakes in both the Co and Py devices have similar thickness (~10–12 nm). The drain current, I_D, vs. back gate voltage, V_{BG}, curves or the transfer characteristics of the Co- and Py-contacted phosphorene devices at room temperature are shown in figure 7-2. Both devices display p-type behavior and both have similar voltages at which the minimum conductivity point occurs. However, the Py devices show higher on-to-off current ratio, higher drive current, and generally a more asymmetric I_D–V_{BG} curve than for Co. The inset

of figure 7-2 shows the extracted hole mobility (measured at $V_{DS} = +0.5\,\text{V}$) vs. temperature for both contact types. The mobility was measured at the value of V_{BG} where the maximum transconductance ($g_m = dI_D/dV_{BG}$) value of the I_D vs. V_{BG} curve occurs, after which the contact resistance of the FM/phosphorene interface starts to dominate over the phosphorene channel. Fairly similar behavior of the mobility as a function of temperature was observed for both samples, with the slight discrepancy likely due to the contact resistance effects as well as small difference in the number of phosphorene layers in the channel.

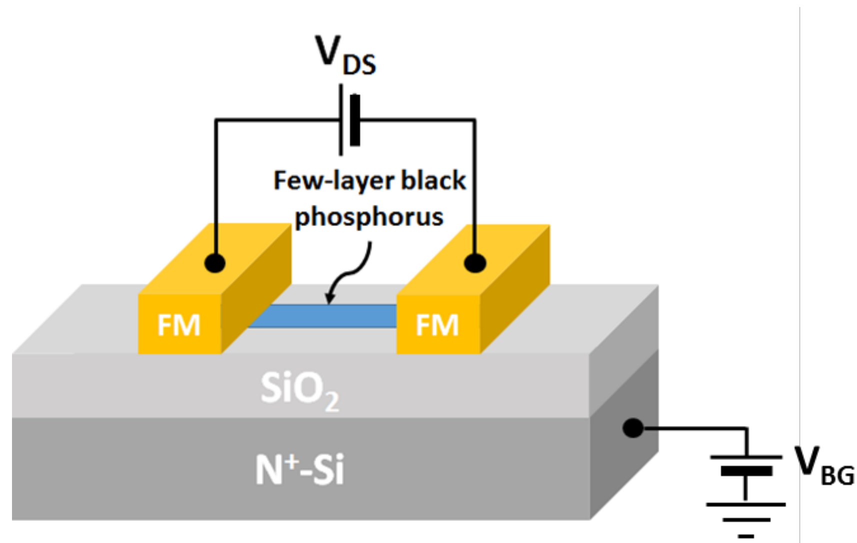

Figure 7-1 Schematic of the few-layer phosphorene back-gated device. Reprinted from Anugrah et al. [229] with the permission of AIP Publishing.

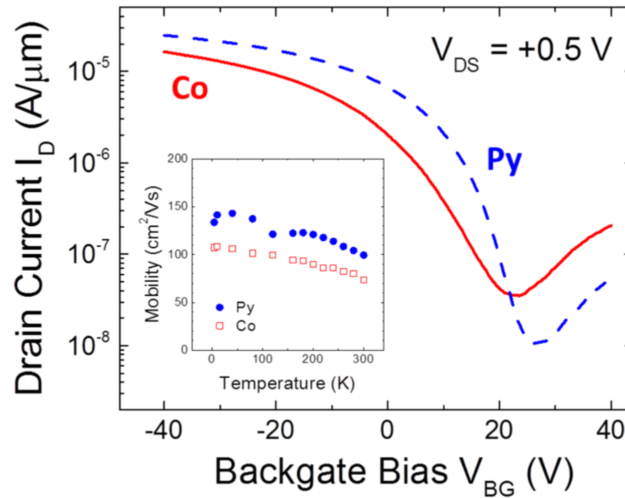

Figure 7-2 Transfer characteristic curves for the few-layer phosphorene devices. Cobalt (red solid line) and permalloy (blue dashed line) were used as the ferromagnetic contacts. The inset shows the hole mobility as a function of temperature for both cases. Reprinted from Anugrah et al. [229] with the permission of AIP Publishing.

Figures 7-3a and 7-3b show the temperature-dependent I_D vs. V_{BG} characteristics of the same few-layer phosphorene FETs as in figure 7-2. As expected, the on-to-off current ratio increases with decreasing temperature for both devices, which is indicative of thermionic conduction-dominated behavior. At large negative gate voltages, however, the temperature dependence of the current practically vanishes, which is indicative of tunneling conduction. Therefore, the thermionic conduction is only applicable in the region where the gate voltages are close to minimum conductivity point, where no saturation due to the tunneling current happens.

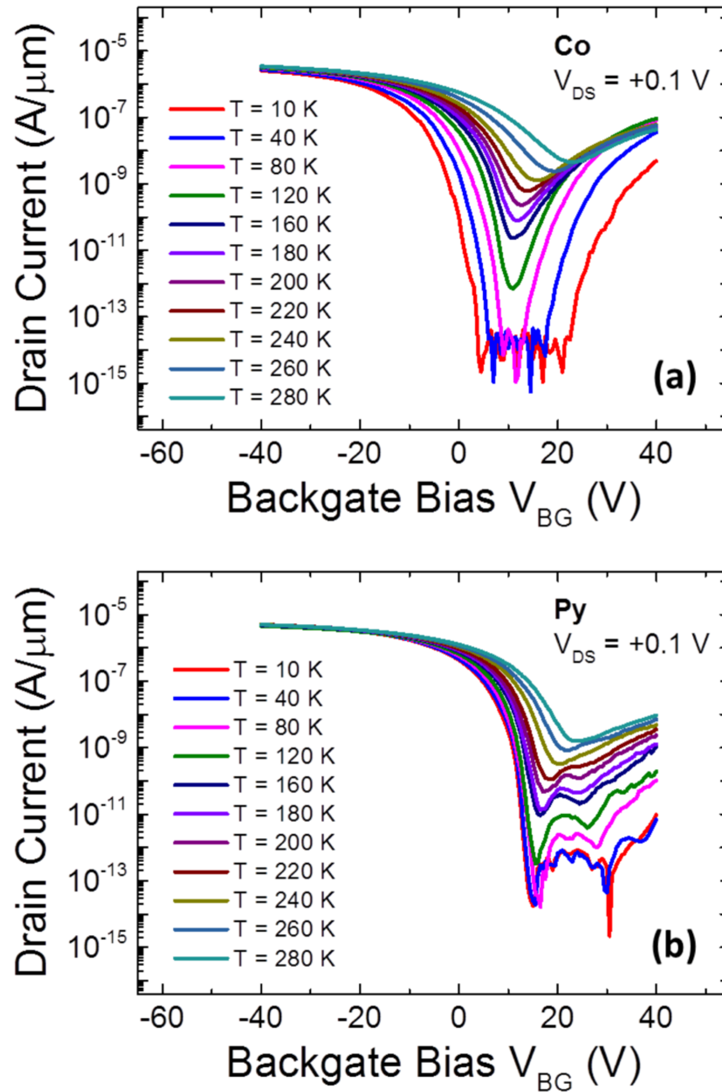

Figure 7-3 Evolution of the transfer characteristic curves as a function of temperature. Data are shown for a) cobalt-contacted and b) permalloy-contacted devices. Reprinted from Anugrah et al. [229] with the permission of AIP Publishing.

To investigate the Schottky barrier formation in phosphorene-based spin valves, it is important to study the ferromagnetic contact to phosphorene. The Schottky barrier can potentially be used to allow efficient spin injection into phosphorene while suppressing the

spin sinking back into the ferromagnet.[173,228] Since the transfer characteristics clearly indicate thermionic conduction behavior at small gate voltages, we utilized temperature-dependent data to generate information on the Schottky barrier height at the interface between the few-layer phosphorene and Co and Py, separately. This was done by analyzing the experimental data with the bulk thermionic emission equation, which provides an estimate for the current in a reverse-biased Schottky diode:

$$I_D \propto A^* T^2 exp\left[-\frac{1}{k_B T}\left(\Phi_B - \frac{qV_{DS}}{n}\right)\right] \qquad 7.1$$

Here, A^* is the modified Richardson constant, q is the electronic charge, k_B is Boltzmann's constant, T is the temperature, n is the ideality factor, and Φ_B is the Schottky barrier height, defined as the energy difference between the FM Fermi energy and the valence band edge of the phosphorene. The $\frac{qV_{DS}}{n}$ term in the exponential reflects the degree of barrier lowering provided by the application of a finite source-to-drain voltage. The Arrhenius plots, $ln(I_D/T^2)$ versus $1/k_B T$, at different source-to-drain voltages as shown in figure 7-4a, were first constructed to extract the value of Φ_B at each back-gate voltage. The example shown is for the Arrhenius plots at $V_{BG} = +10$ V for the device with Py contacts. To ensure the charge transport across the FM/phosphorene interface was dominated by transport across the Schottky barrier and not limited by trapped states on the interface, the temperature range (~200 – 300 K) in the experiment was chosen. The slope of each of the Arrhenius plot is equal to $(qV_{DS}/n - \Phi_B)$, therefore, the effective Schottky barrier height, as shown in figure 7-4b, can be determined by finding the slope at each V_{DS} and extrapolating the result to $V_{DS} = 0$.

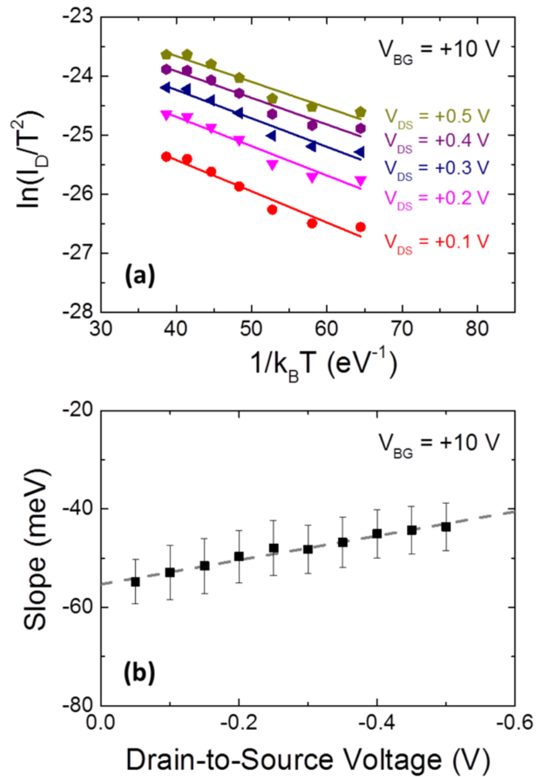

Figure 7-4 Example Arrhenius plots for the few-layer phosphorene device with Py contact at $V_{BG} = +10\ V$. b) The slopes of the Arrhenius plots in a) and the zero extrapolation corresponds to the Schottky barrier height at the that V_{BG}. Reprinted from Anugrah et al. [229] with the permission of AIP Publishing.

Figure 7-5 shows the plots of Schottky barrier height Φ_B vs the applied back gate voltage V_{BG} for both Co and Py devices. Flat-band barrier heights, Φ_{B0}, of ~200 meV and ~110 meV were extracted for the Co- and Py-contacted devices, respectively. These values were determined from the points where the slopes deviated from the linear region shown by the solid lines on the Φ_B vs. V_{BG} plots in figure 7-5. The same slope of the linear region in the Φ_B vs. V_{BG} plot for the Py device (57 meV/V) was used for the Co device, a reasonable assumption made based on the ambipolar nature of the Co device as well as the similarity of the flake thickness in both devices. The values of Φ_{B0} were defined to be the

points where the slope of Φ_B vs. V_{BG} is reduced by ½. The criterion for determining Φ_{B0} has not been well established in the literature, and we have used the ½ slope criterion as an estimate. The band gap in our samples was estimated to 0.5–0.6 eV based on the available data in the literature[217], and this means the barrier height extracted for the Co contacts is near mid-gap, which explains the near ambipolar behavior in figures 7-2 and 7-3, while the lower barrier height for Py is reflected in its more p-type behavior. The higher value of the flat-band barrier height for the Co device compared to the Py device was unexpected due to the higher work function in Co (~5.0 eV) compared to Py (~4.8 eV). This result suggests that the barrier height was not only determined by the work functions of the contact materials, but also possibly by other effects, such as surface defects and oxide formation at the interface, particularly given the reactive nature of both phosphorene and FM materials. More studies are therefore needed to fully understand the Schottky barrier formation at the FM/phosphorene interface.

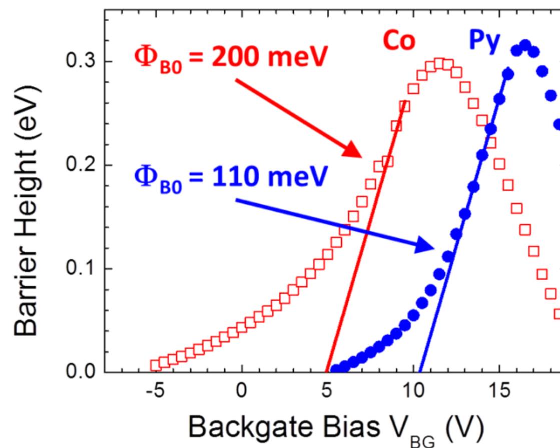

Figure 7-5 Schottky barrier height as a function of V_{BG}. The flat-band barrier heights for cobalt and permalloy contacts are indicated by the red and blue arrows, respectively. Reprinted from Anugrah et al. [229] with the permission of AIP Publishing.

Similar to graphene, the weak spin-orbit coupling and high carrier mobility in phosphorene could be manifested as the long spin diffusion length at room temperature. Additionally, the presence of band gap in phosphorene makes it compatible with FET applications. Our results above suggest that the tuning of Schottky barrier height at the FM/phosphorene interface could enable spin injection into the phosphorene without the need for a physical (oxide-based) tunnel barrier, which is a necessary element in graphene-based spin valves. This could give phosphorene-based spin devices robustness against tunnel barrier damage due to electrostatic charges or large charge current application across the FM/phosphorene interface.

7.3 Conclusion

The history of spintronics was briefly discussed from the first observation of the nuclear polarization in InSb to the spin polarization in aluminium below its superconducting transition temperature and to the first room-temperature spin injection into copper. The discovery of TMR followed by GMR that led to significant technological importance was also discussed. The progress made in the field of spintronics led to more research in this area that finally extended to the semiconductor materials. Although the spin diffusion length is longer in semiconductors, spin injection into semiconductor had been inhibited by its conductivity mismatch with the spin injector, typically a ferromagnet. The role of tunnel barrier to circumvent the conductivity mismatch was then explained. Finally, graphene was introduced as an excellent spin coherent material that has a very long spin diffusion length.

Our experiment endeavor started with the production of graphene by mechanical exfoliation of bulk graphite (HOPG) source and CVD growth. The material characterization of the resulting graphene using optical microscopy, Raman spectroscopy, and AFM was presented. The formation of good and consistent Ohmic contact to graphene was shown to be achieved by using Cr/Au combination. The charge transport properties of graphene were then studied by analyzing measurement results from graphene-based field effect transistors (GFET), some of which indicated the presence of interface traps at the graphene/gate oxide interface.

The spin transport properties of graphene were then carefully studied, starting from the development of the tunnel barrier for efficient spin injection into graphene. Our tunnel barrier deposition method by sputtering of Al and oxidizing in oxygen in-situ has yielded working graphene nonlocal spin valves with different nonlocal resistance signal values ranging from tens of mΩ to tens of Ω. This led us to believe that the formed tunnel barriers did not always yield tunneling effect due to the presence of pinholes. By performing analysis on the nonlocal Hanle measurement results by incorporating the spin sinking effect, the spin transport properties such as the injection/detection efficiency, spin relaxation time, and spin diffusion coefficient were extracted.

We performed electric field dependence study on the spin signal in our graphene nonlocal spin valves by applying external current to produce the electric field. The results showed clear electric field as expected from the theoretical prediction of spin diffusion length suppression/enhancement by electric field. We then proposed an alternative method to produce similar spin signal enhancement/suppression without the external electric field

application by incorporating the double buried-gate structure which consists of two (left and right) local back gates located underneath the left and right halves of the graphene channel into the nonlocal spin valve device. This structure can be used to independently tune the Fermi levels of the two halves of the graphene channel to produce an asymmetry in the doping concentration. The nonlocal resistance values did not exhibit significant change as a function of the different doping concentrations in the two halves of the graphene channel. Interestingly, in one of our devices, we observed a strong dependence of the spin signal as a function of the left gate, but not the right gate. Furthermore, the spin relaxation time dependence on the carrier concentration in the right half of the channel showed clear EY spin scattering mechanism, while the same behavior was not observed in the left half of the channel. This is a strong indication that the spin scattering in graphene is not only different between different devices, but also between two small regions of the same device. The strong local effects could also explain why the spin scattering mechanism in graphene still remains elusive today. Finally, we believe the double-buried gate structure can be useful for example to investigate the spin transport across a p-n junction in graphene.

Graphene spintronics can potentially be useful in the all spin logic (ASL) application. ASL devices require that the information in the form of electron spins travels from the input to the output and not the other way around. Our method by inducing doping asymmetry did not yield strong asymmetry in the nonlocal resistance of our nonlocal spin valves. However, we believe that further investigation of the double buried-gate structures and more theoretical work are still needed to understand the doping asymmetry effects on spin transport in graphene. The magnetization switching by spin transfer torque remains a

challenge in graphene. Fortunately, recent demonstration of perpendicular magnetic anisotropy (PMA) in graphene/cobalt structures could be useful in future graphene spin logic devices to reduce the current needed for magnetization switching. Furthermore, other materials such as phosphorene have emerged that could also have interesting spin properties. The ferromagnet contact to few-layer phosphorene was studied and the gate tuning of the effective Schottky barrier height could enable spin injection into this material.

List of references

1. Clark, W. G. & Feher, G. Nuclear polarization in InSb by a dc current. *Phys. Rev. Lett.* **10**, 134-138 (1963).
2. Aronov, A. G. & Pikus, G. E. Spin injection into semiconductors. *Sov. Phys. - Semicond.* **10,** 698–700 (1976).
3. Meservey, R., Tedrow, P. M. & Fulde, P. Magnetic field splitting of the quasiparticle states in superconducting aluminum films. *Phys. Rev. Lett.* **25**, 1270-1272 (1970).
4. Bardeen, J. Tunneling from a many-particle point of view. *Phys. Rev. Lett.* **6**, 57-59 (1961).
5. Giaever, I. Energy gap in superconductors measured by electron tunneling. *Phys. Rev. Lett.* **5**, 147-148 (1960).
6. Tedrow, P. M. & Meservey, R. Spin-dependent tunneling into ferromagnetic nickel. *Phys. Rev. Lett.* **26**, 192-195 (1971).
7. Tedrow, P. M. & Meservey, R. Spin polarization of electrons tunneling from films of Fe, Co, Ni, and Gd. *Phys. Rev. B* **7**, 318-326 (1973).
8. Johnson, M. & Silsbee, R. H. Interfacial charge-spin coupling: Injection and detection of spin magnetization in metals. *Phys. Rev. Lett.* **55**, 1790-1793 (1985).
9. Johnson, M. & Silsbee, R. H. Thermodynamic analysis of interfacial transport and of the thermomagnetoelectric system. *Phys. Rev. B* **35**, 4959-4972 (1987).
10. Johnson, R. & Silsbee, R. H. Ferromagnet-nonferromagnet interface resistance. *Phys. Rev. Lett.* **60**, 377 (1988).
11. Johnson, M. & Silsbee, R. H. Spin-injection experiment. *Phys. Rev. B* **37**, 5326-5337 (1988).
12. Aronov, A. G. Spin injection in metals and polarization of nuclei. *JETP Lett.* **24**, 32-33 (1976).
13. Julliere, M. Tunneling between ferromagnetic films. *Phys. Lett.* **54A**, 225-226 (1975).
14. Mott, N. F. The electrical conductivity of transition metals. *Proc. Roy. Soc. London Ser. A* **153**, 699-717 (1936).
15. Baibich, M. N., Broto, J. M., Fert, A., Nguyen Van Dau, F. & Petroff, F. Giant magnetoresistance of (001)Fe/(001)Cr magnetic superlattices. *Phys. Rev. Lett.* **61**, 2472-2475 (1988).
16. Binasch, G., Grünbert, P., Saurenbach, F. & Zinn, W. Enhanced magnetoresistance in layered magnetic structures with antiferromagnetic interlayer exchange. *Phys. Rev. B* **39**, 4828-4830 (1989).
17. Slonczewski, J. C. Current-driven excitation of magnetic multilayers. *J. Magn. Magn. Mater.* **159**, L1-L7 (1996).
18. Slonczewski, J. C. Excitation of spin waves by an electric current. *J. Magn. Magn. Mater.* **195**, L261-L268 (1999).
19. Berger, L. Emission of spin waves by a magnetic multilayer traversed by a current. *Phys. Rev. B* **54**, 9353-9358 (1996).

20. Berger, L. Effect of interfaces on Gilbert damping and ferromagnetic resonance linewidth in magnetic multilayers. *J. Appl. Phys.* **90**, 4632-4638 (2001).
21. Tsoi, M., Jansen, A. G. M., Bass, J., Chiang, W.-C., Seck, M., Tsoi, V. & Wyder, P. Excitation of a magnetic multilayer by an electric current. *Phys. Rev. Lett.* **80**, 4281-4284 (1998).
22. Ralph, D. C. & Stiles, M. D. Spin transfer torques. *J. Magn. Magn. Mater.* **320**, 1190-1216 (2008).
23. Behin-Aein, B., Salahuddin, S. & Datta, S. Switching energy of ferromagnetic logic bits. *IEEE Trans. Nanotechnol.* **8**, 505-514 (2009).
24. Sun, J. Z. & Ralph, D. C. Magnetoresistance and spin-transfer torque in magnetic tunnel junctions. *J. Magn. Magn. Mater.* **320**, 1227-1237 (2008).
25. Dyakonov, M. I. & Perel, V. I. Current-induced spin orientation of electrons in semiconductors. *Phys. Lett. A* **35**, 459-460 (1971).
26. Hirsch, J. E. Spin Hall effect. *Phys. Rev. Lett.* **83**, 1834-1837 (1999).
27. Kato, Y. K., Myers, R. C., Gossard, A. C. & Awschalom, D. D. Observation of the spin Hall effect in semiconductors. *Science* **306**, 1910-1913 (2004).
28. Valenzuela, S. O. & Tinkham, M. Direct electronic measurement of the spin Hall effect. *Nature* **442**, 176-179 (2006).
29. Saitoh, E., Ueda, M., Miyajima, H. & Tatara, G. Conversion of spin current into charge current at room temperature: Inverse spin-Hall effect. *Appl. Phys. Lett.* **88**, 182509 (2006).
30. Morota, M., Niimi, Y., Ohnishi, K., Wei, D. H., Tanaka, T., Kontani, H., Kimura, T. & Otani. Y. Indication of intrinsic spin Hall effect in 4d and 5d transition metals. *Phys. Rev. B* **83**, 174405 (2011).
31. Ando, K., Takahashi, S., Ieda, J., Kajiwara, Y., Nakayama, H., Yoshino, T., Harii, K., Fujikawa, Y., Matsuo, M., Maekawa, S. & Saitoh, E. Inverse spin-Hall effect induced by spin pumping in metallic system. *J. Appl. Phys.* **109**, 103913 (2011).
32. Balakrishnan, J., Koon, G. K. W., Avsar, A., Ho, Y., Lee, J. H., Jaiswal, M., Baeck, S.-J., Ahn, J.-A., Ferreira, A., Cazalilla, M. A., Castro Neto, A. H. & Özyilmaz, B. Giant spin Hall effect in graphene grown by chemical vapor deposition. *Nat. Commun.* **5**, 4748 (2014).
33. Žutić, I., Fabian, J. & Sarma, S. Das. Spintronics: Fundamentals and applications. *Rev. Mod. Phys.* **76,** 323–410 (2004).
34. Chappert, C., Fert, A. & Nguyen Van Dau, F. The emergence of spin electronics in data storage. *Nat. Mater.* **6**, 813-823 (2007).
35. Dery, H., Dalal, P., Cywiński, Ł. & Sham, L. J. Spin-based logic in semiconductors for reconfigurable large-scale circuits. *Nature* **447,** 573–576 (2007).
36. Xu, P., Xia, K., Gu, C., Tang, L., Yang, H. & Li, J. An all-metallic logic gate based on current-driven domain wall motion. *Nat. Nanotechnol.* **3**, 97-100 (2008).

37. Behin-Aein, B., Datta, D., Salahuddin, S. & Datta, S. Proposal for an all-spin logic device with built-in memory. *Nat. Nanotechnol.* **5**, 266-270 (2010).
38. Kimura, T., Otani, Y. & Hamrle, J. Switching magnetization of a nanoscale ferromagnetic particle using nonlocal spin injection. *Phys. Rev. Lett.* **96**, 037201 (2006).
39. Yang, T., Kimura, T. & Otani, Y. Giant spin-accumulation signal and pure spin-current-induced reversible magnetization switching. *Nat. Phys.* **4**, 851-854 (2008).
40. Srinivasan, S., Sarkar, A., Behin-Aein, B. and Datta, S. All-spin logic device with inbuilt nonreciprocity. *IEEE Trans. Magn.* **47**, 4026-4032 (2011).
41. Behin-Aein, B., Sarkar, A., Srinivasan, S. & Datta, S. Switching energy-delay of all spin logic devices. *Appl. Phys. Lett.* **98**, 123510 (2011).
42. Lee, O. J., Pribiag, V. S., Braganca, P. M., Gowtham, P. G., Ralph, D. C. & Buhrman, R. A. Ultrafast switching of a nanomagnet by a combined out-of-plane and in-plane polarized spin current pulse. *Appl. Phys. Lett.* **95**, 012506 (2009).
43. Novoselov, K. S., Geim, A. K., Morozov, S. V., Jiang, D., Zhang, Y., Dubonos, S. V., Grigorieva, I. V. & Firsov, A. A. Electric field effect in atomically thin carbon films. *Science* **306**, 666-669 (2004).
44. Slonczewski, J. C. & Weiss, P. R. Band structure of graphite. *Phys. Rev.* **109**, 272-279 (1958).
45. Geim, A. K. & Novoselov, K. S. The rise of graphene. *Nat. Mater.* **6**, 183-191 (2007).
46. Tan, Y. -W., Zhang, Y., Bolotin, K., Zhao, Y., Adam, S., Hwang, E. H., Das Sarma, S., Stormer, H. L. & Kim, P. Measurement of scattering rate and minimum conductivity in graphene. *Phys. Rev. Lett.* **99**, 246803 (2007).
47. Zhang, Y., Tan, Y.-W., Stormer, H. L. & Kim, P. Experimental observation of the quantum Hall effect and Berry's phase in graphene. *Nature* **438**, 201-204 (2005).
48. Abanin, D. A. & Levitov, L. S. Quantized transport in graphene p-n junctions in a magnetic field. *Science* **317**, 641-643 (2007).
49. Williams, J. R., DiCarlo, L. & Marcus, C. M. Quantum Hall effect in a gate-controlled p-n junction of graphene. *Science* **317**, 638-641 (2007).
50. Özyilmaz, B., Jarillo-Herrero, P., Efetov, D., Abanin, D. A., Levitov, L. S. & Kim, P. Electronic transport and quantum Hall effect in bipolar graphene p-n-p junctions. *Phys. Rev. Lett.* **99**, 166804 (2007).
51. Velasco Jr., J., Liu, G., Jing, L., Kratz, P., Zhang, H., Bao, W., Bockrath, M. & Lau, C. N. Probing charging and localization in the quantum Hall regime by graphene p-n-p junctions. *Phys. Rev. B* **81**, 121407(R) (2010).
52. Young, A. F. & Kim, P. Quantum interference and Klein tunneling in graphene heterojunctions. *Nat. Phys.* **5**, 222-226 (2009).
53. Young, A. F., Sanchez-Yamagishi, J. D., Hunt, B., Choi, S. H., Watanabe, K., Taniguchi, T., Ashoori, R. C. & Jarillo-Herrero, P. Tunable symmetry breaking

and helical edge transport in a graphene quantum spin Hall state. *Nature* **505**, 528-532 (2014).
54. Chen, J.-H., Jang, C., Xiao, S., Ishigami, M. & Fuhrer, M. S. Intrinsic and extrinsic performance limits of graphene devices on SiO_2. *Nat. Nanotechnol.* **3**, 206-209 (2008).
55. Chauhan, J. & Guo, J. High-field transport and velocity saturation in graphene. *Appl. Phys. Lett.* **95**, 023120 (2009).
56. Dorgan, V. E., Bae, M.-H. & Pop, E. Mobility and saturation velocity in graphene on SiO_2. *Appl. Phys. Lett.* **97**, 082112 (2010).
57. Berger, C., Song, Z., Li, T., Li, X., Ogbazghi, A. Y., Feng, R., Dai, Z., Marchenkov, A. N., Conrad, E. H., First, P. N. & de Heer, W. A. Ultrathin epitaxial graphite: 2D electron gas properties and a route toward graphene-based nanoelectronics. *J. Phys. Chem. B* **108**, 19912-19916 (2004).
58. Hass, J., Feng, R., Li, T., Li, X., Zong, Z., de Heer, W. A., First, P. N., Conrad, E. H., Jeffrey, C. A. & Berger, C. Highly ordered graphene for two dimensional electronics. *Appl. Phys. Lett.* **89**, 143106 (2006).
59. Lemme, M. C., Echtermeyer, T. J., Baus, M. & Kurz, H. A graphene field-effect device. *IEEE Electron Device Lett.* **28**, 282-284 (2007).
60. Thiele, S. A., Schaefer, J. A. & Schwierz, F. Modeling of graphene metal-oxide-semiconductor field-effect transistors with gapless large-area graphene channels. *J. Appl. Phys.* **107**, 094505 (2010).
61. Schwierz, F. Graphene transistors. *Nat. Nanotechnol.* **5**, 487-496 (2010).
62. Kim, B. J., Jang, H., Lee, S.-K., Hong, B. H., Ahn, J.-H. & Cho, J. H. High-performance flexible graphene field effect transistors with ion gel gate dielectrics. *Nano Lett.* **10**, 3464-3466 (2010).
63. Kim, K., Choi, J.-Y., Kim, T., Cho, S.-H. & Chung, H.-J. A role for graphene in silicon-based semiconductor devices. *Nature* **479**, 338-344 (2011).
64. Liao, L., Bai, J., Qu, Y., Huang, Y. & Duan, X. Single-layer graphene on Al_2O_3/Si substrate: better contrast and higher performance of graphene transistors. *Nanotechnology* **21**, 015705 (2010).
65. Lee, S.-K., Kim, B. J., Jang, H., Yoon, S. C., Lee, C., Hong, B. H., Rogers, J. A., Cho, J. H. & Ahn, J.-H. Stretchable graphene transistors with printed dielectric and gate electrodes. *Nano Lett.* **11**, 4642-4646 (2011).
66. Champlain, J. G. A first principles theoretical examination of graphene-based field effect transistors. *J. Appl. Phys.* **109**, 084515 (2011).
67. Nayfeh, O. M. Radio-frequency transistors using chemical-vapor-deposited monolayer graphene: performance, doping, and transport effects. *IEEE Trans. Electron Devices* **58**, 2847-2853 (2011).
68. Black, C. T., Ruiz, R., Breyta, G., Cheng, J. Y., Colburn, M. E., Guarini, K. W., Kim, H.-C. & Zhang, Y. Polymer self assembly in semiconductor microelectronics. *IBM J. Res. & Dev.* **51**, 605-633 (2007).
69. Liu, G., Velasco Jr., J., Bao, W. & Lau, C. N. Fabrication of graphene p-n-p junctions with contactless top gates. *Appl. Phys. Lett.* **92**, 203103 (2008).

70. Datta, S. S., Strachan, D. R., Khamis, S. M. & Charlie Johnson, A. T. Crystallographic etching of few-layer graphene. *Nano Lett.* **8**, 1912-1915 (2008).
71. Lemme, M. C., Bell, D. C., Williams, J. R., Stern, L. A., Baugher, B. W. H., Jarillo-Herrero, P. & Marcus, C. M. Etching of graphene devices with a helium ion beam. *ACS Nano* **3**, 2674-2676 (2009).
72. Bai, J., Zhong, X., Jiang, S., Huang, Y. & Duan, X. Graphene nanomesh. *Nat. Nanotechnol.* **5**, 190-194 (2010).
73. Li, X., Cai, W., An, J., Kim, S., Nah, J., Yang, D., Piner, R., Velamakanni, A., Jung, I., Tutuc, E., Banerjee, S. K., Colombo, L. & Ruoff, R. S. Large-area synthesis of high-quality and uniform graphene films on copper foils. *Science* **324**, 1312-1314 (2009).
74. Reina, A., Thiele, S., Jia, X., Bhaviripudi, S., Dresselhaus, M. S., Schaefer, J. A. & Kong, J. Growth of large-area single- and bi-layer graphene by controlled carbon precipitation on polycrystalline Ni surfaces. *Nano Res.* **2**, 509-516 (2009).
75. Amini, S., Garay, J., Liu, G., Balandin, A. A. & Abbaschian, R. Growth of large-area graphene films from metal-carbon melts. *J. Appl. Phys.* **108**, 094321 (2010).
76. Yang, W., Chen, G., Shi, Z., Liu, C.-C., Zhang, L., Xie, G., Cheng, M., Wang, D., Yang, R., Shi, D., Watanabe, K., Taniguchi, T., Yao, Y., Zhang, Y. & Zhang, G. Epitaxial growth of single-domain graphene on hexagonal boron nitride. *Nat. Mater.* **12**, 792-797 (2013).
77. Bachmatiuk, A., Boeckl, J., Smith, H., Ibrahim, I., Gemming, T., Oswald, S., Kazmierczak, W., Makarov, D., Schmidt, O. G., Eckert, J., Fu, L. & Rummel, M. H. Vertical graphene growth from amorphous carbon films using oxidizing gases. *J. Phys. Chem. C* **119**, 17965-17970 (2015).
78. Wu, T., Zhang, X., Yuan, Q., Xue, J., Lu, G., Liu, Z., Wang, H., Wang, H., Ding, F., Yu, Q., Xie, X. & Jiang, M. Fast growth of inch-sized single-crystalline graphene from a controlled single nucleus on Cu-Ni alloys. *Nat. Mater.* **15**, 43-47 (2016).
79. Leenaerts, O., Partoens, B. & Peeters, F. M. Adsorption of H_2O, NH_3, CO, NO_2, and NO on graphene: A first-principles study. *Phys. Rev. B* **77**, 125416 (2008).
80. Wehling, T. O., Lichtenstein, A. I. & Katsnelson, M. I. First-principles studies of water adsorption on graphene: The role of the substrate. *Appl. Phys. Lett.* **93**, 202110 (2008).
81. Wehling, T. O., Katsnelson, M. I. & Lichtenstein, A. I. Adsorbates on graphene: Impurity states and electron scattering. *Chem. Phys. Lett.* **476**, 125-134 (2009).
82. Wang, H., Wu, Y., Cong, C., Shang, J. & Yu, T. Hysteresis of electronic transport in graphene transistors. *ACS Nano* **4**, 7221-7228 (2010).
83. Brenner, K. & Murali, R. Single step, complementary doping of graphene. *Appl. Phys. Lett.* **96**, 063104 (2010).

84. Guo, B., Liu, Q., Chen, E., Zhu, H., Fang, L. & Gong, J. R. Controllable n-doping of graphene. *Nano Lett.* **10**, 4975-4980 (2010).
85. Huh, S., Park, J., Kim, K. S., Hong, B. H. & Kim, S. B. Selective n-type doping of graphene by photo-patterned gold nanoparticles. *ACS Nano* **5**, 3639-3644 (2011).
86. Xiang, D., Han, C., Wu, J., Zhong, S., Liu, Y., Lin, J., Zhang, X.-A., Hu, W. P, Özyilmaz, B., Castro Neto, A. H., Wee, A. T. S. & Chen, W. Surface transfer doping induced effective modulation on ambipolar characteristics of few-layer black phosphorus. *Nat. Commun.* **6**, 6485 (2015).
87. Lafkioti, M., Krauss, B., Lohmann, T., Zschieschang, U., Klauk, H., Klitzing, K. v. & Smet, J. H. Graphene on a hydrophobic substrate: Doping reduction and hysteresis suppression under ambient conditions. *Nano Lett.* **10**, 1149-1153 (2010).
88. Joshi, P., Romero, H. E., Neal, A. T., Toutam, V. K. & Tadigadapa, S. A. Intrinsic doping and gate hysteresis in graphene field effect devices fabricated on SiO_2 substrates. *J. Phys.: Condens. Matter* **22**, 334214 (2010).
89. Pirkle, A., Chan, J., Venugopal, A., Hinojos, D., Magnuson, C. W., McDonnell, S., Colombo, L., Vogel, E. M., Ruoff, R. S. & Wallace, R. M. The effect of chemical residues on the physical and electrical properties of chemical vapor deposited graphene transferred on SiO_2. *Appl. Phys. Lett.* **99**, 122108 (2011).
90. Huard, B., Sulpizio, J. A., Stander, N., Todd, K., Yang, B. & Goldhaber-Gordon, D. Transport measurements across a tunable potential barrier in graphene. *Phys. Rev. Lett.* **98**, 236803 (2007).
91. Huard, B., Stander, N., Sulpizio, J. A. & Goldhaber-Gordon, D. Evidence of the role of contacts on the observed electron-hole asymmetry in graphene. *Phys. Rev. B* **78**, 121402(R) (2008).
92. Lee, E. J. H., Balasubramanian, K., Weitz, R. T., Burghard, M. & Kern, K. Contact and edge effects in graphene devices. *Nat. Nanotechnol.* **3**, 486-490 (2008).
93. Robinson, J. A., LaBella, M., Zhu, M., Hollander, M., Kasarda, R., Hughes, Z., Trumbull, K., Cavalero, R. & Snyder, D. Contacting graphene. *Appl. Phys. Lett.* **98**, 053103 (2011).
94. Xia, F., Perebeinos, V., Lin, Y.-m., Wu, Y. & Avouris, P. The origins and limits of metal-graphene junction resistance. *Nat. Nanotechnol.* **6**, 179-184 (2011).
95. Cheng, Z., Zhou, Q., Wang, C., Li, Q., Wang, C. & Fang, Y. Toward intrinsic graphene surfaces: A systematic study on thermal annealing and wet-chemical treatment of SiO_2-supported graphene devices. *Nano Lett.* **11**, 767-771 (2011).
96. Movva, H. C. P., Ramón, M. E., Corbet, C. M., Sonde, S., Chowdhury, Sk. F., Carpenter, G., Tutuc, E. & Banerjee, S. K. Self-aligned graphene field-effect transistors with polyethyleneimine doped source/drain access regions. *Appl. Phys. Lett.* **101**, 183113 (2012).

97. Suk, J. W., Lee, W. H., Lee, J., Chou, H., Piner, R. D., Hao, Y., Akinwande, D. & Ruoff, R. S. Enhancement of the electrical properties of graphene grown by chemical vapor deposition via controlling the effects of polymer residue. *Nano Lett.* **13**, 1462-1467 (2013).
98. Hsu, A., Wang, H., Kim, K. K., Kong, J. & Palacios, T. Impact of graphene interface quality on contact resistance and RF device performance. *IEEE Electron Device Lett.* **32**, 1008-1010 (2011).
99. Kuzmenko, A. B., van Heumen, E., Carbone, F. & van der Marel, D. Universal optical conductance of graphite. *Phys. Rev. Lett.* **100**, 117401 (2008).
100. Falkovsky, L. A. Optical properties of graphene. *J. Phys. Conf. Ser.* **129**, 012004 (2008).
101. Yang, L., Deslippe, J., Park, C.-H., Cohen, M. L. & Louie, S. G. Excitonic effects on the optical response of graphene and bilayer graphene. *Phys. Rev. Lett.* **103**, 186802 (2009).
102. Xia, F., Mueller, T., Lin, Y.-m., Valdes-Garcia, A. & Avouris, P. Ultrafast graphene photodetectors. *Nat. Nanotechnol.* **4**, 839-843 (2009).
103. Bonaccorso, F., Sun, Z., Hasan, T. & Ferrari, A. C. Graphene photonics and optoelectronics. *Nat. Photonics* **4**, 611-622 (2010).
104. Liu, M., Yin, X., Ulin-Avila, E., Geng, B., Zentgraf, T., Ju, L., Wang, F. & Zhang, X. A graphene-based broadband optical modulator. *Nature* **474**, 64-67 (2011).
105. Liu, M., Yin, X. & Zhang, X. Double-layer graphene optical modulator. *Nano Lett.* **12**, 1482-1485 (2012).
106. Yang, Y.-E., Yang, Y.-R. & Yan, X.-H. Universal optical properties of graphene nanoribbons: A first-principles study. Physica E **44**, 1406-1409 (2012).
107. Youngblood, N., Anugrah, Y., Ma, R., Koester, S. J. & Li, M. Multifunctional graphene optical modulator and photodetector integrated on silicon waveguides. *Nano Lett.* **14**, 2741-2746 (2014).
108. Fang, T., Konar, A., Xing, H. & Jena, D. Carrier statistics and quantum capacitance of graphene sheets and ribbons. *Appl. Phys. Lett.* **91**, 092109 (2007).
109. Koester, S. J. High quality factor graphene varactors for wireless sensing applications. *Appl. Phys. Lett.* **99**, 163105 (2011).
110. Ebrish, M. A., Shao, H. & Koester, S. J. Operation of multi-finger graphene quantum capacitance varactors using planarized local bottom gate electrodes. *Appl. Phys. Lett.* **100**, 143102 (2012).
111. Cohen-Tanugi, D. & Grossman, J. C. Water desalination across nanoporous graphene. *Nano Lett.* **12**, 3602-3608 (2012).
112. Hill, E. W., Geim, A. K., Novoselov, K., Schedin, F. & Blake, P. Graphene spin valve devices. *IEEE Trans. Magn.* **42**, 2694-2696 (2006).
113. Tombros, N., Józsa, C., Popinciuc, M., Jonkman, H. T. & van Wees, B. J. Electronic spin transport and spin precession in single graphene layers at room temperature. *Nature Lett.* **448**, 571-575 (2007).

114. Nam Do, V., Hung Nguyen, V., Dollfus, P. & Bournel, A. Electronic transport and spin-polarization effects of relativisticlike particles in mesoscopic graphene structures. *J. Appl. Phys.* **104**, 063708 (2008).
115. Huertas-Hernando, D., Guinea, F. & Brataas, A. Spin-orbit-mediated spin relaxation in graphene. *Phys. Rev. Lett.* **103**, 146801 (2009).
116. Konschuh, S., Gmitra, M. & Fabian, J. Tight-binding theory of the spin-orbit coupling in graphene. *Phys. Rev. B* **82**, 245412 (2010).
117. Ghosh, B. & Misra, S. Monte Carlo simulation study of spin transport in single layer graphene. *J. Appl. Phys.* **110**, 043711 (2011).
118. Ochoa, H., Castro Neto, A. H. & Guinea, F. Elliot-Yafet mechanism in graphene. *Phys. Rev. Lett.* **108**, 206808 (2012).
119. Fedorov, D. V., Gradhand, M., Ostanin, S., Maznichenko, I. V., Ernst, A., Fabian, J. & Mertig, I. Impact of electron-impurity scattering on the spin relaxation time in graphene: A first-principles study. *Phys. Rev. Lett.* **110**, 156602 (2013).
120. Lu, W.-T., Li, W., Wang, Y.-L., Jiang, H. & Xu, C.-T. Tunable wavevector and spin filtering in graphene induced by resonant tunneling. *Appl. Phys. Lett.* **103**, 062108 (2013).
121. Salimath, A. & Ghosh, B. Effect of temperature, electric and magnetic field on spin relaxation in bilayer graphene. *J. Comput. Electron.* **12**, 448-453 (2013).
122. Dyrdał, A. & Barnas, J. Current-induced spin polarization and spin-orbit torque in graphene. *Phys. Rev. B* **92**, 165404 (2015).
123. Yu, Z. G., Baker, J. & Krishnamurthy, S. Transfer lengths and spin injection from a three-dimensional ferromagnet into graphene. *Phys. Rev. B* **82**, 035425 (2010).
124. Zeng, M., Shen, L., Su, H., Zhang, C. & Feng, Y. Graphene-based spin logic gates. *Appl. Phys. Lett.* **98**, 092110 (2011).
125. Liu, F., Liu, Y., Smith, D. L. & Ruden, P. P. Device model for graphene spin valves. *IEEE Trans. Electron Devices* **62**, 3426-3432 (2015).
126. Cho, S., Chen, Y.-F. & Fuhrer, M. S. Gate-tunable graphene spin valve. *Appl. Phys. Lett.* **91**, 123105 (2007).
127. Goto, H., Kanda, A., Sato, T., Tanaka, S., Ootuka, Y., Odaka, S., Miyazaki, H., Tsukagoshi, K. & Aoyagi, Y. Gate control of spin transport in multilayer graphene. *Appl. Phys. Lett.* **92**, 212110 (2008).
128. Józsa, C., Popinciuc, M., Tombros, N., Jonkman, H. T. & van Wees, B. J. Electronic spin drift in graphene field-effect transistors. *Phys. Rev. Lett.* **100**, 236603 (2008).
129. Wang, W. H., Han, W., Pi, K., McCreary, K. M., Miao, F., Bao, W., Lau, C. N. & Kawakami, R. K. Growth of atomically smooth MgO films on graphene by molecular beam epitaxy. *Appl. Phys. Lett.* **93**, 183107 (2008).
130. Han, W., Pi, K., Bao, W., McCreary, K. M., Li, Y., Wang, W. H., Lau, C. N. & Kawakami, R. K. Electrical detection of spin precession in single layer graphene with transparent contacts. *Appl. Phys. Lett.* **94**, 222109 (2009).

131. Han, W., Wang, W. H., Pi, K., McCreary, K. M., Bao, W., Li, Yan., Miao, F., Lau, C. N. & Kawakami, R. K. Electron-hole asymmetry of spin injection and transport in single-layer graphene. *Phys. Rev. Lett.* **102**, 137205 (2009).
132. Józsa, C., Popinciuc, M., Tombros, N., Jonkman, H. T. & van Wees, B. J. Controlling the efficiency of spin injection into graphene by carrier drift. *Phys. Rev. B* **79**, 081402(R) (2009).
133. Popinciuc, M., Józsa, C., Zomer, P. J., Tombros, N., Veligura, A., Jonkman, H. T. & van Wees, B. J. Electronic spin transport in graphene field-effect transistors. *Phys. Rev. B* **80**, 214427 (2009).
134. Han, W., Pi, K., McCreary, K. M., Li, Y., Wong, J. J. I., Swartz, A. G. & Kawakami, R. K. Tunneling spin injection into single layer graphene. *Phys. Rev. Lett*. **105**, 167202 (2010).
135. Han, W. & Kawakami, R. K. Spin relaxation in single-layer and bilayer graphene. *Phys. Rev. Lett.* **107**, 047207 (2011).
136. Yang, T.-Y., Balakrishnan, J., Volmer, F., Avsar, A., Jaiswal, M., Samm, J., Ali, S. R., Pachoud, A., Zeng, M., Popinciuc, M., Güntherodt, G., Beschoten, B. & Özyilmaz, B. Observation of long spin-relaxation times in bilayer graphene at room temperature. *Phys. Rev. Lett.* **107**, 047206 (2011).
137. Dlubak, B., Martin, M.-B., Deranlot, C., Bouzehouane, K., Fusil, S., Mattana, R., Petroff, F., Anane, A., Seneor, P. & Fert, A. Homogeneous pinhole free 1nm Al_2O_3 tunnel barriers on graphene. *Appl. Phys. Lett.* **101**, 203104 (2012).
138. Han, W., Chen, J.-R., Wang, D., McCreary, K. M., Wen, H., Swartz, A. G., Shi, J. & Kawakami, R. K. Spin relaxation in single-layer graphene with tunable mobility. *Nano Lett.* **12**, 3443-3447 (2012).
139. Han, W., McCreary, K. M., Pi, K., Wang, W. H., Li, Y., Wen, H., Chen, J.-R. & Kawakami, R. K. Spin transport and relaxation in graphene. *J. Magn. Magn. Mater.* **324**, 369-381 (2012).
140. Guimarães, M. H. D., Veligura, A., Zomer, P. J., Maassen, T., Vera-Marun, I. J., Tombros, N. & van Wees, B. J. Spin transport in high-quality suspended graphene devices. *Nano Lett.* **12**, 3512-3517 (2012).
141. Yamaguchi, T., Masubuchi, S., Iguchi, K., Moriya, R. & Machida, T. Tunnel spin injection into graphene using Al_2O_3 barrier grown by atomic layer deposition on functionalized graphene surface. *J. Magn. Magn. Mater.* **324**, 849-852 (2012).
142. Zomer, P. J., Guimarães, M. H. D., Tombros, N. & van Wees, B. J. Long-distance spin transport in high-mobility graphene on hexagonal boron nitride. *Phys. Rev. B* **86**, 161416(R) (2012).
143. Vera-Marun, I. J., Ranjan, V. & van Wees, B. J. Nonlinear detection of spin currents in graphene with non-magnetic electrodes. *Nat. Phys.* **8**, 313-316 (2012).
144. Cobas, E., Friedman, A. L., van't Erve, O. M. J., Robinson, J. T. & Jonker, B. T. Graphene-based magnetic tunnel junctions. *IEEE Trans. Magn.* **49**, 4343-4346 (2013).

145. Iqbal, M. Z., Iqbal, M. W., Lee, J. H., Kim, Y. S., Chun, S.-H. & Eom, J. Spin valve effect of NiFe/graphene/NiFe junctions. *Nano Res.* **6**, 373-380 (2013).
146. Konishi, K., Cui, Z., Hiraki, T. & Yoh, K. Spin-injection into epitaxial graphene on silicon carbide. *J. Cryst. Growth* **378**, 385-387 (2013).
147. Neumann, I., Costache, M. V., Bridoux, G., Sierra, J. F. & Valenzuela, S. O. Enhanced spin accumulation at room temperature in graphene spin valves with amorphous carbon interfacial layers. *Appl. Phys. Lett.* **103**, 112401 (2013).
148. Tang, Z., Shikoh, E., Ago, H., Kawahara, K., Ando, Y., Shinjo, T. & Shiraishi, M. Dynamically generated pure spin current in single-layer graphene. *Phys. Rev. B* **87**, 140401(R) (2013).
149. Guimarães, M. H. D., Zomer, P. J., Ingla-Aynés, J., Brant, J. C., Tombros, N. & van Wees, B. J. Controlling spin relaxation in hexagonal BN-encapsulated graphene with a transverse electric field. *Phys. Rev. Lett.* **113**, 086602 (2014).
150. Kamalakar, M. V., Dankert, A., Bergsten, J., Ive, T. & Dash, S. P. Enhanced tunnel spin injection into graphene using chemical vapor deposited hexagonal boron nitride. *Sci. Rep.* **4**, 6146 (2014).
151. Park, J. H. & Lee, H. J. Out-of-plane magnetoresistance in ferromagnet/graphene/ferromagnet spin valve junctions. *Phys. Rev. B* **89**, 165417 (2014).
152. Volmer, F., Drögeler, M., Maynicke, E., von den Driesch, N., Boschen, M. L., Güntherodt, G., Stampfer, C. & Beschoten, B. Suppression of contact-induced spin dephasing in graphene/MgO/Co spin-valve devices by successive oxygen treatments. *Phys. Rev. B* **90**, 165403 (2014).
153. Cubukcu, M., Martin, M.-B., Laczkowski, P., Vergnaud, C., Marty, A., Attané, J.-P., Seneor, P., Anane, A., Deranlot, C., Fert, A., Auffret, S., Ducruet, C., Notin, L., Vila, L. & Jamet, M. Ferromagnetic tunnel contacts to graphene: Contact resistance and spin signal. *J. Appl. Phys.* **117**, 083909 (2015).
154. Kamalakar, M. V., Groenveld, C., Dankert, A. & Dash, S. P. Long distance spin communication in chemical vapor deposited graphene. *Nat. Commun.* **6**, 6766 (2015).
155. Canto, B., Gouvea, C. P., Archanjo, B. S., Schmidt, J. E. & Baptista, D. L. On the structural and chemical characteristics of Co/Al_2O_3/graphene interfaces for graphene spintronic devices. *Sci. Rep.* **5**, 14332 (2015).
156. Balakrishnan, J., Koon, G. K. W., Jaiswal, M., Castro Netro, A. H. & Özyilmaz, B. Colossal enhancement of spin-orbit coupling in weakly hydrogenated graphene. *Nat. Phys.* **9**, 284-287 (2013).
157. Lin, C.-C., Penumatcha, A. V., Gao, Y., Diep, V. Q., Appenzeller, J. & Chen, Z. Spin transfer torque in a graphene lateral spin valve assisted by an external magnetic field. *Nano Lett.* **13**, 5177-5181 (2013).
158. Lin, C.-C., Gao, Y., Penumatcha, A. V., Diep, V. Q. Appenzeller, J. & Chen, Z. Improvement of spin transfer torque in asymmetric graphene devices. *ACS Nano* **8**, 3807-3812 (2014).
159. Datta, S. & Das, B. Electronic analog of the electro-optic modulator. *Appl. Phys. Lett.* **56**, 665 (1990).

160. Rashba, E. I. Theory of electrical spin injection: Tunnel contacts as a solution of the conductivity mismatch problem. *Phys. Rev. B* **62**, R16267-R16270 (2000).
161. Jedema, F. J., Filip, A. T. & van Wees, B. J. Electrical spin injection and accumulation at room temperature in an all-metal mesoscopic spin valve. *Nature* **410**, 345-348 (2001).
162. Jia, Y. Q., Shi, R. C. & Chou, S. Y. Spin-valve effects in Nickel/Silicon/Nickel junctions. *IEEE Trans. Magn.* **32**, 4707-4709 (1996).
163. Hammar, P. R., Bennett, B. R., Yang, M. J. & Johnson, M. Observation of spin injection at a ferromagnet-semiconductor interface. *Phys. Rev. Lett.* **83**, 203-206 (1999).
164. Monzon, F. G., Johnson, M. & Roukes, M. L. Strong Hall voltage modulation in hybrid ferromagnet/semiconductor microstructures. *Appl. Phys. Lett.* **71**, 3087 (1997).
165. Schmidt, G., Ferrand, D., Molenkamp, L. W., Filip, A. T. & van Wees, B. J. Fundamental obstacle for electrical spin injection from a ferromagnetic metal into a diffusive semiconductor. *Phys. Rev. B* **62**, R4790-R4793 (2000).
166. van Son, P. J., van Kempen, H. & Wyder, P. Boundary resistance of the ferromagnetic-nonferromagnetic metal interface. *Phys. Rev. Lett.* **58**, 2271-2273 (1987).
167. Smith, D. L. & Silver, R. N. Electrical spin injection into semiconductors. *Phys. Rev. B* **64**, 045323 (2001).
168. Qi, Y., Xing, D. Y. & Dong, J. Relation between Julliere and Slonczewski models of tunneling magnetoresistance. *Phys. Rev. B* **58**, 2783 (1998).
169. Li, D. L., Ma, Q. L., Wang, S. G., Ward, R. C. C., Hesjedal, T., Zhang, X.-G., Kohn, A., Amsellem, E., Yang, G., Liu, J. L., Jiang, J., Wei, H. X. & Han, X. F. Controlling spin-dependent tunneling by bandgap tuning in epitaxial rocksalt MgZnO films. *Sci. Rep.* **4**, 7277 (2014).
170. Zhou, Y., Ogawa, M., Bao, M., Han, W., Kawakami, R. K. & Wang, K. L. Engineering of tunnel junctions for prospective spin injection in germanium. *Appl. Phys. Lett.* **94**, 242104 (2009).
171. Smith, D. L. & Ruden, P. P. Spin-polarized tunneling through potential barriers at ferromagnetic metal/semiconductor Schottky contacts. *Phys. Rev. B* **78**, 125202 (2008).
172. Hanbicki, A. T., Jonker, B. T., Itskos, G., Kioseoglou, G. & Petrou, A. Efficient electrical spin injection from a magnetic metal/tunnel barrier contact into a semiconductor. *Appl. Phys. Lett.* **80**, 1240-1242 (2002).
173. Jonker, B. T., Kioseoglou, G., Hanbicki, A. T., Li, C. H. & Thompson, P. E. Electrical spin-injection into silicon from a ferromagnetic metal/tunnel barrier contact. *Nat. Phys.* **3**, 542-546 (2007).
174. Lou, X., Adelmann, C., Crooker, S. A., Garlid, E. S., Zhang, J., Madhukar Reddy, K. S., Flexner, S. D., Palmstrøm, C. J. & Crowell, P. A. Electrical detection of spin transport in lateral ferromagnet-semiconductor devices. *Nature Phys.* **3**, 197-202 (2007).

175. Crooker, S. A., Garlid, E. S., Chantis, A. N., Smith, D. L., Reddy, K. S. M., Hu, Q. O., Kondo, T., Palmstrøm, C. J. & Crowell, P. A. Bias-controlled sensitivity of ferromagnet/semiconductor electrical spin detectors. *Phys. Rev. B* **80**, 041305(R) (2009).
176. Han, W., Kawakami, R. K., Gmitra, M. & Fabian, J. Graphene spintronics. *Nat. Nanotechnol.* **9**, 794-807 (2014).
177. Johnson, M. & Silsbee, R. H. Calculation of nonlocal baseline resistance in a quasi-one-dimensional wire. *Phys. Rev. B* **76**, 153107 (2007).
178. Bakker, F. L., Slachter, A., Adam, J.-P. & van Wees, B. J. Interplay of Peltier and Seebeck effects in nanoscale nonlocal spin valves. *Phys. Rev. Lett.* **105**, 136601 (2010).
179. Kane, C. L. & Mele, E. J. Quantum spin Hall effect in graphene. *Phys. Rev. Lett.* **95**, 226801 (2005).
180. Min, H., Hill, J. E., Sinitsyn, N. A., Sahu, B. R., Kleinman, L. & MacDonald, A. H. Intrinsic and Rashba spin-orbit interactions in graphene sheets. *Phys. Rev. B* **74**, 165310 (2006).
181. Huertas-Hernando, D., Guinea, F. & Brataas, A. Spin-orbit coupling in curved graphene, fullerenes, nanotubes, and nanotube caps. *Phys. Rev. B* **74**, 155426 (2006).
182. Yao, Y., Ye, F., Qi, X.-L., Zhang, S.-C. & Fang, Z. Spin-orbit gap of graphene: First-principles calculations. *Phys. Rev. B* **75**, 041401(R) (2007).
183. Gmitra, M., Konschuh, S., Ertler, C., Ambrosch-Draxl, C. & Fabian, J. Band-structure topologies of graphene: Spin-orbit coupling effects from first principles. *Phys. Rev. B* **80** 235431 (2009).
184. Boettger, J. C. & Trickey, S. B. First-principles calculation of the spin-orbit splitting in graphene. *Phys. Rev. B* **75**, 121402(R) (2007).
185. Lundeberg, M. B., Yang, R., Renard, J. & Folk, J. A. Defect-mediated spin relaxation and dephasing in graphene. *Phys. Rev. Lett.* **110**, 156601 (2013).
186. Kochan, D., Gmitra, M. & Fabian, J. Spin relaxation mechanism in graphene: Resonant scattering by magnetic impurities. *Phys. Rev. Lett.* **112**, 116602 (2014).
187. Castro Neto, A. H. & Guinea, F. Impurity-induced spin-orbit coupling in graphene. *Phys. Rev. Lett.* **103**, 026804 (2009).
188. Pi, K., Han, W., McCreary, K. M., Swartz, A. G., Li, Y. & Kawakami, R. K. Manipulation of spin transport in graphene by surface chemical doping. *Phys. Rev. Lett.* **104**, 187201 (2010).
189. Blake, P., Hill, E. W., Castro Neto, A. H., Novoselov, K. S., Jiang, D., Yang, R., Booth, T. J. & Geim, A. K. Making graphene visible. *Appl. Phys. Lett.* **91**, 063124 (2007).
190. Kim, K. S., Zhao, Y., Jang, H., Lee, S. Y., Kim, J. M., Kim, K. S., Ahn, J.-H., Kim, P., Choi, J.-Y. & Hong, B. H. Large-scale pattern growth of graphene films for stretchable transparent electrodes. *Nature* **457**, 706-710 (2009).
191. Luo, Z., Lu, Y., Singer, D. W., Berck, M. E., Somers, L. A., Goldsmith, B. R. & Charlie Johnson, A. T. Effect of substrate roughness and feedstock

concentration on growth of wafer-scale graphene at atmospheric pressure. *Chem. Mater.* **23**, 1441-1447 (2011).
192. Her, M., Beams, R. & Novotny, L. Graphene transfer with reduced residue. *Phys. Lett. A* **377**, 1455-1458 (2013).
193. Lin, W.-H., Chen, T.-H., Chang, J.-K., Taur, J.-I., Lo, Y.-Y., Lee, W.-L., Chang, C.-S., Su, W.-B. & Wu, C.-I. A direct and polymer-free method for transferring graphene grown by chemical vapor deposition to any substrate. *ACS Nano* **8**, 1784-1791 (2014).
194. Ferrari, A. C., Meyer, J. C., Scardaci, V., Casiraghi, C., Lazzeri, M., Mauri, F., Piscanec, S., Jiang, D., Novoselov, K. S., Roth, S. & Geim, A. K. Raman spectrum of graphene and graphene layers. *Phys. Rev. Lett.* **97**, 187401 (2006).
195. Hao, Y., Wang, Y., Wang, L., Ni, Z., Wang, Z., Wang, R., Koo, C. K., Shen, Z. & Thong, J. T. L. Probing layer number and stacking order of few-layer graphene by Raman spectroscopy. *Small* **6**, 195-200 (2010).
196. Graf, D., Molitor, F., Ensslin, K., Stampfer, C., Jungen, A., Hierold, C. & Wirtz, L. Spatially resolved Raman spectroscopy of single- and few-layer graphene. *Nano Lett.* **7**, 238-242 (2007).
197. Frank, D. J., Taur, Y. & Wong, H.-S. P. Generalized scale length for two-dimensional effects in MOSFET's. *IEEE Electron Device Lett.* **19**, 385-387 (1998).
198. Aberg, I. & Hoyt, J. L. Hole transport in UTB MOSFETs in strained-Si directly on insulator with strained-Si thickness less than 5 nm. *IEEE Electron Device Lett.* **26**, 661-663 (2005).
199. Wu, Y., Jenkins, K. A., Valdes-Garcia, A., Farmer, D. B., Zhu, Y., Bol, A. A., Dimitrakopoulos, C., Zhu, W., Xia, F., Avouris, P. & Lin, Y.-M. State-of-the-art graphene high-frequency electronics. *Nano Lett.* **12**, 3062-3067 (2012).
200. Wu, Y., Farmer, D. B., Xia, F. & Avouris, P. Graphene electronics: Materials, devices, and circuits. *Proc. IEEE* **101**, 1620-1637 (2013).
201. Song, S. M., Park, J. K., Sul, O. J. & Cho, B. J. Determination of work function of graphene under a metal electrode and its role in contact resistance. *Nano Lett.* **12**, 3887-3892 (2012).
202. Giovannetti, G., Khomyakov, P. A., Brocks, G., Karpan, V. M., van den Brink, J. & Kelly, P. J. Doping graphene with metal contacts. *Phys. Rev. Lett.* **101**, 026803 (2008).
203. Zebrev, G. I. *Graphene Field Effect Transistors: Diffusion-Drift Theory, Physics and Applications of Graphene - Theory*. (InTech, 2011). doi:10.5772/1938
204. Moser, J., Verdaguer, A., Jiménez, D., Barreiro, A. & Bachtold, A. The environment of graphene probed by electrostatic force microscopy. *Appl. Phys. Lett.* **92**, 123507 (2008).
205. Ishigami, M., Chen, J. H., Cullen, W. G., Fuhrer, M. S. & Williams, E. D. Atomic structure of graphene on SiO_2. *Nano Lett.* **7**, 1643-1648 (2007).

206. Maassen, T., Vera-Marun, I. J., Guimarães, M. H. D. & van Wees, B. J. Contact-induced spin relaxation in Hanle spin precession measurements. *Phys. Rev. B* **86**, 235408 (2012).
207. Takahashi, S. & Maekawa, S. Spin injection and detection in magnetic nanostructures. *Phys. Rev. B* **67**, 052409 (2003).
208. Idzuchi, H., Fukuma, Y., Takahashi, S., Maekawa, S. & Otani, Y. Effect of anisotropic spin absorption on the Hanle effect in lateral spin valves. *Phys. Rev. B* **89**, 081308(R) (2014).
209. Volmer, F., Drögeler, M., Maynicke, E., von den Driesch, N., Boschen, M. L., Güntherodt, G. & Beschoten, B. Role of MgO barriers for spin and charge transport in Co/MgO/graphene nonlocal spin-valve devices. *Phys. Rev. B* **88**, 161405(R) (2013).
210. Maassen, T., Dejene, F. K., Guimarães, M. H. D., Józsa, C. & van Wees, B. J. Comparison between charge and spin transport in few-layer graphene. *Phys. Rev. B* **83**, 115410 (2011).
211. Yu, Z. G. & Flatté, M. E. Electric-field dependent spin diffusion and spin injection into semiconductors. *Phys. Rev. B* **66**, 201202(R) (2002).
212. Yu, Z. G. & Flatté, M. E. Spin diffusion and injection in semiconductor structures: Electric field effects. *Phys. Rev. B* **66**, 245302 (2002).
213. Kim, J., Paul, A., Crowell, P. A., Koester, S. J., Sapatnekar, S. S., Wang, J.-P. & Kim, C. H. Spin-based computing: Device concepts, current status, and a case study on a high-performance microprocessor. *Proc. IEEE* **103**, 106-130 (2015).
214. Yang, H., Vu, A. D., Hallal, A., Rougemaille, N., Coraux, J., Chen, G., Schmid, A. K. & Chshiev, M. Anatomy and giant enhancement of the perpendicular magnetic anisotropy of cobalt-graphene heterostructures. *Nano Lett.* **16**, 145-151 (2016).
215. Li, L., Yu, Y., Ye, G. J., Ge, Q., Ou, X., Wu, H., Feng, D., Chen, X. H. & Zhang, Y. Black phosphorus field-effect transistors. *Nat. Nanotechnol.* **9**, 372-377 (2014).
216. Liu, H., Neal, A. T., Zhu, Z., Luo, Z., Xu, X., Tománek, D. & Ye, P. D. Phosphorene: An unexplored 2D semiconductor with a high hole mobility. *ACS Nano* **8**, 4033-4041 (2014).
217. Das, S., Demarteau, M. & Roelofs, A. Ambipolar phosphorene field effect transistor. *ACS Nano* **8**, 11730-11738 (2014).
218. Liu, H., Neal, A. T., Si, M., Du, Y. & Ye, P. D. The effect of dielectric capping on few-layer phosphorene transistors: Tuning the Schottky barrier heights. *IEEE Electron Device Lett.* **35**, 795-797 (2014).
219. Xia, F., Wang, H. & Jia, Y. Rediscovering black phosphorus as an anisotropic layered material for optoelectronics and electronics. *Nat. Commun.* **5**, 4458 (2014).
220. Das, S., Zhang, W., Demarteau, M., Hoffmann, A., Dubey, M. & Roelofs, A. Tunable transport gap in phosphorene. *Nano Lett.* **14**, 5733-5739 (2014).

221. Hong, T., Chamlagain, B., Lin, W., Chuang, H.-J., Pan, M., Zhou, Z. & Xu, Y.-Q. Polarized photocurrent response in black phosphorus field-effect transistors. *Nanoscale* **6**, 8978-8983 (2014).
222. Engel, M., Steiner, M. & Avouris, P. Black phosphorus photodetector for multispectral, high-resolution imaging. *Nano Lett.* **14**, 6414-6417 (2014).
223. Youngblood, N., Chen, C., Koester, S. J. & Li, M. Waveguide-integrated black phosphorus photodetector with high responsivity and low dark current. *Nat. Photonics* **9**, 247-252 (2015).
224. Ashley, M. F. Nuclear spin of phosphorus from band spectrum analysis. *Phys. Rev.* **44**, 919-927 (1933).
225. Jenkins, F. A. & Ashley, M. F. Nuclear spin of phosphorus from the band spectrum. *Nature* **129**, 829-830 (1932).
226. Rodin, A. S., Carvalho, A. & Castro Neto, A. H. Strain-induced gap modification in black phosphorus. *Phys. Rev. Lett.* **112**, 176801 (2014).
227. Wood, J. D., Wells, S. A., Jariwala, D., Chen, K.-S., Cho, E., Sangwan, V. K., Liu, X., Lauhon, L. J., Marks, T. J. & Hersam, M. C. Effective passivation of exfoliated black phosphorus transistors against ambient degradation. *Nano Lett.* **14**, 6964-6970 (2014).
228. Monsma, D. J., Vlutters, R. & Lodder, J. C. Room temperature-operating spin-valve transistors formed by vacuum bonding. *Science* **281**, 407-409 (1998).
229. Anugrah, Y., Robbins, M. C., Crowell, P. A. & Koester, S. J. Determination of the Schottky barrier height of ferromagnetic contacts to few-layer phosphorene. *Appl. Phys. Lett.* **106**, 103108 (2015).

Appendix

Graphene mesas

1) Clean sample using acetone, methanol, isopropanol, and blow dry using nitrogen gun,
2) Pre-bake sample on a hotplate at 115 °C for 1 minute,
3) Spin Shipley S1813 photoresist on sample at 4000 rpm for 30 seconds,
4) Soft-bake sample on a hotplate at 105 °C for 1 minute,
5) Expose sample using the hard contact mode on the contact aligner (MA6 or MABA6, intensity ~12 mW/cm^2) and pre-made optical mask with the mesa patterns for 5 seconds,
6) Develop patterns in Microposit MF-319 developer:deionized (DI) water (1:5) solution for 35 seconds,
7) Rinse sample in DI water for 3 minutes and blow dry using nitrogen gun,
8) Check for patterns under a microscope, if patterns turn out well, proceed with step 9, otherwise redo the process from step 1,
9) Etch the unprotected graphene using oxygen plasma in the STS etcher (reactive ion etch) at 100 W for 20 seconds,
10) Dissolve resist by rinsing with acetone, methanol, IPA, and blow dry using nitrogen gun.

Nonmagnetic (NM) contacts

1) Clean sample using acetone, methanol, isopropanol, and blow dry using nitrogen gun,
2) Pre-bake sample on a hotplate at 115 °C for 1 minute,
3) Spin Shipley S1813 photoresist on sample at 6500 rpm for 45 seconds,
4) Soft-bake sample on a hotplate at 105 °C for 1 minute,
5) Expose sample using the hard contact mode on the contact aligner (MA6 or MABA6, intensity ~12 mW/cm^2) and pre-made optical mask with the NM contact patterns for 7 seconds,
6) Load sample in the image reversal oven (model YES 310) filled with anhydrous ammonia gas at 90 °C for 90 minutes,
7) Subject the sample to flood-exposure using the Oriel system (model 8095) for 6 minutes, rotate sample by 90 degrees and expose for another 6 minutes,
8) Develop patterns in Microposit MF-319 developer:DI water (1:5) solution for 3 minutes,
9) Rinse sample in DI water for 3 minutes and blow dry using nitrogen gun,
10) Load sample into the electron beam evaporation system (CHA evaporator) and let it pump down to base pressure of 8×10^{-7} Torr or lower,
11) Deposit 5 nm of Cr and 80 nm Au,
12) Unload sample and soak in acetone for at least 1 hour for metal lift-off,
13) Rinse in acetone, methanol, IPA, and blow dry using nitrogen gun.

Ferromagnetic (FM) contacts

1) Clean sample using acetone, methanol, isopropanol, and blow dry using nitrogen gun,
2) Pre-bake sample on a hotplate at 115 °C for 1 minute,
3) Spin MMA EL9 resist on sample at 3000 rpm for 60 seconds,
4) Post-bake sample on a hotplate at 150 °C for 2 minutes,
5) Spin PMMA C2 resist on sample at 3000 rpm for 60 seconds,
6) Post-bake sample on a hotplate at 180 °C for 8 minutes,
7) Expose the resist using electron beam (e-beam) lithography tool to write the FM contact patterns with a dose of 1100 $\mu C/cm^2$ for thin electrode regions directly in contact with graphene and 550 $\mu C/cm^2$ for the bulk regions,
8) Develop patterns in IPA:DI water (1:3) solution for 120 seconds,
9) Rinse sample using running DI water for 1 minute and blow dry using nitrogen gun,
10) Load sample into the electron beam evaporation system (CHA evaporator) and let it pump down to base pressure of 8 x 10^{-7} Torr or lower,
11) Deposit 40 nm of Co and 20 nm Al,
12) Unload sample and soak in acetone for at least 1 hour for metal lift-off,
13) Rinse in acetone, methanol, IPA, and blow dry using nitrogen gun.

Double buried-gate (DBG) structures

1) Clean sample using acetone, methanol, isopropanol, and blow dry using nitrogen gun,
2) Pre-bake sample on a hotplate at 150 °C for 10 minutes,
3) Spin PMMA C2 resist on sample at 3000 rpm for 60 seconds,
4) Post-bake sample on a hotplate at 180 °C for 8 minutes,
5) Expose the resist using electron beam (e-beam) lithography tool to write the double buried-gate patterns with a dose of 1100 $\mu C/cm^2$ using the built-in proximity effect correction (PEC) function,
6) Develop patterns in MIBK:IPA (1:3) solution for 90 seconds,
7) Rinse sample in IPA bath for 2 minutes and blow dry using nitrogen gun,
8) Load sample into the electron beam evaporation system (CHA evaporator) and let it pump down to base pressure of 8 x 10^{-7} Torr or lower,
9) Deposit 5 nm of Cr and 25 nm Au,
10) Unload sample and soak in acetone for at least 1 hour for metal lift-off,
11) Rinse in acetone, methanol, IPA, and blow dry using nitrogen gun,
12) Initiate ALD, ramp up the temperature to 300 °C, and purge the chamber with Al_2O_3 deposition for 50 cycles,
13) Deposit 1600 cycles of Al_2O_3 (~1700 Å),
14) Check the resulting thickness using an ellipsometer,
15) Clean sample using acetone, methanol, isopropanol, and blow dry using nitrogen gun,
16) Pre-bake sample on a hotplate at 115 °C for 1 minute,
17) Spin Shipley S1813 photoresist on sample at 4000 rpm for 30 seconds,

18) Soft-bake sample on a hotplate at 105 °C for 1 minute,
19) Expose sample using the hard contact mode on the contact aligner (MA6 or MABA6, intensity ~12 mW/cm^2) and pre-made optical mask with the via contact patterns for 7 seconds,
20) Load sample in the image reversal oven (model YES 310) filled with anhydrous ammonia gas at 90 °C for 90 minutes,
21) Subject the sample to flood-exposure using the Oriel system (model 8095) for 6 minutes, rotate sample by 90 degrees and expose for another 6 minutes,
22) Develop patterns in Microposit MF-319 developer:DI water (1:5) solution for 3 minutes,
23) Rinse sample in DI water for 3 minutes and blow dry using nitrogen gun,
24) Hard-bake the resist on a hot plate at 120 °C for 3 minutes,
25) Etch the Al_2O_3 in BOE:DI water (1:10) solution for 10 minutes to make sure all of the Al2O3 in the unprotected region is removed (etch rate ~1 nm/s, but seems to slow down after a while and thus the much longer etch time),
26) Rinse sample in DI water for 3 minutes and blow dry,
27) Confirm that the oxide on the pads has been removed using the probe station by quickly measuring the resistance of two probes placed on one pad,
28) Load sample into the electron beam evaporation system (CHA evaporator) and let it pump down to base pressure of 8×10^{-7} Torr or lower,
29) Deposit 5 nm of Cr and 80 nm Au for the via layer metal,
30) Unload sample and soak in acetone for at least 2 hours for metal lift-off,
31) Rinse in acetone, methanol, IPA, and blow dry using nitrogen gun.